FRACTAL ANALYSES AND GEOMETRICAL MODELS OF FRACTURE SURFACES IN ROCK

A Dissertation
Presented to the Faculty of Graduate Studies
of
The University of Ottawa
in Candidacy for the degree of
Doctor of Philosophy

by
Daniel Edward Roach

ISBN 0-315-85844-3

UNIVERSITÉ D'OTTAWA
UNIVERSITY OF OTTAWA

ABSTRACT

Fracture propagation in rock often produces complex patterns, such as the branching patterns of fracture networks, or the irregular radiating patterns on fracture surfaces. These patterns often appear complex because they are unpredictable in detail, yet predictable in the sense that smaller pieces of the pattern, when suitably enlarged, are statistically similar to larger pieces of the pattern. This property of statistical self-similarity can be quantified using fractal geometry. The fractal nature of rock fracture patterns is related to lithological properties and to the dynamics of the fracturing processes.

Joint surfaces in homogeneous rocks display rough radiating ridges. A "plumose joint" surface was analyzed using the slit island method and found to have a fractal dimension (D_f) of 2.24 ± .14 (95%). Surfaces with similar fractal dimensions (2.2 - 2.5) are produced by a three-dimensional computer simulation of jointing. In the simulation, randomly-distributed defects cause local mis-orientations of the stress field and local deflection of the propagating fracture front. After passing through the defect the joint surface is re-oriented relative to remote stresses, and a planar radial fracture segment (i.e. inclusion hackle) is formed. Collectively, the numerous inclusion hackle form the plumose surface pattern. For the simulation results, D_f increases (i.e. the surface gets rougher) in proportion to the log of the defect density. The simulation also demonstrates a complex relationship between D_f of the propagating fracture front and D_f of the fracture surface.

Shatter cones are conical fracture surfaces produced during high energy events such as meteorite impact and nuclear explosion. These

fractures also display radiating surface features. Using a modified version of the slit island method, the fractal dimension of a shatter cone surface in limestone is estimated to be $2.24 \pm .09$. The observation of shingled convex fracture surfaces within the conical envelope surrounding the shatter cone surface is demonstrated to support the genetic model of Johnson and Talbot (1964). Striations on these fracture surfaces are re-interpreted as micro-fracture intersections.

The measured fractal dimensions of the joint and shatter cone surfaces (i.e 2.24) are within the range reported for most fracture surfaces in metals (i.e. 2.1 ~ 2.3).

ACKNOWLEDGEMENTS

I thank Bill Fyson for his continued encouragement and support throughout this project. I appreciate his willingness to let me wander, sometimes with Brownian motion, in pursuit of new topics.

I thank Tony Fowler for enthusiastically introducing to me the many fascinating elements of fractal geometry and non-linear dynamics. I also thank Tony Fowler for the use of his IIfx, and for countless inspiring conversations about all sorts of dynamical problems. I am indebted to the Fowler family, and to Geoff and Anne Burbidge for my "homes away from home".

I thank my wife Robin for her understanding and continued support.

TABLE OF CONTENTS

LIST OF FIGURES

CHAPTER 1
INTRODUCTION

1.1 General introduction

Two million years ago *Australopithecus* used knowledge of fracture mechanics to manufacture sharp-edged stone tools; the first known physical invention attributed to primitive humans (Bronowski, 1973). These early material scientists and engineers also recognized that homogeneous fine-grained rocks such as flint and chert were ideal for producing sharp and durable tools. This knowledge and its practical application was so powerful that for the next million years of evolution these tools endured as human's only physical invention to be preserved from that time. Perhaps this practical knowledge of rock mechanics gave early man the competitive "edge" over more physically dangerous species, allowing for the eventual evolution of Homo sapiens.

Undoubtedly, during that million years of manufacturing one of our ancestors must have noticed the delicate patterns which graced the many fracture surfaces, perhaps recognizing that these patterns always radiated away from the point where one rock was struck by another. Early man may have believed that these patterns were actually contained inside the rock since they appeared each time a new fracture revealed more of the rock's interior. Much of this dissertation is concerned with a similar notion, that is, that surface features observed on fracture surfaces of rock are strongly influenced by the material properties of the rock.

The relatively recent inventions of mathematics and science have accelerated human's ability to understand the physical universe. During the past 100 years great strides have been made in the fields of fracturing and rock mechanics. Theory and experiment have been continuously refined such that mathematical models of fracturing are increasingly realistic. However, most of the models are concerned with ideal hypothetical materials, which are hardly similar to the complex arrangement of minerals that constitute rock. Atkinson (1987), in his introductory chapter for the book **Fracture Mechanics of Rock**, points out that "our understanding of brittle and semi-brittle rock fracture has seriously lagged behind developments in understanding plasticity and solid state flow of geological materials". This is due in part to the complex nature of fracture in crystalline materials such as rocks. Atkinson emphasizes the need to learn more about the interaction between rock microstructures and the fracturing process. This dissertation addresses that need.

Fracture in polyphase material yields visually and quantitatively complex fracture surfaces. So complex in fact, that surface features were originally described mainly by analogy with well-known biological patterns. Radiating surface patterns on rock fractures were described by Woodworth, 1896, as "feather-like". Other descriptive terms have included "hackle markings", "horse-tailed striations", and "plumose markings". These terms prove sufficient for recognition purposes, however, they are inadequate for the quantitative interpretation of fracture surface features. A more rigorous approach to the interpretation of fracture surface features was first made by material scientists studying ceramics, glass and metal. Their study, known as "fractography", relates detailed fracture surface features to processes active during fracture propagation. Fractography has only recently been applied to fracture surface patterns in rock (Hodgson, 1961; Kulander *et al*, 1979; Kulander and Dean, 1985; Barton, 1983; DeGraff and Aydin, 1987) .

Coincident with the use of fractography in rock mechanics during the past decades, a revolutionary idea for describing complex natural objects was introduced by Mandelbrot in his book, **Les Objet Fractals:Forme, Hasard, et Dimension** (1975). The book documents methods for creating and measuring complex, scale-invariant, non-Euclidean objects, known as fractals. In the succeeding years this new geometry has proved useful in quantifying many natural objects which were previously intractable. The importance of this technique in analyzing fracture surfaces is emphasized by Mandelbrot who states that the term "fractal" was chosen "in explicit cognizance of the fact that the irregularities found in fractal sets are often strikingly reminiscent of fracture surfaces in metals" (Mandelbrot *et al*, 1984). This dissertation uses fractal geometry in a quantitative fractographic study of joint surfaces in one rock type. Note that the words "fracture, fractography, and fractal" stem from the latin root fractus - the past participle of frangere, meaning to break into pieces.

One important aspect of fractal geometry to note is the iterative nature of the algorithms used to produce and analyze fractal sets. Not surprisingly, there is a natural link between computers and fractals. At the core of this dissertation is a 3-dimensional computer simulation of low-velocity joint propagation. The flexibility of the simulation permits experimentation with realistic dynamic growth parameters and material properties. Variations in joint surface morphology as a function of these parameter changes are documented using fractal geometry.

A natural extension to joint analysis is the study of extremely-high energy, hyper-velocity fractures in rock, i.e. shatter cones. These are also analyzed using fractal geometry. Their origin is discussed in light of new observations and interpretations of the fracture surface.

The use of fractal geometry in fracture mechanics is by no means restricted to fracture surfaces. On the contrary, much of the current work is concerned with the fractal characteristics of fracture networks. Some of these networks result from high-energy fracture bifurcation. This process is an unresolved problem in fracture mechanics, and "as yet, no universal crack branching criterion has emerged" (Kanninen and Popelar, 1985). This thesis compares high-energy fracture bifurcation to other known fractal growth processes, such as diffusion-limited aggregation, viscous fingering, and dielectric breakdown. These ideas are also incorporated into a hypothetical model of pore-pressure controlled jointing.

At the time of this writing, fractal geometry is a relatively new tool in geology. For this reason, there is an introductory chapter (Chapter 3) explaining the concepts of fractal geometry. In addition, Chapter 2 introduces the fundamentals of fracture mechanics to readers who have principle interests outside the fields of structural geology and fracture mechanics.

1.2 Innovations

The key elements of this thesis are original contributions to the study of structural geology. At the time of this writing, fractal geometry is proving increasingly useful as a tool for quantifying many of the scale-invariant features long recognized in structural geology. Recent work, relevant to topics in this thesis may thus be unknown to me. Accepting this possibility, the following lists what I understand to be original contributions that this thesis makes to the field of structural geology.

a) The measurement of the fractal dimension of a portion of a plumose joint surface in an carbonate-cemented arkose using a modified version of the the slit island technique.

b) The development of a 3-dimensional computer simulation of joint propagation in a homogeneous medium containing randomly-distributed point defects, resulting in simulated joint surfaces that are quantitatively similar (i.e. having the same fractal dimension) to natural plumose joints.

c) The demonstration of a linear relationship between the fractal dimension of the simulated joint surface and the logarithm of the defect density.

d) The demonstration of a complex relationship between the fractal dimension of the simulated joint surfaces and the fractal dimension of the propagating fracture front as measured during fracture propagation.

e) The measurement of the fractal dimension of a portion of a shatter cone surface in fine-grained limestone using a modified version of the slit island technique, including the practical application of a mathematical theorem which essentially states that the fractal nature of a set is preserved under non-infinite heterogeneous transformation.

f) The first documented observation and interpretation of shingled, striated, convex fracture surfaces within the rock volume surrounding the shatter cone surface.

g) The measurement of the fractal dimension of a mode I fracture bifurcation pattern using the box method.

h) A conceptual explanation of dynamic fracture bifurcation that combines recent advances in dynamic fracture theory with new models for random growth processes.

i) An attempt to conceptually apply Laplace field/random growth dynamics to pore pressure-controlled, subcritical joint propagation.

CHAPTER 2
FRACTURE MECHANICS OF JOINTS

This chapter introduces fracture mechanics and fractography as applied to rock joints. Much of this discussion is derived from the review of the jointing literature by Pollard and Aydin (1988) and the handbook of fractographic techniques by Kulander *et al* (1979).

2.1 Historical perspective

Since the work of Hopkins (1835,1841) there has been much discussion on the origin of jointed structures in rock (for example see Gilbert, 1882a,1882b, 1884; LeConte,1882; King, 1875; Crosby, 1882; McGee,1883; Becker,1891,1893,1895; Van Hise,1896; Hoskins,1896; Hartmann, 1896; Mohr,1900; Bucher, 1920,1921; Balk, 1937; Parker, 1942; Muehlberger, 1961). Somewhat overshadowed were the detailed observations made by Woodworth (1896) in his interpretive study of joint surface morphology. Woodworth was the first to propose that plumose structures were caused by fracture initiation at a point and the subsequent outward propagation of an opening fracture. The modern era of rock mechanics includes Lachenbruch's (1961,1962) interpretation of field observations. In these papers he combined 1) the equations for stress distribution around cracks (after Inglis, 1913), 2) the physics of crack propagation as developed by Griffith (1921), and 3) the principles of modern fracture mechanics as established by Irwin, (1957, 1958). Hodgson (1961) and Bankwitz (1965,1966) reinforced Woodworth's idea that much information about fracture propagation is contained in the surface morphology of a fracture. Techniques for understanding fracture propagation based on the relationship between fracture mechanic principles and fracture surface features have been further refined by Lutton (1969; for unconsolidated mud), Kulander *et al*,(1979), Barton, (1983), Kulander and Dean (1985), and DeGraff and Aydin (1987).

2.2 Definitions

In the geological literature, there is much ambiguity associated with the subject of jointed structures. Much of this is due to the evolving nomenclature used to describe joint related features. This dissertation adopts the definitions of Pollard and Segall (1987), and Pollard and Aydin (1988). The definitions are based on the principles of fracture mechanics (Lawn and Wilshaw, 1975; Kanninen and Popelar, 1985) and are sufficiently flexible to encompass the complex character of geological materials.

2.2.1 Fractures, joints and faults

According to Pollard and Aydin, (1988), fractures in rock have three basic characteristics;

1) fractures have two parallel surfaces that meet at the fracture front,

2) the two surfaces are approximately planar, and

3) the relative displacement of originally adjacent points across the fracture is small compared to the fracture length.

The three pure modes of fracture are illustrated in Fig. 2.1. Mode I

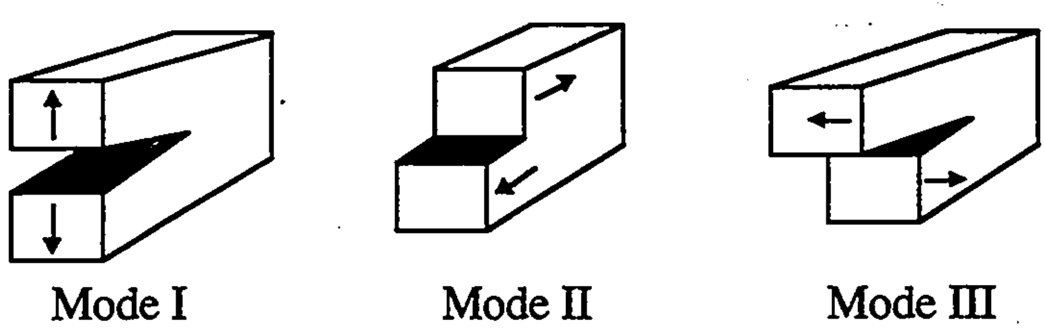

Fig. 2.1 The three modes of fracture. Arrows indicate displacement directions. Fracture surface is shaded. (After Irwin,1958; and Lawn and Wilshaw, 1975). See text for complete explanation.

fractures have opening displacements perpendicular to the fracture surface. Shearing displacements are parallel to the fracture surface, either perpendicular (mode II) or parallel (mode III) to the propagation front

(Fig. 2.1). Joints are mode I opening displacements, whereas faults are associated with shearing modes. However, as stressed by Pollard and Aydin (1988), "one should not be too stringent about these associations since modes of fracture may vary along the fracture front and may involve mixtures of modes I, II and III".

Much of the joint literature (Bucher, 1921; Parker, 1942, 1969; Nickelsen and Hough, 1967,1969; Scheidegger, 1982; Engelder, 1982; Barton, 1983; Segall and Pollard, 1983; Hancock, 1985) focuses on the problematic existence of shear joints - those joints in conjugate pairs and/or joints displaying evidence of shear modes. In their comprehensive review Pollard and Aydin (1988) contend that "the concept of shear joints is sheer nonsense" because joints with shear displacements are defined as faults and they have stress, strain and displacement fields which are distinctly different from those associated with joints. Therefore, in this dissertation the following distinction is made; joints are associated with opening displacements whereas faults are associated with shear displacements.

Joints are further described (using Euclidean geometry) by Pollard and Aydin (1988) as "three-dimensional structures composed of two matching surfaces (joint faces) that are commonly idealized as smooth, continuous and planar". They add that "virtually all joints have some roughness, minor and major discontinuities, and occasional curves and kinks."

2.3 Mechanics of jointing

Prior to discussing the geometrical aspects of joint surface morphology it is important to understand the currently accepted ideas of joint formation. This is accomplished by briefly reviewing the principles of fracture mechanics as applied to rock jointing.

2.3.1 Joint initiation

Joint origins are commonly the site of geometric and/or material inhomogeneities such as fossils, clasts, cavities, grain boundaries or pre-existing fractures (Hodgson, 1961; Wise, 1964; Kulander *et al*, 1979; Barton, 1983; Bahat and Engelder, 1984). Pollard and Aydin (1988) recognize two important circumstances where the magnitude of local tensile stress at a flaw exceeds the tensile strength of the rock and thus initiates jointing;

1) concentration of an otherwise insufficient for fracture remote tension, and

2) conversion of remote compression into local tension.

Remote tensile stress can be concentrated when inhomogeneities have elastic properties that differ from the surrounding rock (for examples see Jaeger and Cook, 1969). Eccentric geometrical flaws such as cavities, grain boundaries and microcracks can also concentrate stresses.

While it is relatively easy to visualize joint initiation and propagation under remote tension, it is more difficult to envisage joint formation and propagation under compressive stress field conditions typical of the shallow crust (McGarr and Gay, 1978 and McGarr, 1982). Theory (Jaeger and Cook, 1969), experiment (Borg and Maxwell, 1956; Gallagher *et al*, 1974) and observation of natural fractures (Aydin, 1978) demonstrate that remote compression can be converted into local tension at grain contacts, inclusions, pores and microcracks. However, experimental studies (Brace and Bombolakis, 1963; Hoek and Bieniawski, 1965; Ingrafea, 1981 and Nemat-Nasser and Horii, 1982) reveal that fractures initiated under compressive fields do not grow larger than the initiating material flaw. How then do joints continue to propagate in a totally compressive stress field? One way this problem may be overcome is by subjecting microcracks and cavities to an internal fluid pressure that exceeds the least compressive stress, σ_3^r, thereby converting the least compressive stress into local tension (Rubey and Hubbert, 1959; Suppe, 1985). In this way, a joint formed under compressive stresses can propagate provided that sufficient internal fluid pressure is maintained.

2.3.2 Joint propagation

Joint propagation is controlled by the concentrated stresses near the edge of the fracture (Fig. 2.2). This region of stress concentration is relatively small since stress magnitudes are inversely proportional to the square of the distance away from the fracture edge (Lawn and Wilshaw, 1975; Kanninen and Popelar, 1985). Linear elastic fracture theory dictates that all stress components in the small region of stress concentration (within diameter **E** of Fig. 2.2) are proportional to stress intensity factors, K_I, K_{II} and K_{III}, that in turn correspond to the three modes of fracture, and to three unique stress distributions near the fracture tip. Fracture propagation proceeds in a given mode provided that the stress intensity factor for that mode exceeds a critical value, K_C. Theoretical equations for fracture propagation in isotropic materials have been derived for the various fracture modes and their corresponding stress distributions (Gell and Smith, 1967; Lawn and Wilshaw, 1975). The equations are applicable only if inelastic deformation (e.g. microcracking) is restricted to a small "process zone", located at the edge of the fracture (within diameter **P** in Fig. 2.2), (Irwin, 1957). The equations show that pure mode I loading in an isotropic material results in fracture propagation perpendicular to the least remote compressive stress, $\sigma_3{}^r$. Theoretically, mixed-mode loading, (i.e. I+II , or I+III), produces out of plane fracture propagation resulting in smoothly curved or sharply kinked fracture paths. The complex joint surfaces in rock indicate that joints are not pure mode I fractures. Mixed mode propagation occurs when the stresses along the fracture front are locally altered in the vicinity of structural anisotropies such as pore spaces, inclusions, grain boundaries, and microcracks (Kulander *et al*, 1979; Barton, 1983). The resulting twisted and tilted fracture segments contribute to the complexity of the overall joint surface.

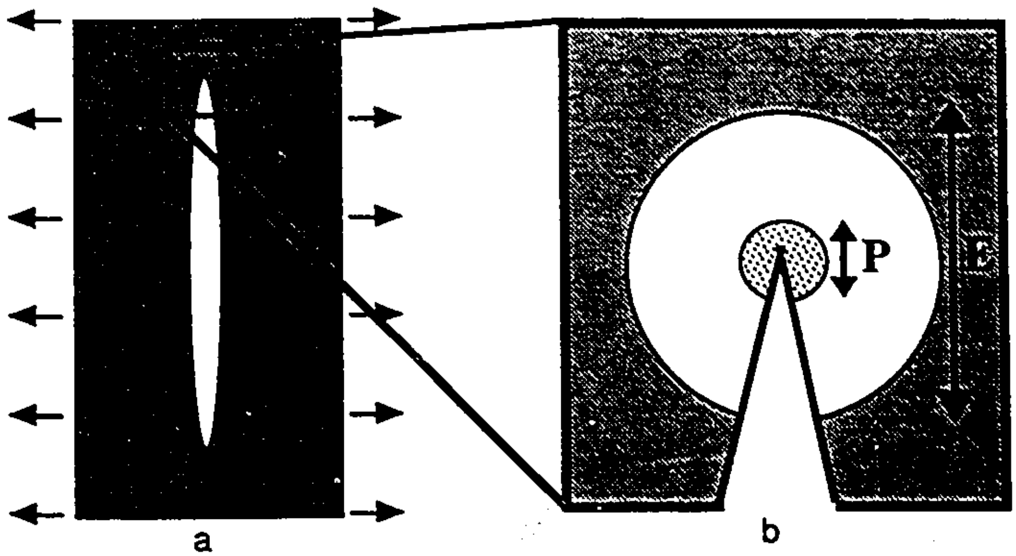

Fig. 2.2 a) Idealized sketch of mode I fracture under remote tension, (arrows indicate direction of remote tension). b) Fracture tip region where local stress field is approximated by elastic solution within diameter E. Inelastic deformation occurs within the process zone, diameter P. (After Pollard and Aydin, 1988).

The principles described above are applicable to slow-forming fractures, i.e. fractures that propagate at velocities much less then the velocity of stress waves in the rock. There is evidence that many joints are slow-forming. Atkinson and Meredith (1987) found that chemical reactions at fracture tips cause many rock fractures to propagate slowly, under subcritical conditions (where K_I is much less then K_{IC}). Similarly, those joints hypothesized to form in response to pore-pressure variations are also thought to be slow-forming (Segall, 1984).

For fractures propagating at near-sonic velocities (in metals), the shape of the near-tip stress field differs significantly from its quasi static counterpart (see for example Freund, 1990). This has important implications for dynamic fracture path stability and fracture bifurcation, as discussed in Appendix A.

2.4 Fractography

Joint propagation is a difficult phenomena to observe directly because it often occurs unpredictably, rapidly, and completely within opaque rock. Nevertheless, fracture propagation has been observed in experiments using translucent materials (for example Kies *et al*, 1950), sonic interference imaging techniques (for example, Michalske *et al*, 1981) and more recently, micro-seismology (Lockner *et al*, 1991). Much of our knowledge regarding fracture propagation in rock has been obtained through fractography - the detailed interpretive study of joint surface morphology. Fractography has been used by ceramists and metallurgists for decades, yet its application to rock joint surfaces is relatively recent (Kulander *et al*, 1979). Fracture surface features are broadly classified according to their size. Long-range changes in the stress field produce tendential fracture features whereas short-range local stress perturbations result in transient features.

2.4.1 Transient joint surface features

Transient fracture features are local perturbations of the fracture surface attributable to undulations of the advancing fracture front (Kulander *et al*, 1979; Barton, 1983). These undulations form in response to fracture propagation velocity changes and/or local disruptions of the applied stress field. Kulander *et al*, (1979) propose that the applied stress field can be locally altered by;

1) transverse and longitudinal elastic waves,

2) chemical and physical inhomogeneities in the rock, and

3) external alteration of the applied stress field.

Transient features are generally best developed on joints in fine-grained homogeneous rocks such as shale, basalt and limestone. Transient features of an idealized joint surface are illustrated in Figure 2.3 .

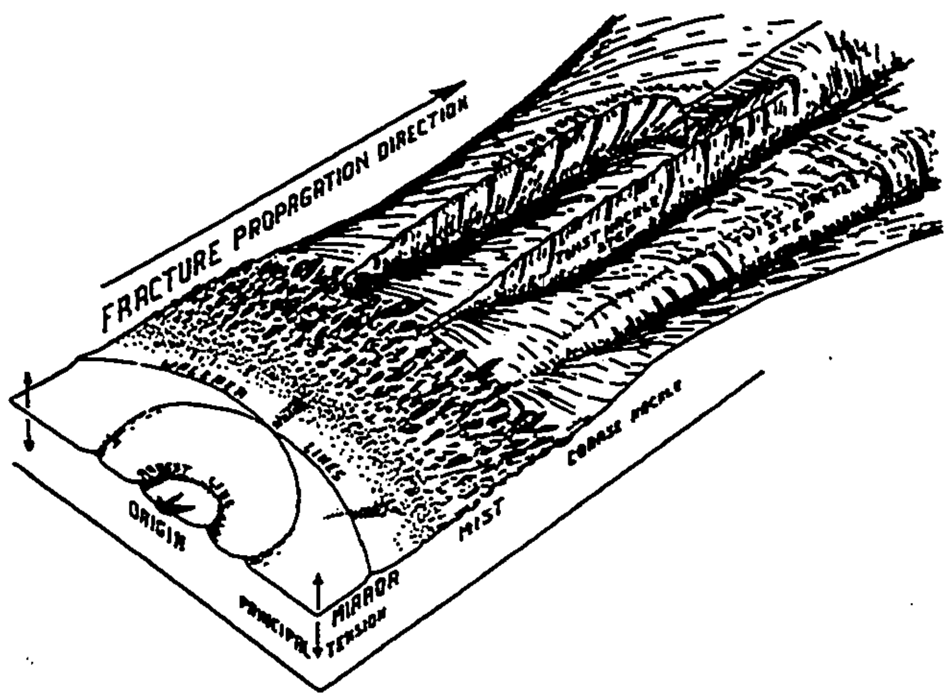

Fig. 2.3 Transient joint surface morphology illustrating origin, Wallner lines, mirror-mist-hackle zones and twist hackle morphology (after Kulander *et al*, 1979). See text for details.

2.4.1.1 Fracture origin

The fracture origin is the initial point of fracture. It is usually the site of a stress-concentrating flaw, such as a fossil, concretion, large clast, cementation or lithology variation, pore space, bedding irregularity, surface irregularity, pre-existing fracture tip, etc. (Kulander *et al*, 1979).

2.4.1.2 Mirror region

In glass, the smooth featureless fracture surface surrounding the origin (see Fig. 2.3) has been termed the mirror region, (Johnson and Holloway, 1966). This region is essentially featureless because the stress intensity factors have not yet exceeded the critical values necessary to break a large number of bonds oblique to the advancing fracture front. In rocks, the mirror zone is represented by the fracture surface region containing no undulations larger than the rock grain size (Kulander *et al*, 1979).

2.4.1.3 Wallner Lines

Wallner lines form when an elastic wave, created at a flaw in one location along the fracture front, intersects the rest of the propagating fracture front causing a temporary deflection in the fracture (Wallner, 1939). These subtle cusp-like lines are convex in the direction of fracture propagation (see Fig. 2.3). Wallner lines are generally not apparent in rocks due to the coarse grain size of rocks, and the masking by other coarse transient features (Kulander *et al*, 1979).

2.4.1.4 Mist region

The mist zone (see Fig. 2.3) is characterized (in glasses) by a rough, dull surface, unlike the smooth reflective surface of the mirror zone. The mirror-mist boundary marks the position where critical values of crack tip stresses and propagation velocities are initially exceeded (Shand, 1954). Once these critical values are attained, sections of the fracture tip along the fracture front deviate above and below the mean propagation plane creating minute undulations referred to as "velocity hackle". Poncelet (1958) states that increased fracture propagation velocity within the mist zone results in larger velocity hackle and an increased angle between the hackle surface and the main fracture plane. Frechette (1972) concludes that the mist region is not fully understood and its origin may be due to interaction between elastic waves and the applied stress field.

2.4.1.5 Twist Hackle

Twist hackle forms when a propagating fracture front enters a region of different stress orientation, causing it to break into en echelon fracture faces, each perpendicular to the new tension direction (Kulander *et al*, 1979; Barton, 1983). The fractures separating the en echelon faces form steps, called twist hackle steps (see Fig. 2.3). Oblique stresses across twist hackle steps result in secondary twist hackle oriented perpendicular to the twist hackle long axis (see Fig. 2.3). Twist hackle can occur within any region of the fracture.

2.4.1.6 Inclusion hackle

Inclusion hackle forms when the propagating fracture front encounters structural anisotropies such as an inclusions, pore spaces, grains of different size and/or composition, etc. As the fracture front approaches a defect, the local stress field at the edge of the fracture is mis-aligned relative to the remote stress system, inducing out of plane fracture propagation within the region of the inclusion. As the fracture front emerges from the far side of the inclusion the local stress field re-aligns with the remote stresses and fracture propagation continues in an orientation perpendicular to the remote least compression, σ_3^r, (Frechette,1972; Preston, 1926), (see Fig. 2.4). The net result is a displaced fracture segment, oriented parallel to the mean joint path, extending away from the far side of the defect in the direction of the propagating fracture.

Kulander *et al* (1979) and Barton (1983) suggest that inclusion hackle is probably the most common constituent of hackle plumes in crystalline rocks. A major objective of this thesis is to quantify and model fracture surfaces formed by inclusion hackle using a relatively new tool - fractal geometry.

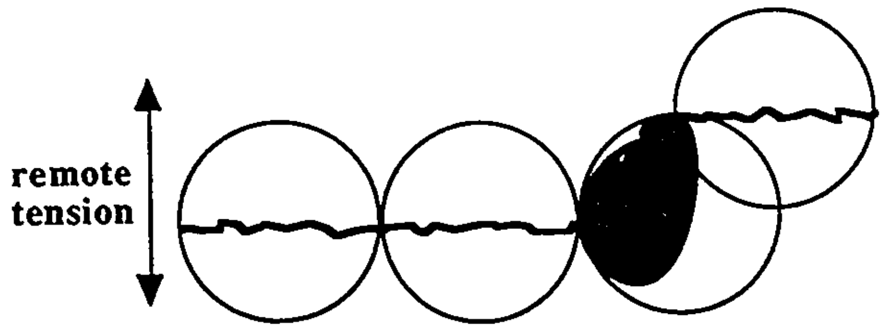

Fig. 2.4 Cross-section of inclusion hackle. Fracture is propagating left to right, perpendicular to remote tension. Each sphere represents the position of the process zone at some time. When the fracture encounters a defect of process zone size it is deflected to a new level. After leaving the vicinity of the defect, the fracture continues to propagate perpendicular to remote tension.

CHAPTER 3
FRACTAL GEOMETRY

"Mandelbrot's fractal geometry provides both a description and a mathematical model for many of the seemingly complex forms found in nature" - Richard F. Voss (1988).

Mandelbrot, (1982) notes that natural objects such as clouds, mountains, trees and coastlines are not easily described by traditional Euclidean geometry. More importantly, each of these objects is statistically self-similar, that is, it appears the same at different levels of magnification. This property of scale invariance is the essence of fractal geometry. For most geologists, this concept is not entirely new. On the contrary, fractal geometry is simply the mathematical formalization of a well-established geological axiom: that small-scale features are similar to large-scale features.

3.1 Comparing Euclidean and fractal geometries

Voss (1988) documents several important differences between fractal geometry and traditional Euclidian geometry.

1) Euclidean objects have a characteristic size; for example, a line has length and a circle has radius. Fractal objects are statistically self-similar, so they possess no characteristic size, (e.g. how big is a typical tree branch?).

2) Euclidean geometry facilitates accurate description of man-made objects but is ineffective at describing seemingly complex natural objects. Fractal geometry can describe complex natural objects and provide a quantitative measure useful for comparison.

3) Euclidean objects are often described by an algebraic formula and generated through scale-bound geometric construction (e.g. $x^2+y^2=r^2$). Fractal objects are often the result of many iterative geometric constructions operating over a range of scales. Therefore, computers are an ideal tool for generating and measuring fractals.

Both Euclidean and fractal geometries are only approximations to natural geometries. Furthermore, both are only accurate over a range of scales. For example, when viewed at close range with the naked eye, a soap bubble might be accurately described as a sphere, (a three-dimensional object). However, when viewed from the other side of a football field, the bubble appears as a point (a zero dimensional object). Furthermore, at the scale of atoms, the soap bubble might be more accurately described as a rough surface composed of chemical bonds of finite length. In a similar manner, natural fractal objects, (such as clouds, trees, etc.) are only fractal over a finite range of scales.

3.2 Dimension

The Euclidean notion of dimension (e.g. dimension 0 = a point, dimension 1 = a line, etc.) has long been the basis for informal and formal instruction of mathematics, science and engineering. These notions are so

Object	Euclidean dimension	Fractal dimension D_f
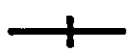 line	1	can be divided into 2 parts each scaled by ratio r = 1/2, D_f = log(2) / log (1/2) = 1
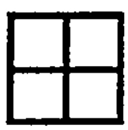 square	2	can be divided into 4 parts each scaled by ratio r = 1/2, D_f = log(4) / log (1/2) = 2
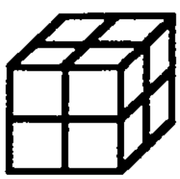 cube	3	can be divided into 8 parts each scaled by ratio r = 1/2, D_f = log(8) / log(1/2) = 3

In general, for an object of N identical parts, each scaled down from the whole by a factor of r;

$$N\, r^{D_f} = 1$$

and

$$D_f = \frac{\log N}{\log 1/r}$$

Fig. 3.1 Scaling properties of standard objects of known Euclidean dimension. See text for complete explanation. (After Voss, 1988).

deeply entrenched that it is often difficult to initially conceive of non-integer, or fractal dimensions. The concept of fractal dimension is well illustrated by considering the scaling properties of standard objects of known Euclidean dimension. The line in Fig. 3.1 has a Euclidean dimension of one. It can be divided into N identical parts, each equal to the original object multiplied by a scaling factor r, where $r= l/N$. Similarly, a two-dimensional object such as a square can be divided into N parts, each one scaled down from the original by a scaling factor $r=l/N^{1/2}$. Extending into three dimensions, a cube can be subdivided into N smaller cubes, each one being scale down by $r=l/N^{1/3}$. In the general case, a D-dimensional self-similar object can be divided into N smaller parts, each scaled down by a factor of r, where $r=1/N^{1/D}$. Therefore, given a self-similar object of N parts, each scaled by a ratio r, the fractal or similarity dimension D_f is given by

$$D_f = \log(N) / \log(1/r) \tag{3.1}$$

Fractal dimensions are unlike Euclidean dimensions in that they are not restricted to integer values. Consider the von Koch curve of Figure 3.2. Any segment of the curve is composed of 4 sub-segments, each scaled down from its parent by the factor $r = l/3$. Therefore, this curve has the fractal dimension $D_f = \log(4) / \log(3)$, or approximately 1.26.

An intuitive notion of fractal dimension is conveyed by illustrating curves with increasing fractal dimension (see Fig. 3.3). As D_f increases from 1 to 2, the corresponding curves change from being “line-like” to “filling” much of a 2-dimensional plane.

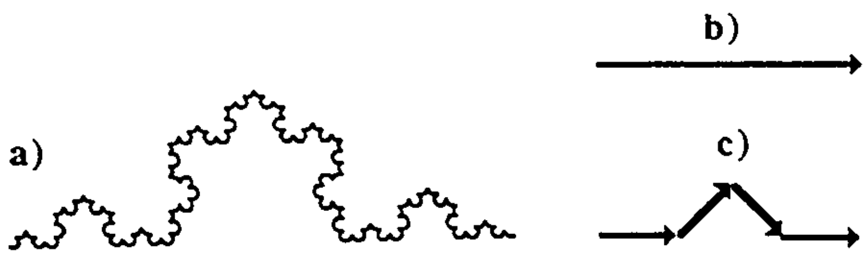

Fig. 3.2. a) von Koch curve Fractal dimension $D_f \sim 1.26$. The curve is constructed by iteratively replacing each straight line (b) with the four sub-segments in (c).

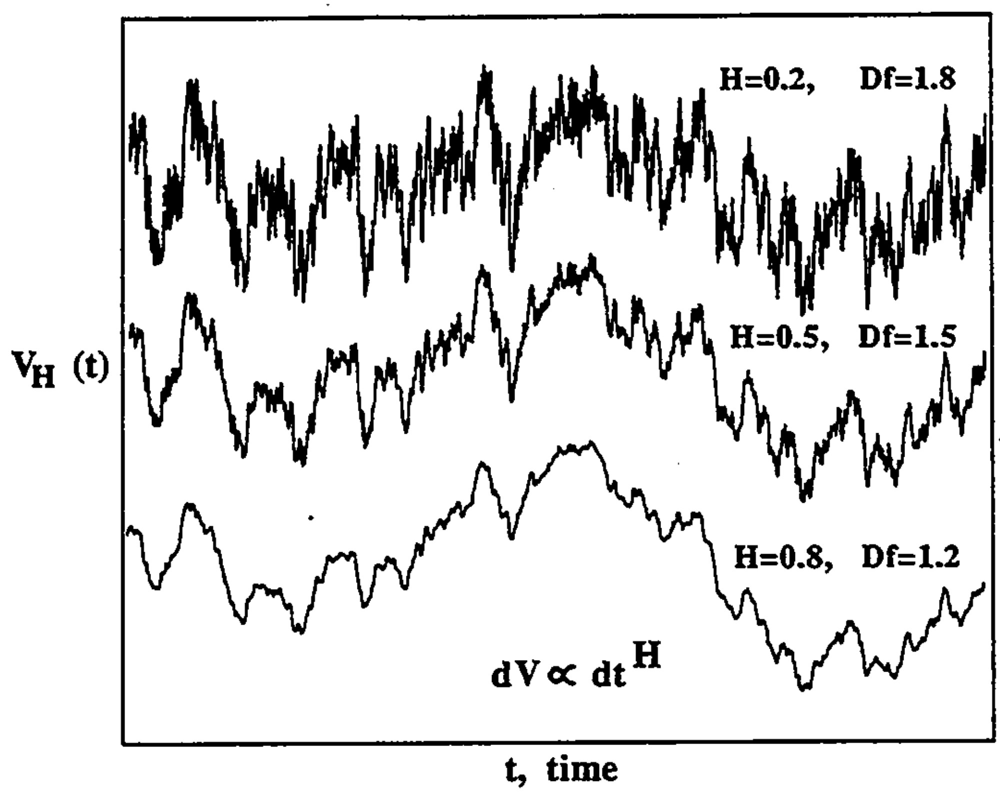

Fig. 3.3 Fractal profiles of various fractal dimensions. Each profile can be considered a single valued function V(t) of one variable, t, time. For these functions the average change in V, $dV = V(t_2) - V(t_1)$, is related to the time difference $dt = t_2 - t_1$, by $dV \propto dt^H$. (After Voss, 1988). See text for more explanation.

3.3 Exact and statistical self-similarity

Fractals can be either exactly self-similar or statistically self-similar. Fractals generated by a precise recursive geometrical procedure, such as the von Koch curve (Fig. 3.2), are exactly self-similar in that each small portion of the object, when magnified, is exactly equal to a larger portion. Exactly self-similar fractals are mathematical entities and are not yet observed in nature. Natural fractals, also known as random fractals,

Fig. 3.4 Shore line of a simulated fractal surface having $D_f = 2.2$. This is an example of statistically self-similar fractal. Instead of appearing exactly self-similar under magnification changes (as does the von Koch curve), this pattern has identical statistical properties over a range of scales. (Modified after Voss, 1988).

are statistically self-similar. The synthetic coastline in Figure 3.4 is an example of a statistically self-similar fractal. Upon magnification, a small portion of the coast looks similar to, but not exactly like, a larger portion of the object. Much of the theory regarding random fractals is derived from the studies of fractional Brownian motion (fBm) (Mandelbrot and van Ness, 1968). Figure 3.3 illustrates several sample traces of fBm, each being a single valued function $V_H(t)$ of one variable t, in this case time. The scaling properties of the different traces in Figure 3.3 are characterized by a parameter H, in the range $0 < H < 1$. When H is close to 1 the traces are relatively smooth. When H is close to zero the traces are the roughest. H relates the average change in V, $dV=V(t_2) - V(t_1)$, to the time difference $dt = t_2 - t_1$ by the scaling law (Voss, 1988)

$$dV \propto dt^H. \tag{3.2}$$

Furthermore, the fractal dimension D_f of a fBm trace is related to the scaling parameter H as

$$D_f = 2 - H, \tag{3.3}$$

(Voss, 1988).

3.4 Self-affinity and zerosets

The scaling properties of fBm are different from those of exactly self-similar factals like the von Koch curve of Figure 3.2, or statistically self-similar objects like the coastlines of Figure 3.3. Under magnification, small segments of self-similar fractals are exactly or statistically similar to larger segments. Self-affine fractals, such as a fBm trace, are statistically similar only if the t and V directions are magnified by different scaling factors. Voss (1988) describes self-affinitiy as "non-uniform scaling, where shapes are statistically invariant under transformations that scale different coordinates by different amounts". Mandelbrot recognized a similarity between self-affine fBm traces and mountainous horizons. Mathematically, an alpine terrain can be modelled as the function V(x,y), which represents the altitude at any given x and y coordinate. If a hiker travels any distance dr in the xy-plane ($dr^2=dx^2+dy^2$) then the expected altitude variation dV is given by

$$dV \propto dr^H. \tag{3.4}$$

Note the similarity between this relationship and the relationship for fBm (eq 3.2). In this case, the fractal dimension of the landscape must be greater than the Euclidian dimension 2 of a surface. Therefore, the landscape has the fractal dimension $D_f = 3 - H$. Furthermore, the fractal landscape is self-affine because the altitude scales differently than the x and y coordinates. The non-uniform scaling (i.e. self-affinity) of the landscape becomes evident when the viewing distance is varied. When viewed from nearby, (e.g. on a ski lift), the fractal landscape appears quite rough. However, when viewed from a satellite the earth's surface appears quite flat. Because $H<1$, the vertical scale increases by less than the horizontal scale and the mountains appear to flatten as the viewing distance is increased. Intersecting the self-affine landscape with a horizontal plane eliminates the vertical axis leaving a family of curves (coastlines) that scale equally in the x and y directions and are therefore self-similar. This type of coastline is referred to as a zeroset.

3.5 Estimating fractal dimension

There are several methods of estimating the fractal dimension of self-similar fractal objects. All of them are based on the relationship

$$N = 1 / r^{D_f} \tag{3.5}$$

and taking logarithms of both sides,

$$D_f = \log(N) / \log(1/r), \tag{3.6}$$

where N is the number of self-similar parts, each scaled down by a factor of r, that comprise the object.

3.6 Measuring D_f of self-similar curves

3.6.1 Mandelbrot-Richardson plot (caliper method)

Consider a self-similar fractal curve, such as a coastline (see Fig. 3.5). This curve has some maximum length L_{max}. The curve can be measured using smaller sized rulers of length (L), where

$$L = r * L_{max} \qquad \text{for } r < 1 \tag{3.7}$$

and r is a scaling factor.

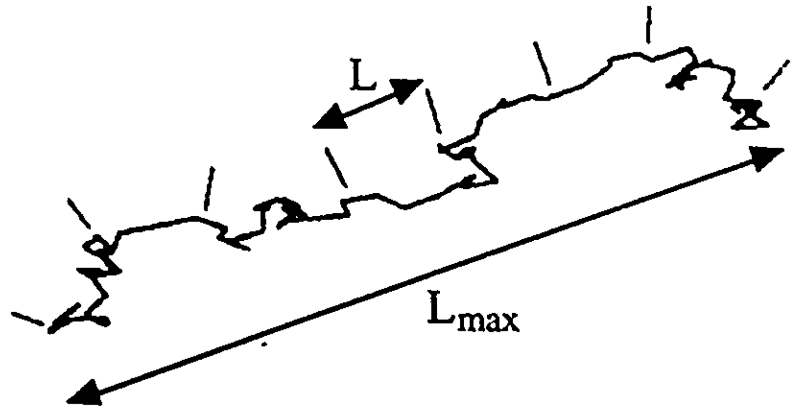

Fig. 3.5 A fractal curve of linear size Lmax can be measured using rulers of length L. The measured perimeter, P, equals N x L, where N is the number of ruler increments required to measure the curve. Notice that there are variations along the curve that are smaller than L, and simply spanned by the ruler. As the ruler size decreases, more details of the curve are accounted for in the perimeter calculation. For fractal curves, P is proportional to $1/L^{D_f-1}$, where D_f is the fractal dimension. Therefore, the fractal dimension D_f can be estimated from 1 - the slope of a log(P) (ordinate) vs. log(L) (abscissa) plot over a range of ruler sizes, L. See text for full explanation.

The measured perimeter (P) of the curve can be determined by

$$P = L * N \tag{3.8}$$

where N is the number of caliper steps of length (L) it takes to measure the object. From eq 3.5 we know that for fractals,

$$N = 1 / r^{D_f}.$$

Therefore, combining eqs 3.5, 3.7, and 3.8 yields

$$P = L * (L_{max} / L)^{D_f}, \tag{3.9}$$

or

$$P \propto 1 / L^{D_f - 1} \tag{3.10}$$

Taking logarithms yields

$$\log(P) \propto (D_f - 1) * \log(L) \tag{3.11}$$

Therefore, the fractal dimension $D_f = 1$ - the slope of a log(P) (ordinate) vs. log(L) (abscissa) plot over a range of ruler sizes (L), (Mandelbrot, 1982).

3.6.2 Box method (grid dimension)

The box method (Voss, 1988) is analogous to the ruler method in that the fractal dimension D_f is estimated by counting the number of boxes (N) of width (L) containing an element of the curve (Fig. 3.6). The slope of a log(N) (ordinate) vs. log(1/L) (abscissa) plot over a range of box widths yields an estimate of the fractal dimension. See Appendix E for a listing of a box method computer program.

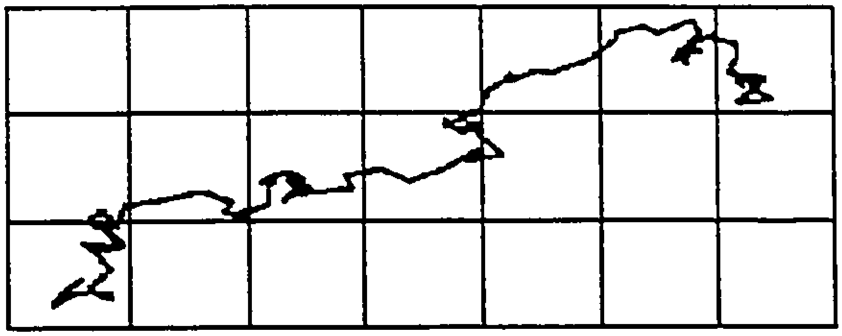

Fig. 3.6 The box method requires counting the number of boxes, N, of side length L containing a piece of the curve. For fractal objects, the slope of a log(N) (ordinate) vs. log(1/L) (abscissa) plot over a range of box widths yields an estimate of the fractal dimension.

3.7 D_f estimates for self-affine curves

Self-affine curves, such as mountain profiles or fractional Brownian motion traces, do not scale equally in the horizontal and vertical directions. Consequently, direct application of the above methods yields different estimates of D_f, depending on the technique and ruler sizes used (Voss, 1988). Voss, (1988) suggests that these self-affine curves should be reduced to zerosets of self-similar points. This is accomplished by intersecting the curve with a straight line parallel to one of the axis. The fractal dimension D_Z of the zeroset, which must be less than 1 but greater than zero, can then be estimated using the box method. The fractal dimension of the original curve is calculated by

$$D_f = D_z + 1 \tag{3.12}$$

3.8 Estimating D_f of fractal surfaces

The initial use of fractals in quantitative fractography involved the measurement of the fractal dimension of fracture profiles (e.g. Chermant and Coster, 1979; Coster and Chermant, 1983; Brown and Scholz, 1985). This technique has recently been applied to surfaces of fractured concrete (Saouma *et al*, 1990) and metal (Dauskardt,1990).

3.8.1 Slit island method

This method was introduced by Mandelbrot *et al* (1984) in their study of fracture surfaces in metal. Zerosets are created by intersecting the fracture surface with planes that are parallel to the main plane of fracturing. The zerosets emerge as islands having fractal coastlines. The area - perimeter relationship of these islands can be used to estimate the fractal dimension. Consider a fractal curve as in the previous section (see Fig. 3.5). The perimeter of the curve depends on the length of the ruler (L) and the fractal dimension D_f, as in eq 3.9,

$$P = L * (L_{max} / L)^{D_f}$$

or, if always using the same size ruler (L),

$$P \propto L_{max}^{D_f} \qquad (3.13)$$

Therefore, the fractal coastline of islands measured at different slit heights have perimeters (P) governed by eq 3.13. The area (A) of the emerging islands varies according to

$$A \propto L_{max}^2 \tag{3.14}$$

or

$$A^{1/2} \propto L_{max} \tag{3.15}$$

Combining eqs 3.13 and 3.15 yields.

$$P \propto A^{D_f/2} \tag{3.16}$$

And taking logarithms,

$$\log(P) \propto (D_f/2) * \log(A) \tag{3.17}$$

Therefore, the slope of a log(P) (ordinate) vs. log(A) (abscissa) plot for islands of various sizes yields ($D_f/2$) and

$$2*(\log(P)/\log(A)) = D_f \tag{3.18}$$

The benefits and limitations of the slit island method are currently being reviewed by many investigators in the field of material science (Pande, *et al*, 1987; Lung and Mu, 1988 and Meisel, 1991). Lung and Mu

(1988) state that the measured fractal dimension of the slit islands does not correspond to the actual fractal dimension of the fracture surface. Meisel, (1991), refutes this claim using mathematical examples. In either case, it is this author's opinion that the slit island method is becoming one of the standard procedures for quantitative fractography.

3.8.2 Estimating D_f of real fracture surfaces

Joint surfaces having plumose structures appear quite rough when viewed under a microscope. However, the surfaces often appear remarkably planar when observed from afar. This nonuniform scaling suggests that these surfaces are self-affine fractals. Therefore, their corresponding fractal dimensions are measured using the slit island method.

The following flow chart illustrates the slit island method for determining D_f of joint surfaces.

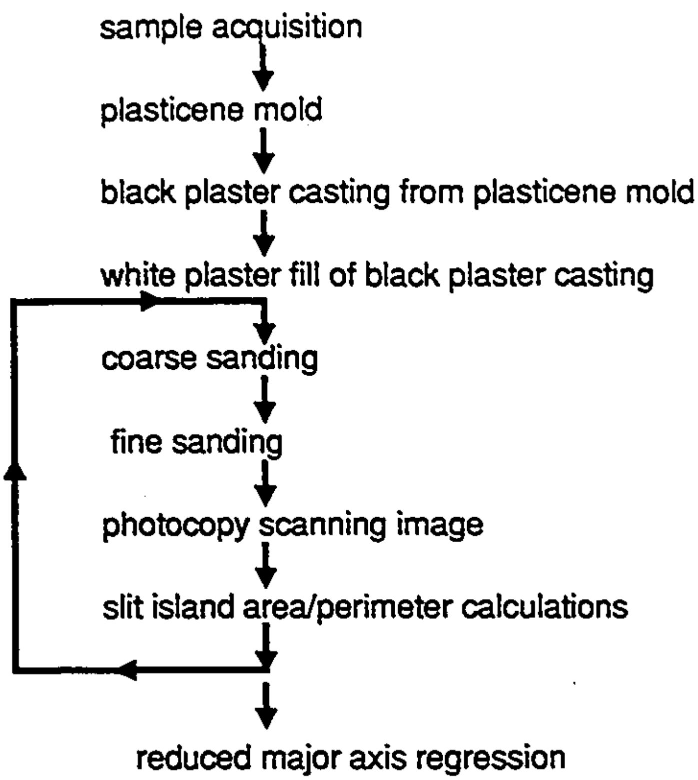

In essence, the slit island method involves making a binary plaster cast (one side black, one side white) of the original surface. Zerosets of the fracture surface are obtained by sanding the block parallel to the main joint surface. At various levels (approximately, 0.1 mm apart), the emerging zeroset islands are imaged, (either photographically or photomechanically). They are then scanned into a computer for area/perimeter analysis. The lower (0.085 mm) and upper (280 mm) limits of the analytical procedure are determined by the resolution and size of the image scanner, respectively. The perimeter is calculated by counting the number of pixel edges (ruler size ~ 0.085 mm) that constitute the island boundary. The area is calculated by counting the number of pixels, (each having an area ~ 0.007 mm^2), which fill the island.

CHAPTER 4
PLUMOSE JOINT FRACTAL ANALYSIS

4.1 Sample description

A jointed surface in carbonate-cemented arkose from the Cambro-Ordivician Potsdam Formation at Old Fort Henry, Kingston, Ontario Canada (Liberty, 1971) was selected for analysis (see Fig. 4.1). The rock has a bimodal grain size distribution.

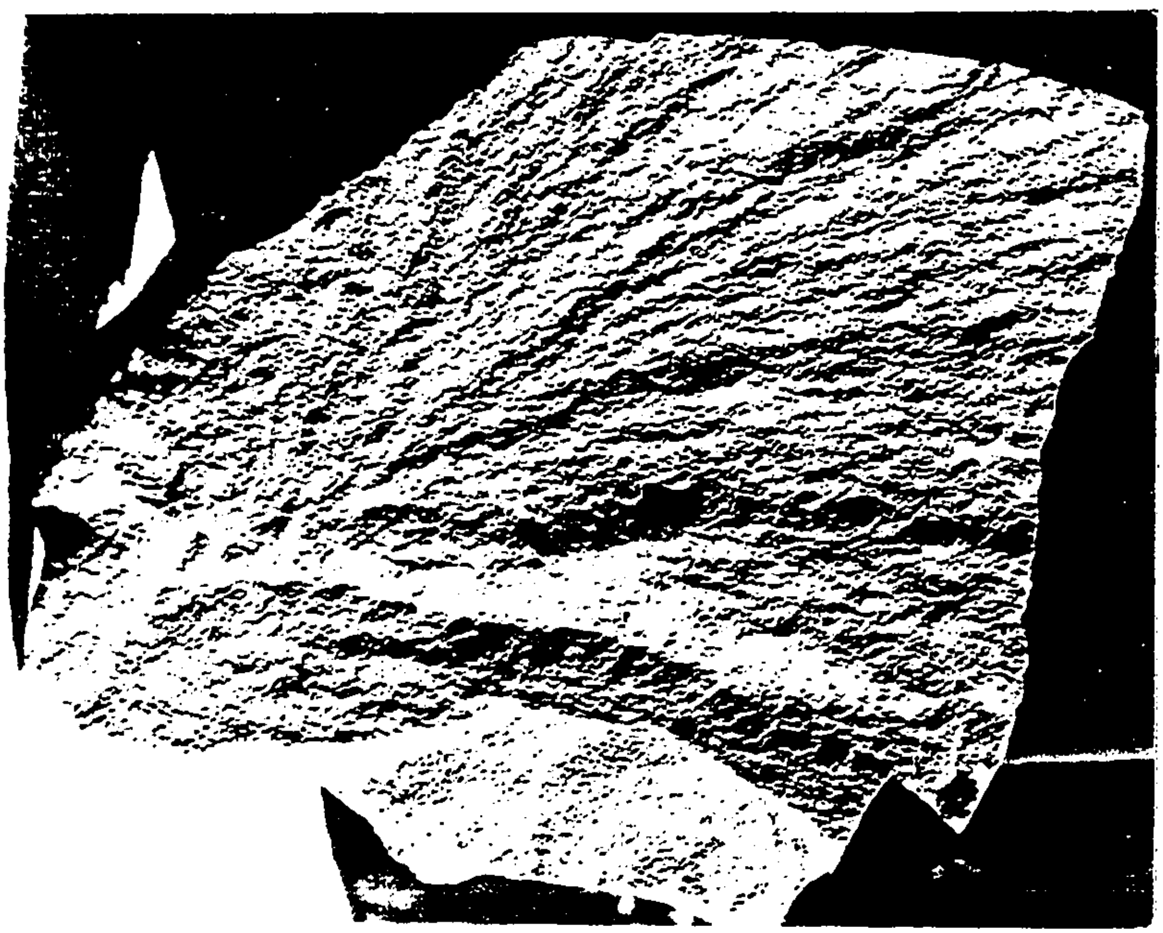

Fig. 4.1 Jointed surface in carbonate-cemented arkose. (Width of photo approximately 15 cm)

Most of the rock is fine-grained (<0.1 mm diameter) quartz, carbonate, plagioclase and biotite. There are also scattered rounded quartz grains which are an order of magnitude larger (>1 mm diameter) than the matrix (see Fig. 4.2).

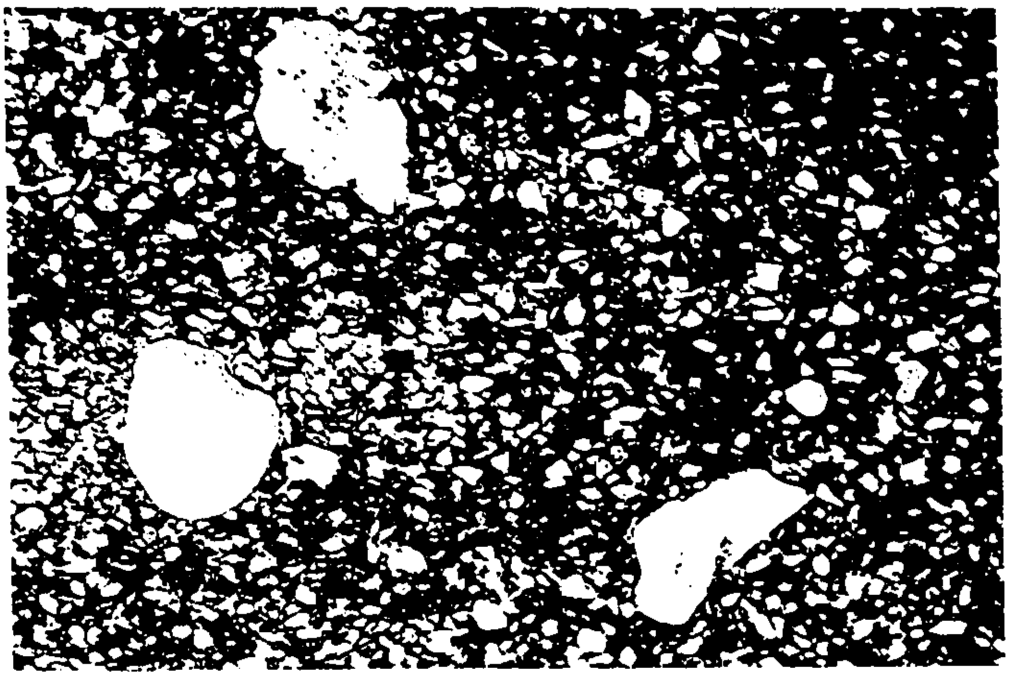

Fig. 4.2 Photomicrograph of joint-hosting lithology. Note the bimodal grain size distribution, with most grains < 0.1 mm diameter, and a few grains > 1 mm diameter. Field of view approximately 6 mm.

This rock was selected for analysis because its jointed surfaces have a) significant relief in their plumose structure, b) no large scale twist hackle, and c) no evidence of velocity features, namely "mirror", "mist" or "hackle" zones.

4.2 Analysis

A typical slit island section of a plumose joint from the rock is illustrated in Fig. 4.3.

Fig. 4.3 Typical slit island section of the plumose joint in Fig. 4.1.

The ln(perimeter) vs. ln(area) plot for the plumose joint is shown in Fig. 4.4. Since both axes contain uncertainty, a reduced major axis regression (York, 1966) was used to regress the data. The slope equals 0.62 ± .07 (at 2σ). Therefore, from eq 3.18, the fractal dimension of the jointed surface is estimated at 1 + 2 * slope, or 2.24 ± 0.14. In order to fully describe the fractal aspect of the surface it is also necessary to state the range over which fractal scaling is observed. The range of island areas varies from 15 to 7000 pixels. Each pixel represents approximately 0.007 mm^2. Therefore the joint surface is fractal between approximately 0.1 mm^2 and 49 mm^2, (i.e. approximately 3 orders of magnitude).

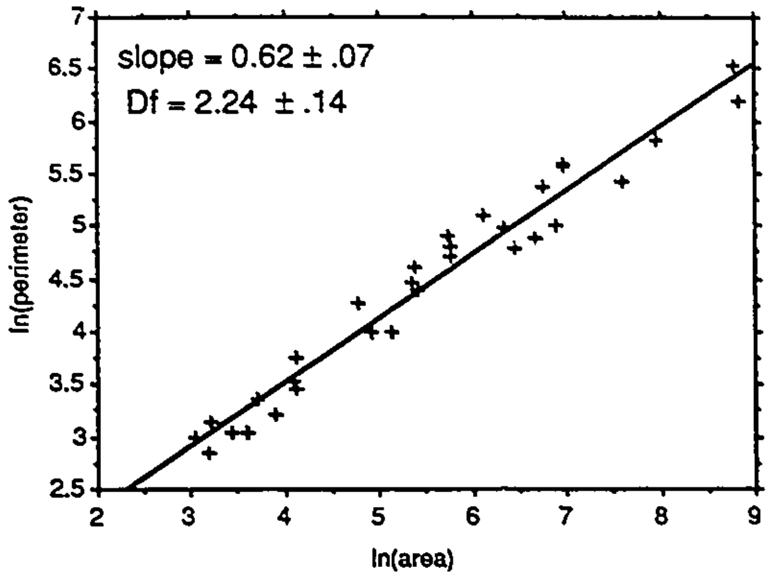

Fig. 4.4 Ln(perimeter) vs. ln(area) plot for plumose joint of Fig. 4.1. Slope equals $0.62 \pm .07$ (2σ), therefore, D_f of the surface equals 2.24 ± 0.14.

4.3 Discussion

The fractal aspect of the joint surface and the actual measured fractal dimension are in accordance with those determined by Mandelbrot *et al* (1984) for fractures in steel. They obtained D_f values ranging between 2.10 and 2.28. In their study, Mandelbrot *et al* demonstrate that the fractal nature of the fracture surface is more than just a mathematical curiosity. Fig. 4.5 shows their observed correlation between a known metallurgical property (in this case impact energy) and the fractal dimension of the resulting surface. Mandelbrot *et al* (1984) suggest that further investigation into microstructural aspects of fracturing are needed to fully explain this relationship.

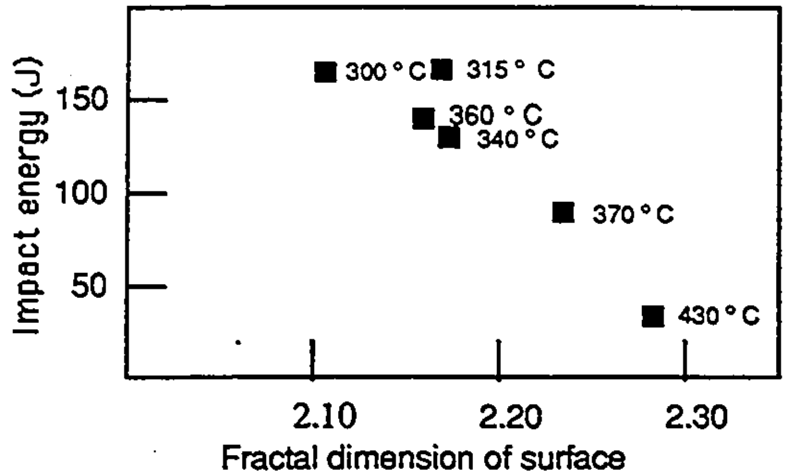

Fig. 4.5 Impact energy vs. fractal dimension. 300 - grade maraging steel, room temperature, Charpy impact. (After Mandelbrot *et al*, 1984).

More recent studies, (Bouchaud *et al*, 1990; Dauskardt *et al*, 1990; Mu and Lung, 1988; and Long *et al*, 1991) demonstrate a similar range of D_f values for a variety of metal fracture surfaces. Brown and Scholz (1985) demonstrate that profiles of rock fracture surfaces have measured fractal dimensions as great as 1.68. As with metal fractures, it is likely that this range would be related to microstructural aspects of fracture propagation in rock. There are several possible ways of comparing the fractal dimension of jointed surfaces with known microstructural properties of rock. One could measure the fractal dimension of various joints, and relate these values to measured parameters such as permeability, porosity, grain size variation, etc. However, the errors associated with mapping of microstructures in complex media such as rock renders this approach untenable. Alternatively, one could attempt to manufacture and fracture "pseudo-rocks" having predetermined microstructural properties and distributions. However, precise control of such an experiment is made difficult by technical problems such as reflected stress waves, boundary conditions of test rigs, emplacement of defects, and controlling strain rate and fracture propagation velocity. Furthermore, both of these methods suffer from a common drawback. They are of the "before and after" type, that is, they do not readily facilitate the observation of fracture propagation or the measurement of dynamic parameters. Any correlations between microstructural properties and fractal dimensions would be made without fully understanding the details of fracture propagation.

Therefore in order to explore the relationship between microstructures, fracture propagation and fractal dimensions, I have chosen to simulate fracture propagation using a growth algorithm on a digital computer.

CHAPTER 5
COMPUTER SIMULATION

Simulations help to build an understanding of the process being studied. Simulations have been particularly useful for understanding dynamic growth processes, such as crystal growth (Nittman and Stanley,1986), viscous fingering (Van Damme, 1989), dielectric breakdown (Niemeyer *et al*, 1984) and diffusion-limited aggregation (DLA)(Witten and Sander, 1981). In these systems, the interaction between the growing object and its medium is not apparent from the initial set of equations or rules. Furthermore, sometimes even the humblest of recursive growth algorithms (such as DLA) yields startling results during iterative growth.

Computer simulations are flexible. They permit the investigator to observe the effects of slight changes in growth algorithms. An understanding of the growth dynamics gradually or spontaneously emerges after experiencing many cycles of adjustment and observation. The fracture propagation algorithm in this thesis is a hybrid. It is based on the properties of linear elastic fracture mechanics, however, its development is determined in part by insight realized through observing countless computer runs (n >1000) on numerous predecessor algorithms. In spite of its inherent simplifications, this computer simulation offers a flexible approach to analyzing the complex problem of joint propagation in rock.

5.1 Algorithm assumptions

Joint propagation in rock is very complicated. This complexity is due in part to the inherently complicated nature of the rock medium itself. Therefore, any computer simulation of joint propagation involves simplification of the physical inhomogeneities of rock. Rocks that readily display plumose joints are generally fine-grained and of uniform grain size. Good host lithologies include shale, fine-grained limestone, and fine-grained volcanic rocks. In a structural sense, these rocks are considered homogeneous or isotropic. However, the very existence of plumose structures attests to the presence of imperfections within this perceived homogeneity. These rocks must contain defects, such as grain boundaries, pore spaces, and micro-cracks that are large enough to alter stresses in the process zone and hence alter the path of the propagating fracture. In the present simulation the natural complexity of rock is quantified by assigning a uniform spatial distribution to the defects.

Development of the simulator was achieved by partitioning the fracture process into a number of steps, hence an algorithm, and then converting this to computer code. The fracture mechanic principles (see chapter 2) used in formulating the growth algorithm are described in the following list of joint growth assumptions.

1) Joints do not form instantaneously (Woodworth, 1896; Barton, 1983; Pollard and Aydin, 1988). Their complex surfaces are the sum of a finite number of fracture increments. Each fracture increment is proportional in size to a hypothetical zone of inelastic

deformation (a process zone), which is very much smaller than the overall joint (Lawn and Wilshaw, 1975).

2) Stress intensity factors are well below the critical value where velocity hackle and/or fracture bifurcation occurs. Consequently, the joint is a single fracture.

3) Joints form predominantly through mode I fracture. In the absence of structural anisotropies (hereinafter referred to as defects) and ignoring velocity effects, a mode I fracture tends to propagate in a plane perpendicular to the remote least compressive stress direction (Lawn and Wilshaw, 1975).

4) In the immediate vicinity of a defect, the local stress orientation may deviate from parallelism with the remote stresses, resulting in tilted or twisted fracture increments (Kulander *et al*, 1979). Beyond the vicinity of the defect, local stresses re-align with the remote stresses and the fracture again propagates perpendicular to the remote least compressive stress. Therefore, the defect creates a displaced fracture segment (or tail, Preston, 1939; or wake Frechette, 1972; or inclusion hackle, Barton, 1983) extending beyond the inclusion, in the direction of fracture propagation. Displacements due to defects are assumed to be uniformly distributed, that is, an individual displacement has equal probability of being any magnitude between two limits.

5) Defects such as inclusions, pore spaces, and grain boundaries are plentiful in rock. In this simulation, defects are assumed to be the size of the process zone. Furthermore, defect distribution is approximated as uniform (i.e. randomly-distributed).

5.2 Iterative growth

The above assumptions form the basis for the design of the computer simulator. To simulate fracture propagation, these assumptions are incorporated into a recursive growth algorithm. This algorithm is best explained by examining the first couple of iterations of joint propagation.

In the simulation, the material being fractured is represented by a 3-dimensional array having orthogonal axes [x,y,z], where the xy-plane is perpendicular to $\sigma_3{}^r$ and z is parallel to $\sigma_3{}^r$ (see Fig. 5.1). Since a joint is single surface (see assumption 2), its entire surface can be projected onto the xy-plane and displayed on a 2-dimensional computer graphics screen.

As with real joints, the simulated joint is initiated at a point. In the simulator, the initial fracture increment has coordinates [x,y,z] and is perpendicular to a hypothetical $\sigma_3{}^r$. On the graphics screen, the initial fracture increment, and all subsequent fracture increments, are projected as single pixels (i.e. picture elements, or single dots). Thus, each pixel represents a single fracture increment equivalent in size to a hypothetical process zone.

After initiation, a joint propagates outward. In the example of Fig. 5.2, the joint surface can propagate from the origin into any of the 8 potential growth sites (i.e. neighbouring pixels). This presents an immediate problem - how is the direction of growth determined? Neighbouring pixels are incorporated into the joint surface through

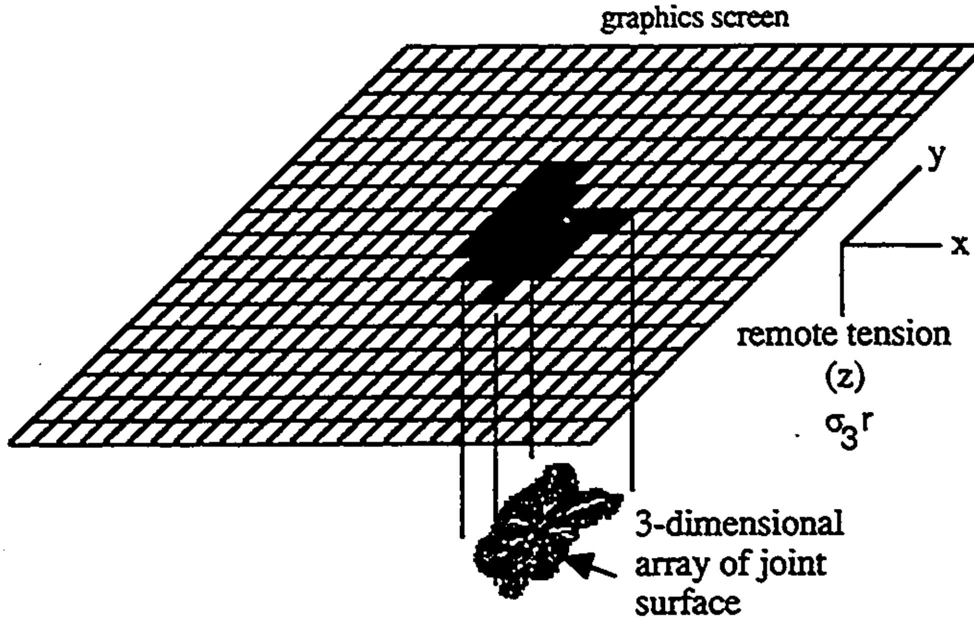

Fig. 5.1 Projection of 3-dimensional array onto graphics screen, (which is oriented perpendicular to remote tension).

random selection, where each neighbouring pixel (or potential fracture increment) has equal probability of being selected. Furthermore, only an assigned percentage of all potential fracture increments are incorporated during a single iteration (see Fig. 5.2). All potential fracture sites, in projection, are eventually fractured.

Most joints are a single fracture surface (see assumption 2). In the simulation, this assumption restricts the propagating fracture from extending above or below any portion of the already formed joint surface. More importantly, this causes the joint surface to propagate outwards, away from the origin. In the absence of defects, the new fracture increments are parallel, (hence, also perpendicular to hypothetical $\sigma_3{}^r$) and at the same level, in the z direction, as the pre-existing fracture increment that served as its parent (see Fig. 5.3).

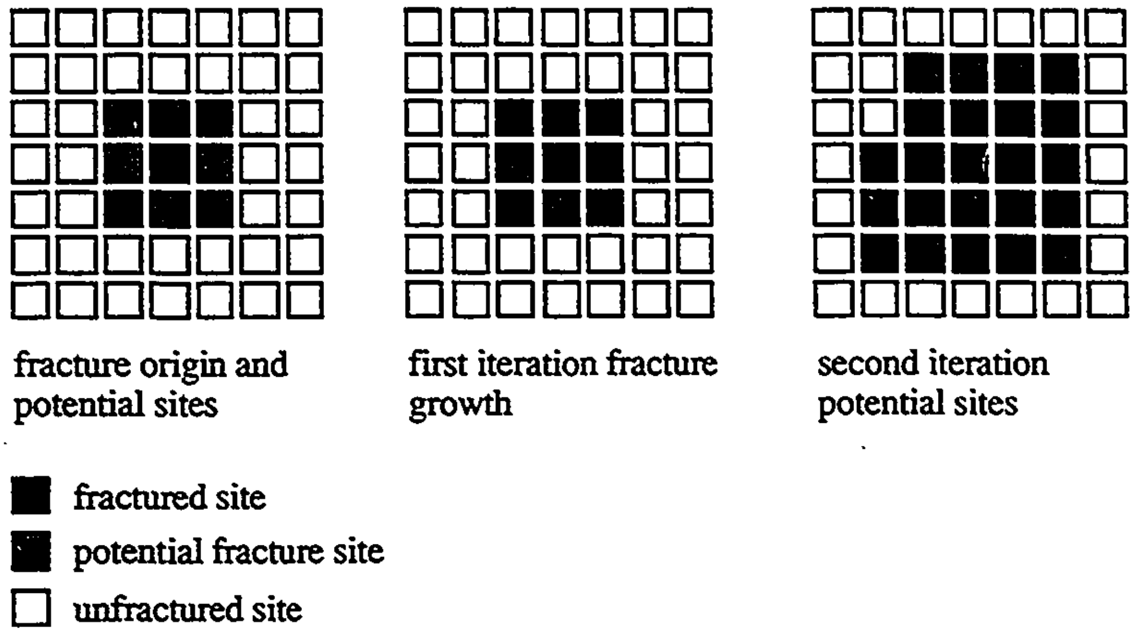

Fig. 5.2 Sketch of hypothetical first one and a half iterations of fracture growth algorithm. a) Surrounding the origin are 8 neighbouring potential fracture sites. b) Algorithm randomly selects 50% of these sites to become fracture sites. c) Process is repeated, and all sites neighbouring fracture sites become potential fracture sites.

During fracture propagation, there is a probability, (proportional to defect density), that the fracture front will encounter a defect large enough to significantly alter the process zone stresses, and hence the propagation path. In rocks, the net result of a defect is a displaced fracture increment (see assumption 4). In the simulation, a defect causes the new fracture increment to be displaced a randomly-selected distance, in the z-direction, from its previous z level (see Fig. 5.3). The fracture increment is then re-aligned with remote stresses (i.e. perpendicular to $\sigma_3{}^r$). In accordance with these rules, the fracture propagates outwards yielding a 3-dimensional array of the simulated joint surface. Figure 5.4 illustrates the visual similarity between a simulated and a natural joint surface. A quantitative comparison follows.

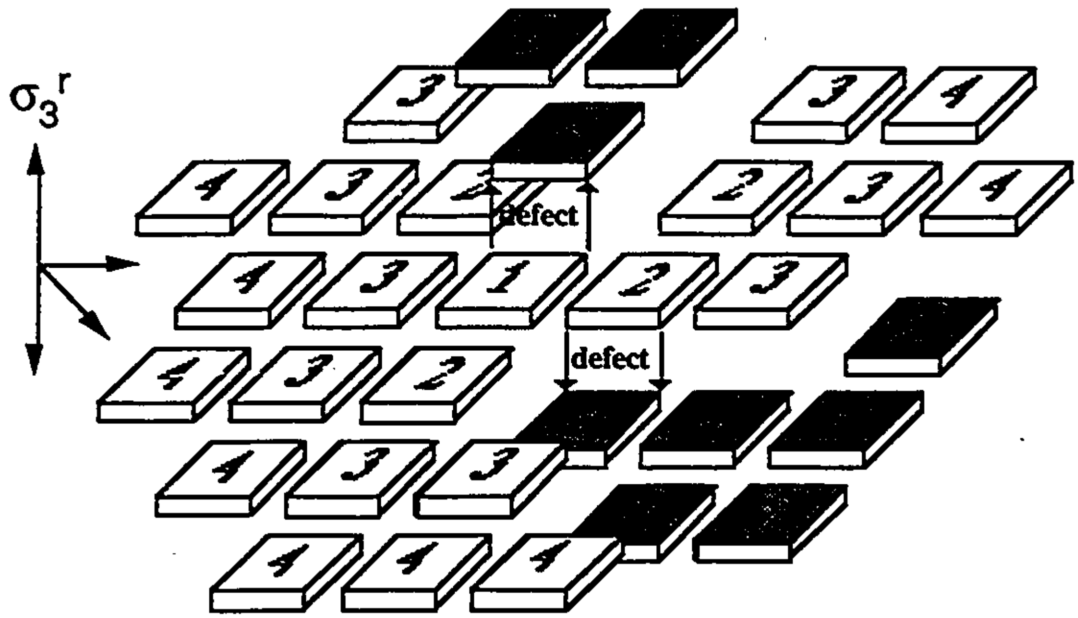

Fig. 5.3. Schematic of plumose joint simulation. Each tablet represents an individual fracture increment oriented perpendicular to remote least compressive stress. Numbers represent iteration when fracture increment occurred. During the first and third generations, randomly-distributed defects were encountered and two of the fracture increments were displaced out of the initial plane of fracture.

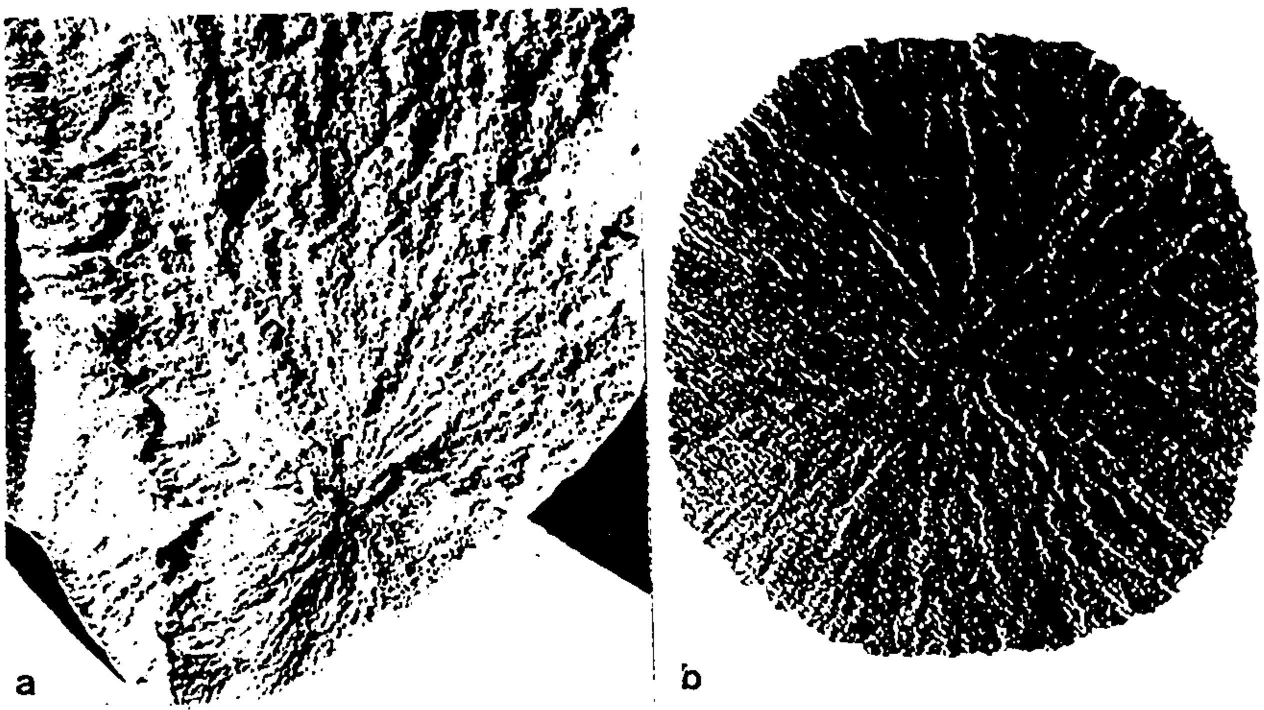

Fig. 5.4 Visual comparison between (a) actual plumose joint (field of view approximately 10 cm and (b) simulated plumose joint (defect density = 0.1%).

5.3 Slit island constructions and shaded relief maps

To produce slit island sections, the data are re-plotted on the graphics screen with only those points of the joint surface above some selected z-level illuminated. On average, 20 sections are constructed and 60 islands are used to estimated the fractal dimension of the surface.

Shaded relief maps are constructed by re-plotting the data while assigning a grey intensity proportional to the local gradient of the joint surface.

5.4 Software considerations

The simulation was initially coded in compiled GFA Basic on an Atari Mega ST4 computer. Typical runs of approximately 100,000 fracture tablets required 30 minutes execution time. Eventually, the simulation was rewritten in Think Pascal and run on a MacIntosh IIfx system, resulting in dramatic reduction of run times. A commented listing of the Think Pascal version is given in Appendix B.

5.5 On-lattice growth

The above algorithm is the basic growth algorithm. It is slightly modified in future sections (see sections 5.6.1.1 and 5.6.1.2). In one way this algorithm is similar to the algorithm of diffusion-limited aggregation (DLA) (Witten and Sander, 1981), which is used to simulate many growth phenomena (e.g. crystal growth, Fowler *et al*, 1989; dielectric breakdown, Niemeyer *et al*, 1984). A typical DLA pattern, produced by the algorithm written by the author and listed in Appendix C, is seen in Fig. 5.5. These aggregates are fractal with D_f approximately 1.7. In DLA, and in the present joint simulation, growth involves an incremental random process. During DLA, particles representing diffusing chemical constituents wander randomly (i.e. with Brownian motion) in the vicinity of the growing aggregate. Each time a constituent collides with the aggregate it "sticks" and becomes part of the aggregate (causing the aggregate to grow). When the DLA is grown on a square lattice, such as a computer screen, (as in Fig. 5.5), the resulting aggregate can appear more

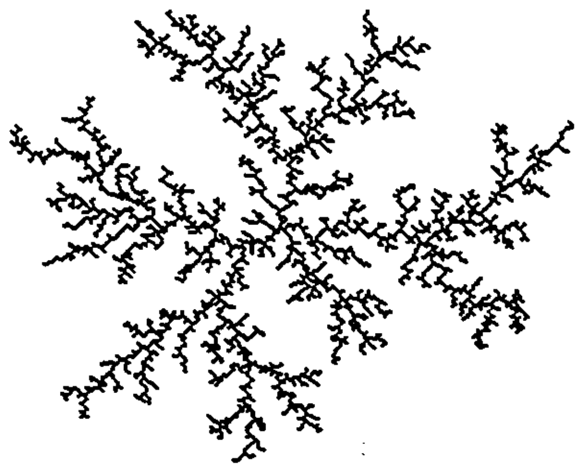

Fig. 5.5 Output pattern from diffusion-limited aggregation algorithm. D_f is approximately 1.7. Note that the pattern grows equally in all directions despite being grown on a square lattice.

rectilinear than aggregates grown off-lattice. However, for relatively small aggregate sizes (<10^7 sites), the estimated fractal dimensions of on-lattice DLA is in agreement with off-lattice DLA (Meakin *et al*, 1987). Therefore, the 300 x 300 square lattice (<10^5 sites) used in the present simulation should be sufficiently small so as not to compromise the fractal nature of the simulated joint surfaces. On-lattice growth is preferred because the resulting algorithms are much shorter and execution times are significantly reduced.

5.6 Simulation results

5.6.1 Parameters affecting D_f of simulated joint surfaces

Experimentation with the algorithm revealed 2 parameters that affect the fractal dimension of the resulting simulated joint surface. The first parameter, defect density, is a property of the medium. The second parameter is the fractal dimension of the simulated propagating fracture front. This parameter is a dynamic parameter, therefore it is only measurable during fracture propagation.

These two parameters, and their effects are discussed in the following sections.

5.6.1.1 Varying defect density

For mode I joints formed in perfect material (0% defects), and not subjected to any velocity effects, the dimension of the resulting surface is 2 (i.e. the Euclidean plane). This is the lower limit for the dimension of plumose joints formed predominantly under conditions of inclusion hackle.

There must also be an upper limit to the density of defects. Clearly, a rock cannot be 100% defect. Furthermore, an increase in defect density must eventually affect the material properties of the rock and hence the process zone size. An upper limit of 20 % defects was selected for the simulations. In the simulation, a 20% defect density corresponds to a probability of 0.2 that the current fracture increment (i.e. single pixel) is encountering a defect.

Results from simulation runs at defect densities of 0.2%, 2%, and 20% illustrate the effects of varying defect density. Figs. 5.6, 5.9, and 5.12 are shaded relief maps of the surfaces. Figs. 5.7, 5.10, and 5.13 are typical slit island sections through the respective joint surfaces, while Figs. 5.8, 5.11, and 5.14 are double logarithmic plots used to determine the respective fractal dimensions.

For a defect density of 0.2% (Fig. 5.6) notice that most of the surface is flat and individual defect sites can be located by tracing back the inclusion tails. For defect densities of 2% and 20%, (Figs. 5.9 and 5.12), the individual defect sites are unrecognizable. Furthermore, the slit islands formed at a defect density of 0.2% have perimeters which appear slightly smoother than those formed at defect densities of 20%. This subtle change is quantified by the fractal dimension of the surfaces, which increase as the defect density increases from 0.2% to 20%.

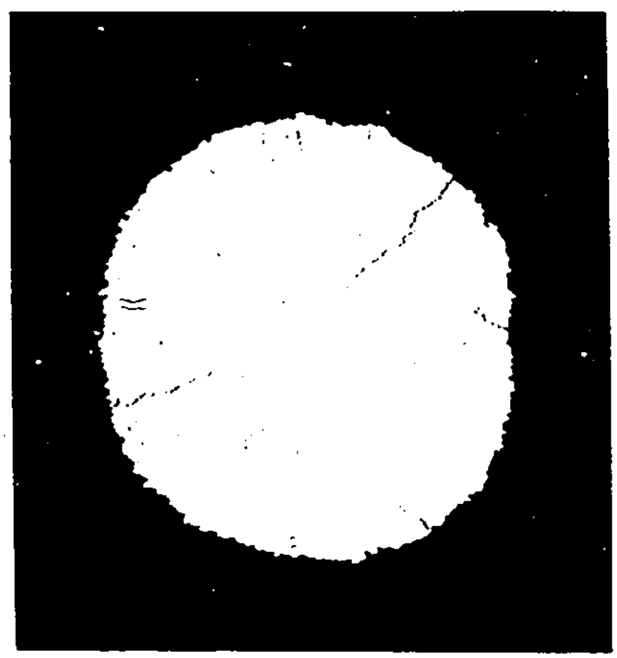

Fig. 5.6 Shaded relief map of computer generated plumose joint formed in medium containing 0.2% defects. Note that most of the surface is flat and individual defect sites can be located by tracing back the inclusion tails.

Fig. 5.7 Typical slit island section through computer generated plumose joint formed in medium containing 0.2% defects.

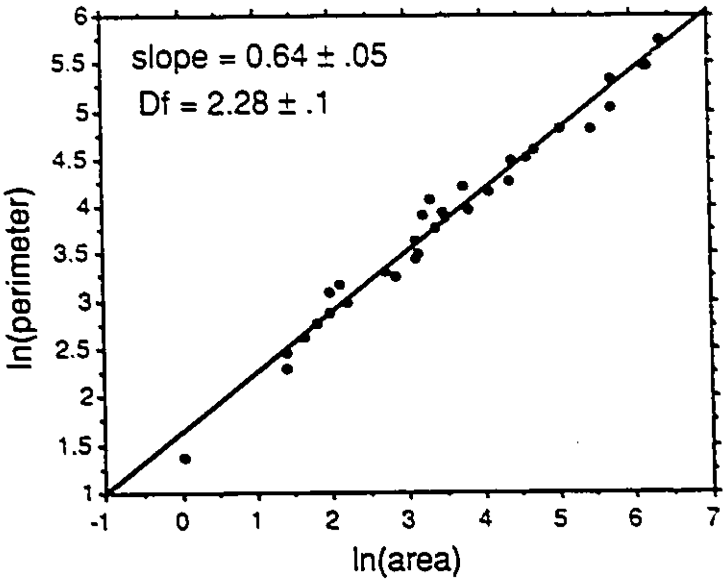

Fig. 5.8 Double logarithmic plot of perimeter vs. area for islands from slit island sections of plumose joint generated in medium containing 0.2 % defects. Reduced major axis regression yields slope 0.64 ± .05 (2σ). Therefore, the fractal dimension of the surface is approximately 2.28 ± .1.

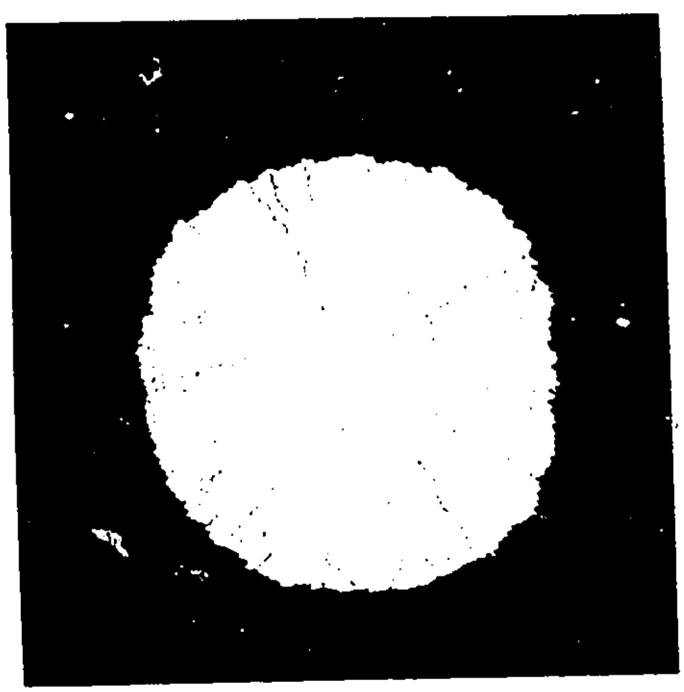

Fig. 5.9 Shaded relief map of computer generated plumose joint formed in medium containing 2% defects.

Fig. 5.10 Typical slit island section through computer generated plumose joint formed in medium containing 2% defects.

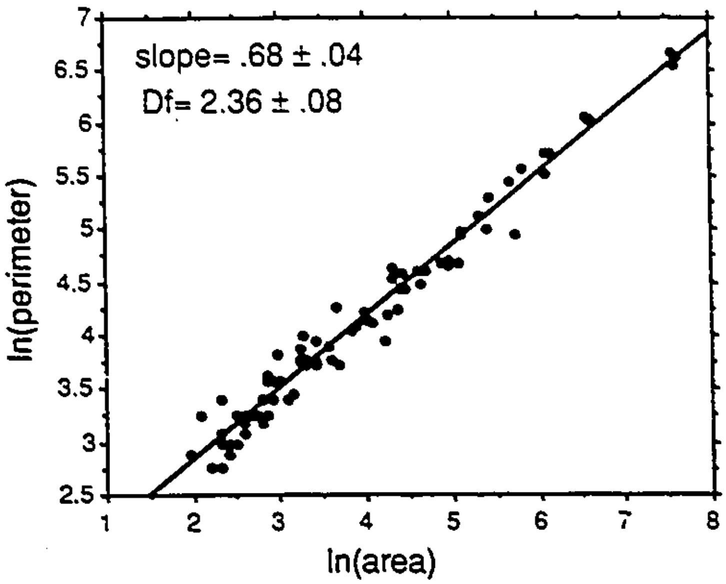

Fig. 5.11 Double logarithmic plot of perimeter vs. area for islands from slit island sections of plumose joint generated in medium containing 2% defects. Reduced major axis regression yields slope 0.68 ± .04. Therefore, the fractal dimension of surface is approximately 2.36 ± .04.

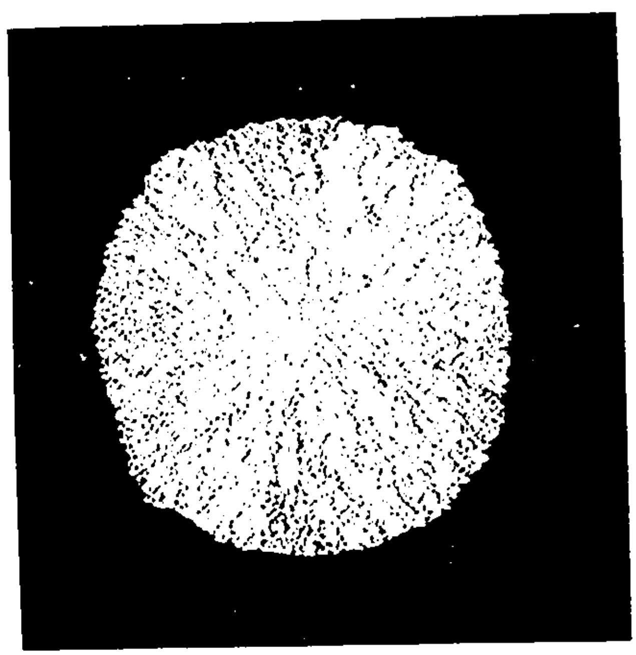

Fig. 5.12 Shaded relief map of computer generated plumose joint formed in medium containing 20% defects. Note that individual defect sites cannot be discriminated in the complex surface.

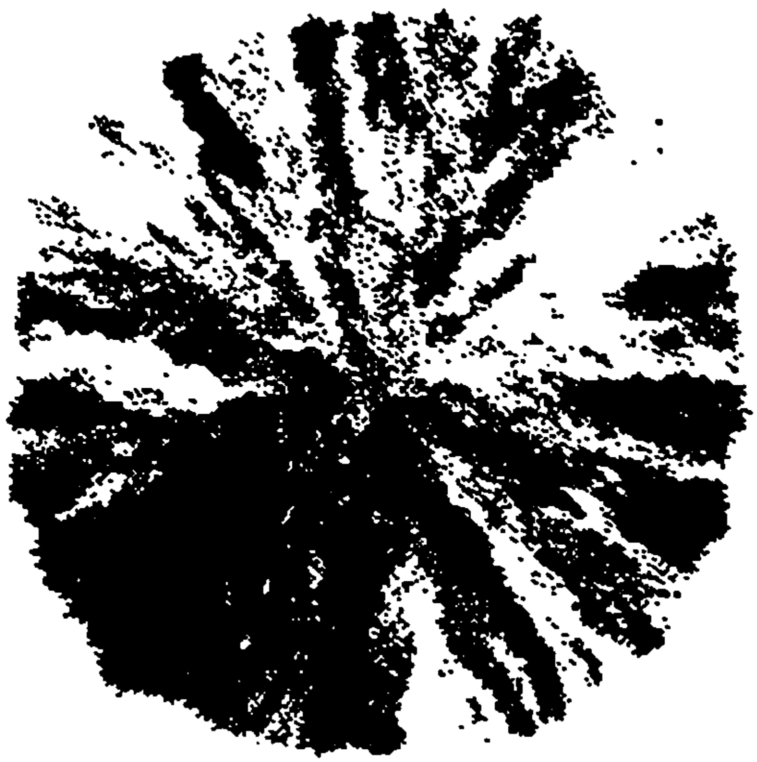

Fig. 5.13 Typical slit island section through computer generated plumose joint formed in medium containing 20% defects.

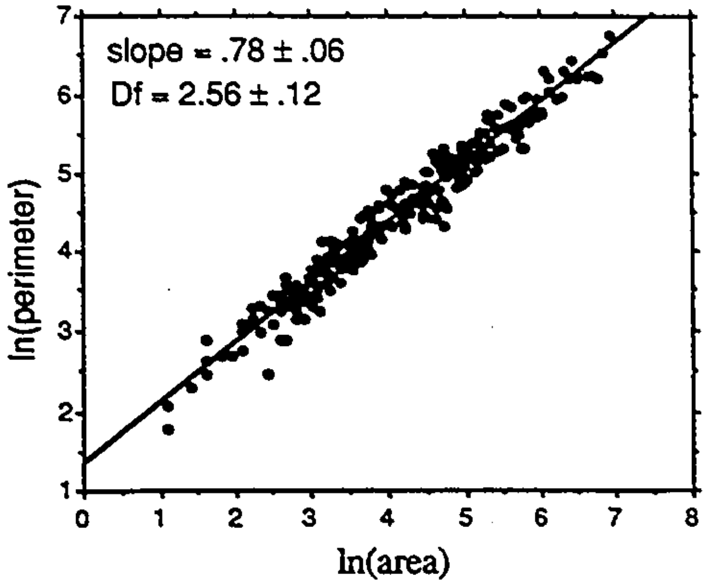

Fig. 5.14 Double logarithmic plot of perimeter vs. area for islands from slit island sections of plumose joint generated in medium containing 20% defects. Reduced major axis regression yields slope 0.78 ± .06. Therefore, the fractal dimension of surface is approximately 2.56 ± .12.

To establish the functional relationship between the dimensionality of the surface and the defect density, surfaces produced at varying defect densities were analyzed. Fig. 5.15 demonstrates a linear relationship between the logarithm of defect density and the fractal dimension of the resulting surface. Physically, this is because an increased defect density causes more deviations during fracturing, and hence a rougher surface. A more rigorous mathematical explanation of the functional relationship demonstrated in Fig. 5.15 is lacking. However, many well established geometrical models for creating fractals, such as diffusion-limited aggregation, cannot rigorously account for the fractal dimensions measured.

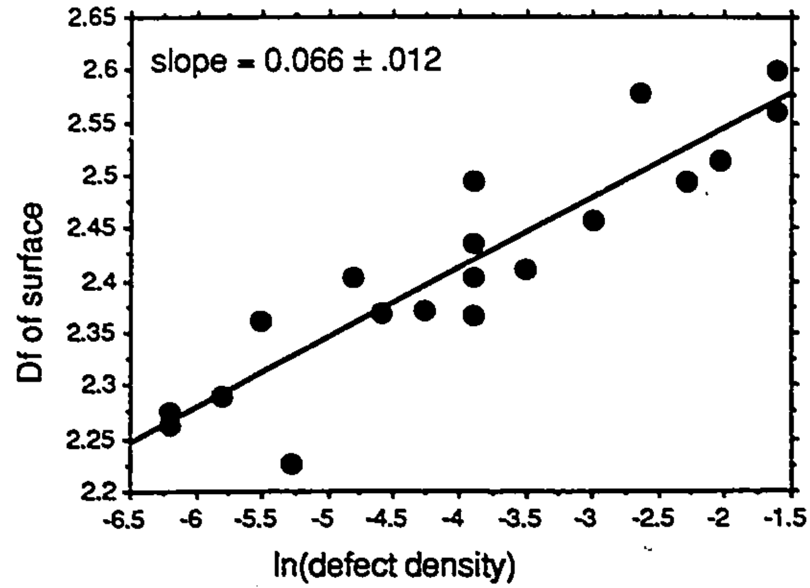

Fig. 5.15 Plot demonstrating a linear relationship between the fractal dimension of simulated joint surface vs. logarithm of defect density used during its generation.

This simulation of joint propagation under conditions of inclusion hackle suggests one way that microstructures (in this case defects) can influence the resulting joint surface morphology. In the next section, these simulation results are applied to the analysis of the natural plumose joint discussed in chapter 4.

5.6.1.2 Application to natural joint surfaces

For most brittle fractures in rock, the propagating fracture front is accompanied by a distribution of microcracks contained in a zone of inelastic deformation. The size of this "process zone" (see Fig. 2.2) has been estimated for joints in sandstone by measuring the zone of enhanced permeability adjacent to the fracture. Barton, (1983) used this method to estimate a process zone diameter of 1 mm for joints in Cardium Sandstone. This technique could not be used on the analyzed joint surface of Fig. 4.1 because of visible post-jointing weathering to a depth of about 0.5 mm. Therefore, the process zone for the analyzed joint has not been measured. However, a process zone size similar to that of other sandstone joints, (approximately 1 mm, Barton, 1983), does not seem unreasonable.

Assuming a process zone of approximately 1 mm diameter, the photomicrograph of Fig. 4.2 suggests that the main structural defects of the analyzed sample are the few quartz grains which are larger than 1 mm in diameter. For the sample, the defect density can be readily calculated from thin section. The area of the thin section is approximately 30 mm x 24 mm = 720 mm^2. There are approximately 20 grains > 1 mm in diameter. Therefore the defect density equals 20/720, or approximately 3%.

The computer simulation of the jointing process is tested by comparing the fractal dimension of the actual joint ($D_f = 2.24$) with the fractal dimension of a computer generated joint surface formed at a defect density of 3% ($D_f = 2.4$). This discrepancy may be caused by other factors which also affect the fractal dimension of the fracture surface, as discussed in the next section.

5.6.1.3 Varying D_f of fracture front

The nature of the propagating fracture front (i.e. whether it is smooth or irregular) can be altered by slightly changing the growth algorithm. The potential fracture sites, located adjacent to the fracture, have a pre-determined probability of becoming part of the jointed surface during any iteration. For example, say there are 8 potential sites. During one iteration, only 50% of these sites (i.e. 4 sites) actually become incorporated into the growing fracture because during the current (see Fig. 5.16).

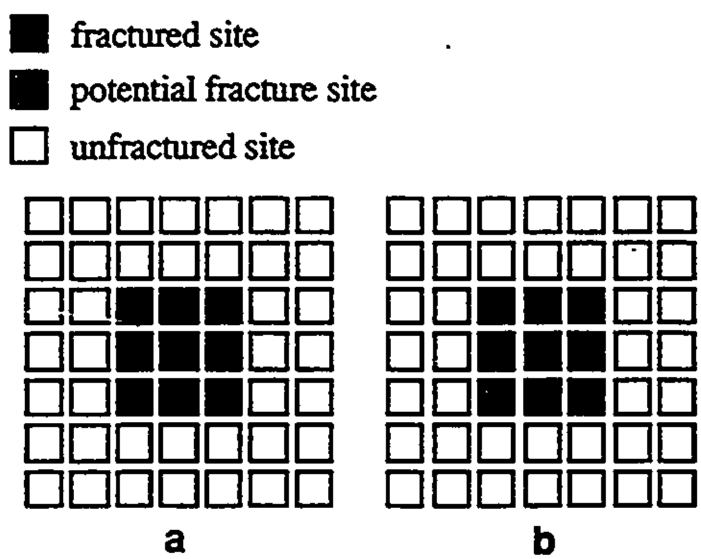

Fig. 5.16 a) Fractured site and the surrounding eight potential fracture sites. During the current iteration, each site has a probability, P=0.5, of becoming a fractured site.b) Original fracture site plus four new fracture sites randomly selected from the potential sites in (a).

By changing the probability that potential sites immediately become fractured sites, (i.e. the site potential), the nature of the propagating fracture front changes dramatically. For the present discussion, the nature of the fracture front refers its spatial variation within the plane of fracture. It does not include those variations perpendicular to the fracture, as induced by inclusion hackle. Fig. 5.17 illustrates how the fracture front varies with increasing site potential. For P=1, the probability of a potential site becoming a fractured site during a single iteration is 1.

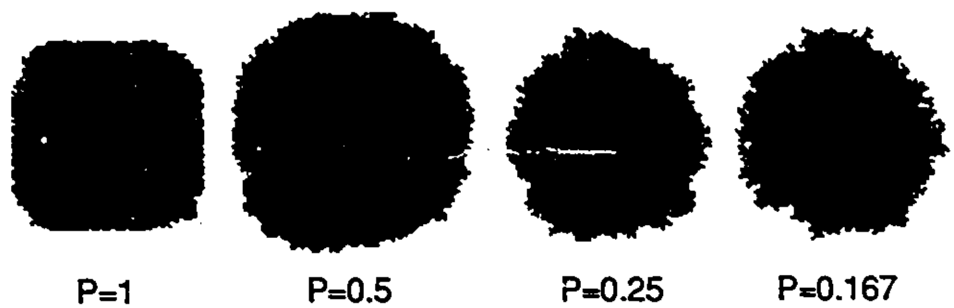

Fig. 5.17 Projections of computer generated joints formed with varying site potentials (P). Note that decreasing P results in rougher fracture fronts .

Notice that the fracture front formed at P=1 is almost straight, as is expected from growth on a lattice. With decreasing P, the fracture front becomes increasingly rough. Using the box method, the fractal dimension of the fracture fronts can be estimated. Fig. 5.18 shows a typical result from a box method analysis of a fracture front, in this case P=0.25. The fractal dimension of the fracture front is estimated at 1.30 ± .03 (95%).

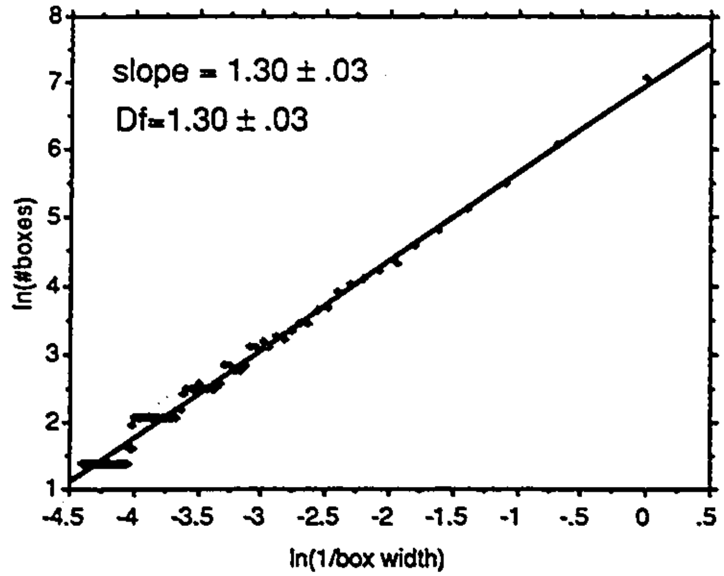

Fig. 5.18 Plot for box method analysis of fracture front formed at site potential P=0.25. Fractal dimension is estimated by the slope of the regression line through the data. D_f equals 1.30 ±.03 (95%).

The fractal dimension of the propagating fracture front affects the fractal dimension of the resulting joint surface. This is demonstrated in the plots of Fig. 5.19. In these plots, the surface D_f is plotted against the fracture front D_f measured during the simulation. This is done for simulation runs at defect densities of 3% and 10%. There is considerable scatter in the data because the differences in the measured surface D_f are close to the error limits of the slit island technique. However, a similar trend is observed in both runs. There is an initial decrease of surface D_f with increasing fracture front D_f. In both runs, the surface D_f reaches a minimum at a fracture front D_f of approximately 1.29. Subsequent increases in fracture front D_f result in increases of surface D_f, until a maximum is reached at fracture front D_f of approximately 1.34. In both runs, after this maximum, the surface D_f decreases with increasing fracture front D_f.

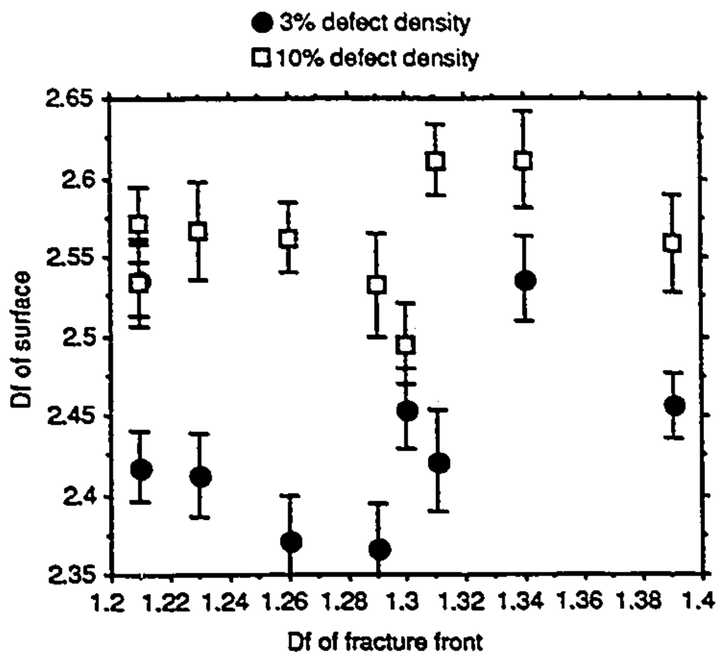

Fig. 5.19 Plot of fractal dimension of fracture surface vs. fractal dimension of propagating fracture front for defect densities of 3% and 10%. Error bars for surface D_f estimates are at 1σ. Errors in the fracture front D_f estimates are approximately .025 at 1σ. Both plots demonstrate an initial decrease of surface D_f with increasing fracture front D_f. Minimum surface D_f occurs at fracture front D_f of approximately 1.29. Subsequent increases in fracture front D_f results in increases of surface D_f, towards a maximum at fracture front D_f of approximately 1.34.

Again, a rigorous mathematical explanation for this trend is lacking. However, it is observed that very low D_f fracture fronts produce slit islands that tend to be extremely elongate in the radial direction (see Fig. 5.20a). This is in contrast to the more equi-dimensional islands (see Fig. 5.20b) observed for joint surfaces generated at higher fracture front D_f.

Fig. 5.20 a) Slit island section through simulated joint surface generated with 10% defect density and a fracture front D_f of approximately 1.2. Df of surface is approximately 2.5 . Note that islands are elongate in radial direction. b) Slit island section through simulated joint surface generated with 10% defects and a fracture front D_f of approximately 1.38. D_f of surface is approximately 2.5. Note that the islands are more equi-dimensional than in (a).

5.6.1.4 Application to natural joint surfaces

In the simulations, the fractal dimension of the propagating fracture front is an important control over the fractal dimension of the resulting joint surface. Is this also an important control for natural joints? This can only be answered by investigating the nature of fracture fronts in joints and fractures. Theoretically, Irwin (1962) determined for mode I loading that "if crack extension is governed by the stress intensity factor attaining its critical value, then the elliptical crack will have a tendency to grow into a circular one" (Kanninen and Popelar, 1985). This one example suggests a tendency for joints to "straighten out" any irregularities in the propagating fracture front. However, Kanninen and Popelar (1985) indicate that for mixed mode loading, "there is a lack of agreement on what the appropriate fracture criterion ought to be". Consequently, the theoretical nature of a fracture front in a propagating joint experiencing transient mixed-mode loading is unclear.

Practically, it is difficult to actually observe a propagating fracture front. Therefore, most studies rely on fractographic evidence to determine the shape of fracture fronts. Joint surface features which are thought to mark places where the joint has hesitated (possibly due to changes in principal stress directions) are known as conchoidal structures (Hodgson, 1961), annular structures (Bankwitz, 1965, 1966), rib marks (Dennis, 1972, arrest lines (Kulander *et al*, 1979), and hesitation lines (Barton, 1983). Certainly these names adequately describe the smooth rounded appearance of most hesitation features. However, it should be noted that these concentric features are thought to form when the joint has momentarily stopped. Certainly, the conditions causing hesitation are different from those operating during regular propagation. Work by Kulander *et al*, 1979, Barton, 1983, and Bahat and Engelder, 1984, demonstrates that plumose patterns and fracture fronts, can be quite irregular. This concurs with results from low velocity fracture experiments by (Kies, 1951) and with the idea proposed by Poncelet (1965) that all bonds along the front may not break simultaneously.

Therefore, in spite of the preponderance of rounded hesitation features, there does appear to be variability in the character of the propagating fracture front. As in the simulations, it is possible that the nature of the propagating fracture front affects the resulting joint surface. However, there has not been a quantitative study relating joint surface morphology to the character of the propagating fracture front.

Irregular fracture fronts described by Bahat and Engelder, (1984), are proposed to be slow-forming and pore-pressure controlled (Bahat and Engelder, 1984). For these joints, the evolving pore-pressure field surrounding the propagating joint surface may influence the growth dynamics. In fact, recent studies in physics have demonstrated that dissolution networks formed in other systems under similar pore-pressure fields are fractal (Daccord, 1987). Appendix A discusses these new ideas and relates them to fracture propagation and bifurcation.

5.7 Discussion

The results of the simulation demonstrate that the slit island method can be used to quantify subtle changes in the surface morphology of joints. The simulation also demonstrates that material properties, such as defect density, can affect the fractal characteristics of the joint surface. Furthermore, the fractal nature of the joint surface is also influenced by the growth dynamics, as illustrated by the fracture front experiments. Undoubtedly there are more parameters, both material and dynamic, that can affect the joint surface morphology. For example, DeGraff and Aydin (1987) argue that the loading configuration affects the symmetry of plumose patterns. Preliminary experiments with the simulator indicate that this also affects the fractal dimension of the resulting surface. Slight variations in the statistical properties of the defects, such as their size and spatial distributions, may also affect the joint surface morphology. However, the goal of this thesis is not to document every possible parameter and its potential affects. Rather, the intent is to demonstrate that surface patterns can be quantified, and correlated with the material properties of the rock and with elements of the fracture growth dynamics.

The slit island technique is one way of quantifying the fracture surface. Fig. 5.20 shows that surfaces having similar fractal dimensions can be quite different in appearance. Indeed, since the fractal dimension is estimated from the slope in log(perimeter)/log(area) space, there may exist a wide range of surfaces having the same slope and hence fractal dimension.

The simulation also illuminates one potential problem in using the slit island method for estimating D_f of fractal surfaces. The slit island method uses the fractal dimension of the island boundaries to estimate D_f of the surface. In some cases, D_f of island boundaries do not correspond with fractal surfaces equal to $D_f + 1$. In the simulation, the surfaces produced at low defect densities (<0.2%) are predominantly planar, with fractal boundaries separating the individual planar sections. Therefore, the fractal dimensions of the island boundaries do not correspond with the planar surfaces (i.e. $D_f = 2$) of the individual islands. Therefore, it appears that the slit island method is useful for determining the fractal dimension of the zeroset, which may or may not be related to the fractal dimension of surface, as suggested by Lung and Mu (1988). For this reason, it is important to state the method used in determining the fractal dimension of a surface.

CHAPTER 6
SHATTER CONES

6.1 Introduction

Shatter cones are conical fractures spatially associated with high energy events such as meteorite impact (Dietz, 1968, Dietz, 1972), large scale (100 ton TNT) chemical explosions (Roddy and Davis, 1977) and nuclear explosions (Dietz, 1960; Bunch and Quaide, 1968). Their precise origin is problematic (Milton, 1977). This is due in part to an incomplete understanding of the mechanics of shock wave propagation in rock. However, shatter cones share enough characteristics with plumose joints to warrant a similar surface analysis using fractal geometry.

6.2 Description

Fig. 6.1 shows a well-defined shatter cone in Ordivician limestone of the Eleanor River Formation (Thursteinsson and Mayr, 1987) from the Haughton impact structure, Devon Island, Canadian Arctic Archipelago (sample from the University of Ottawa collection). This shatter cone displays most of the diagnostic features of shatter cones (as compiled by Dietz 1968, 1972). A partial list of these features is given below.

a) Shatter cones are conical fracture surfaces with striae fanning outward from the apex in horsetail-like packets.

b) Small parasitic half-cones are shingled on the face of the master cone.

c) Shatter cones are best developed in aphanitic and dense rocks, especially carbonate. They are also found in shale, sandstone, quartzite, granite, gneiss and other lithologies.

d) Shatter cones range greatly in length, from 1 cm to >12 m.

e) Apical angles are reported to vary from approximately 60° to 120°, with the overall average near 90°.

f) An inhomogeneity, such as a clastic quartz grain in limestone, may be at the apex of the cone.

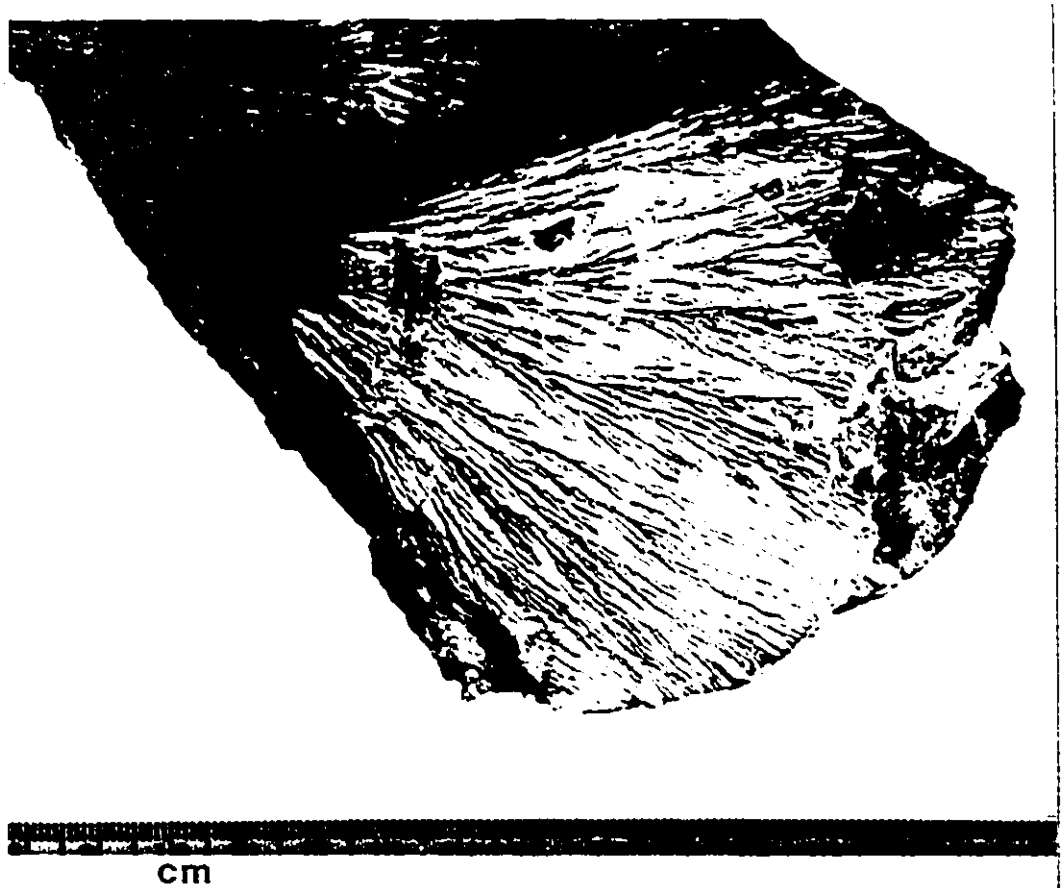

Fig. 6.1 Shatter cone in limestone from the Haughton impact structure, Devon Island, Canadian Arctic Archipelago

6.3 Fractal analysis of shatter cone surface

The fractal dimension of the shatter cone surface was measured using the slit island method (see section 3.8.1). In this case, the conical surface of the shatter cone mold was unfolded (when in malleable form). Such a non-infinite transformation does not affect fractal dimension (see for example Barnsley, 1988, pg. 179). A typical slit-island section from the shatter cone is seen in Fig. 6.2. The ln(perimeter)/ln(area) plot of Fig. 6.3

yields a slope of $0.62 \pm .046$, and therefore a fractal dimension of $2.24 \pm .09$.

Fig. 6.2 Typical slit island section from shatter cone surface in Fig. 6.1 .

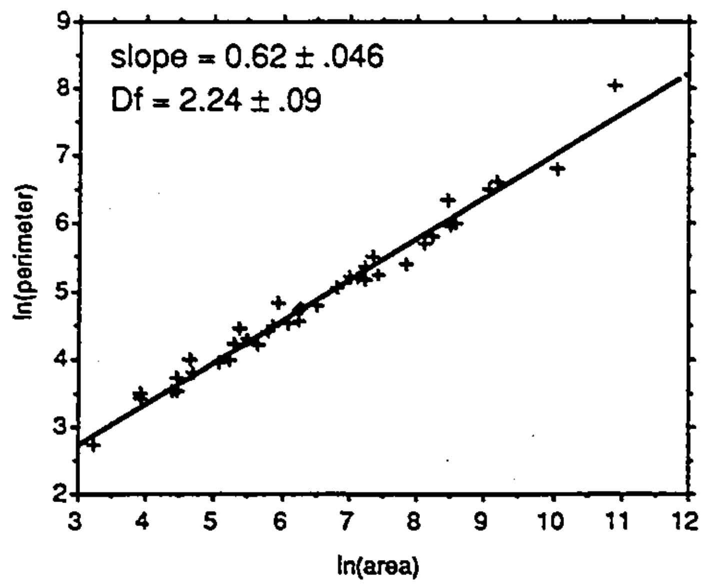

Fig. 6.3 Double logarithmic plot of perimeter vs. area for islands from slit island sections of shatter cone. Reduced major axis regression yields a best fit line of slope 0.62 ± .046. Therefore, the fractal dimension of surface equals approximately 2.24 ± .09.

6.4 Theory of formation

The formation of shatter cones has never been observed. Therefore, the theory of their formation is based on shatter cone morphology, and the study of shock mechanics. The most widely accepted theory was developed by Johnson and Talbot (1964). This theory is unfortunately unpublished, and as Milton (1977) suggests, it "has received little scrutiny".

The theory is based on the observation (from underground nuclear tests) that strong compression wavefronts are multiple fronts (for example see Melosh, 1989), in that they are composed of an elastic precursor wave traveling in advance of a slower-moving "plastic" wave (see Fig. 6.4).

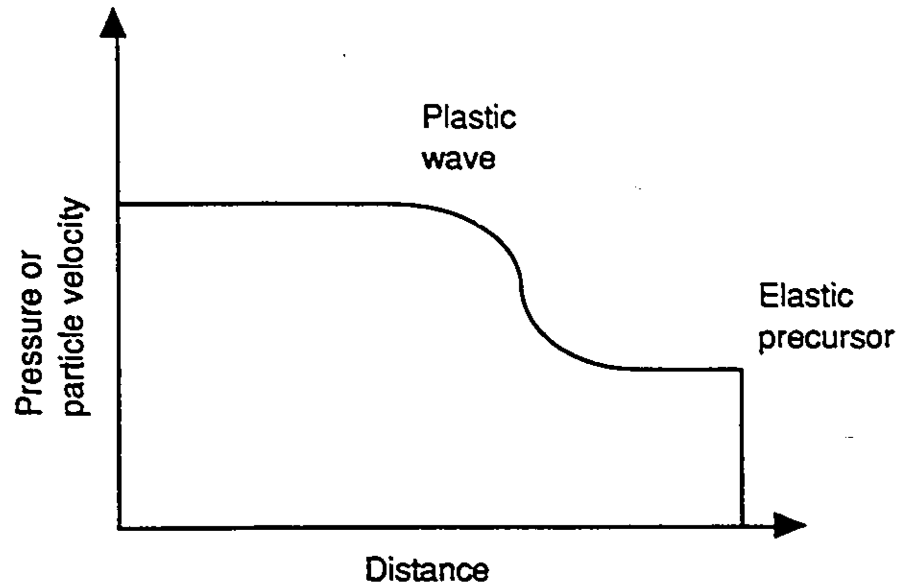

Fig. 6.4 Structure of a strong compression wavefront. A lower pressure fast-moving elastic wave is precursor to the stronger slow-moving plastic wave. (From Melosh, 1989).

Johnson and Talbot suggest that shatter cones are nucleated when the elastic precursor wave encounters a small region of anomalous density or compressibility (i.e. a defect). This generates a secondary stress wave which propagates spherically outward. This secondary wave and the elastic precursor wave interact constructively to yield stresses exceeding the elastic limit of the rock. As the two waves propagate outwardly, the region contained within the conical intersection is plastically deformed, whereas the rock outside this volume is only elastically deformed. Therefore, after the passage of the elastic precursor, the material outside of the cone returns to its original state and is separated from the permanently deformed material by a conical fracture (see Fig. 6.5).

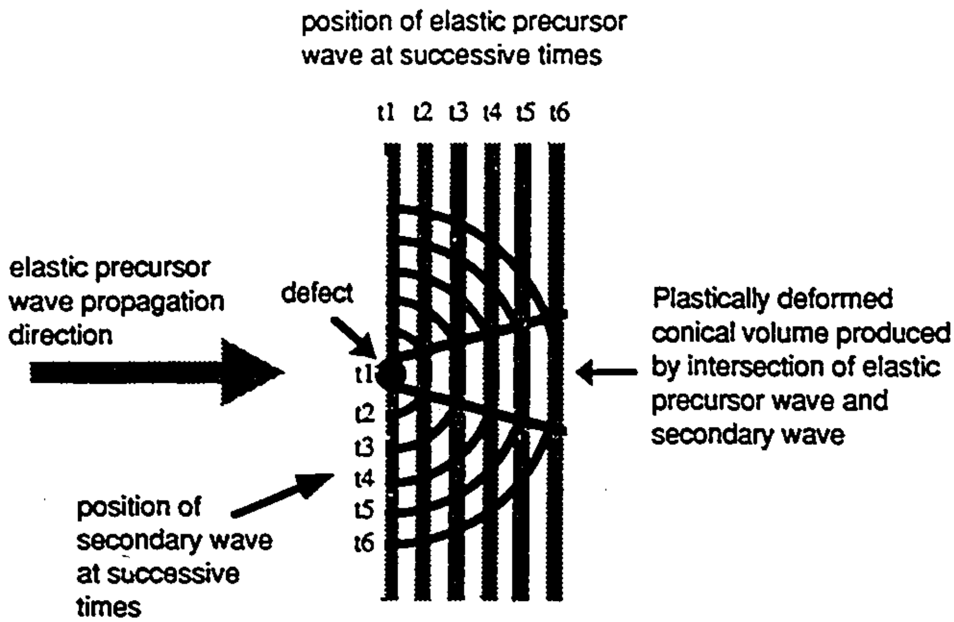

Fig. 6.5 Cross-sectional sketch of hypothetical shatter cone model as proposed by Johnson and Talbot (1964). Propagating elastic precursor wave (grey lines) intersects defect, nucleating a secondary stress wave (black semi-circles). The 2 waves constructively intersect and over time sweep out a conical volume that has been stressed beyond the elastic limit. The shatter cone fracture surface separates this plastically deformed volume from the elastically deformed surrounding rock.

The Johnson-Talbot model accounts for the overall conical nature of the fracture surface. Furthermore, the striations on the cone surface are thought to be caused by the plastic domain moving relative to the elastic domain. However, the Johnson-Talbot model does not explain the ever present nested cones, i.e. scale-invariant coning, which form the fracture surface. As suggested by Dietz (1968,1972) and Milton (1977), the Johnson-Talbot model requires much more study. The following discussion offers a few new ideas pertaining to the origin of shatter cones.

6.5 New observations and discussion

There are several similarities between shatter cones and plumose joints. Both fracture types are nucleated at structural defects and both are best observed in hand samples of fine-grained homogeneous rocks. Furthermore, both fracture types have radiating surface features.

According to Dietz (1968, 1972), "shatter cones are conical fracture surfaces with striae which fan outward from the apex in horsetail-like packets". Furthermore, "the striae are sharp grooves between intervening, rounded ridges - or the reverse on negative mold faces", and "small parasitic half-cones are shingled on the face of the master cone". These striae and parasitic half-cones are re-examined for the spectacular shatter cone sample of Fig. 6.1.

In this shatter cone, if a piece of the fracture surface is separated from the rest of the surface, then the newly-exposed sub-surface is also striated (see Fig. 6.6). In fact, when whole half-cones are removed, the newly-exposed sub-surface is striated in a manner visually similar to the rest of the fracture surface. Therefore, there appears to be an overlapping set of striated, convex fracture surfaces within the conical volume enveloping the shatter cone surface. For this sample, these penetrative shingled fracture surfaces are generally < 1 mm apart. Furthermore, these surfaces intersect, and they are all convex in the same direction. Dietz may have been referring to this phenomena when he noted that "shatter cones which formed last, i.e. millimeters to centimeters farther from the shock wave source, truncate earlier shatter cones producing a stacked appearance on a thoroughly shatter-coned rock" (Dietz, 1968, 1972).

Fig. 6.6 Photograph demonstrating penetrative striated fracture surfaces. Note the lower striated fracture surface exposed by the late fracture across the shatter cone. Width of photo approximately 4 cm.

The very fine-grained nature of the rock containing the shatter cone sample facilitates a detailed examination of the striations on the fracture surface. Here, the striations appear as high angle intersections (i.e. intersection lineations) between adjacent planar elements of the convex fracture surface (see Fig. 6.7). Furthermore, all of these small planar fracture elements (<1mm wide) have long axes which are radial to the conical axis. Therefore, it is possible that each of these minute planar fracture elements is an independent, radially-extending microfracture. Furthermore, these radiating microfractures intersect forming the convex fracture surfaces described above. Therefore, what kind of fracture dynamics are required to produce a shingled set of convex fracture surfaces that are defined by a set of intersecting, radially-extending microfractures?

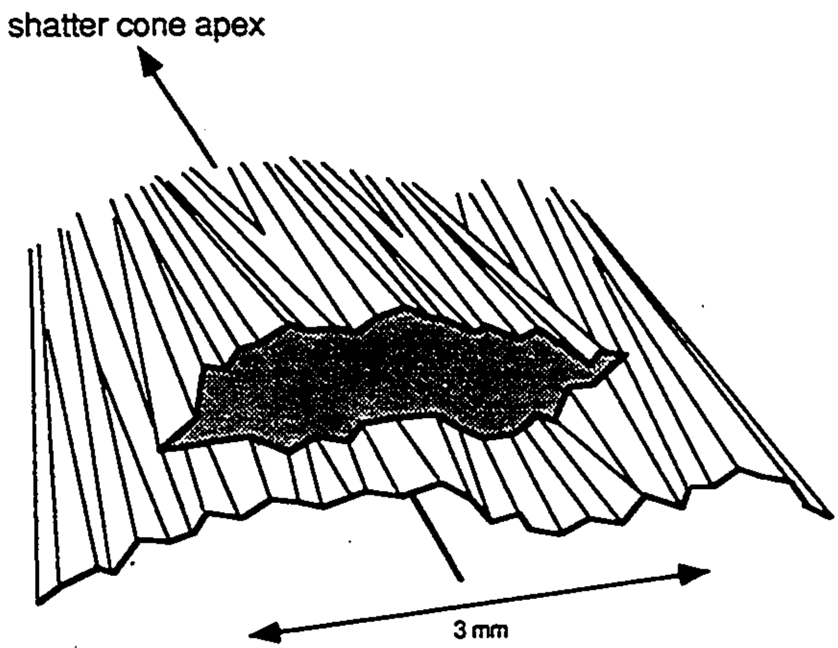

Fig. 6.7 Sketch of shatter cone surface interpretation. Note that radial striations are intersections between radially-extending planar microfractures. Furthermore, the larger convex fracture surfaces are defined by the intersection of these microfractures.

First, consider the geometry of the Johnson-Talbot model (see Fig. 6.5). At some time, t_1, the interior region of the cone is plastically deformed, and radial tension develops in the ring-like volume separating the plastic and elastic domains (see Fig. 6.8). It is proposed that many microfractures instantly form in response to the tension. These multiple microfractures, (as opposed to a single fracture) are consistent with the Johnson-Talbot hypothesis. Under loading conditions controlled by hyper-velocity stress waves, there is not time for the earlier-formed fractures to unload stress. Therefore, numerous microfractures are expected. Most of these microfractures are oriented approximately perpendicular to the radial tension. However, any inherent planar weakness in the material, such as grain boundaries or cleavage, could cause microfractures to form at an oblique angle to the radial tension (see Fig. 6.8).

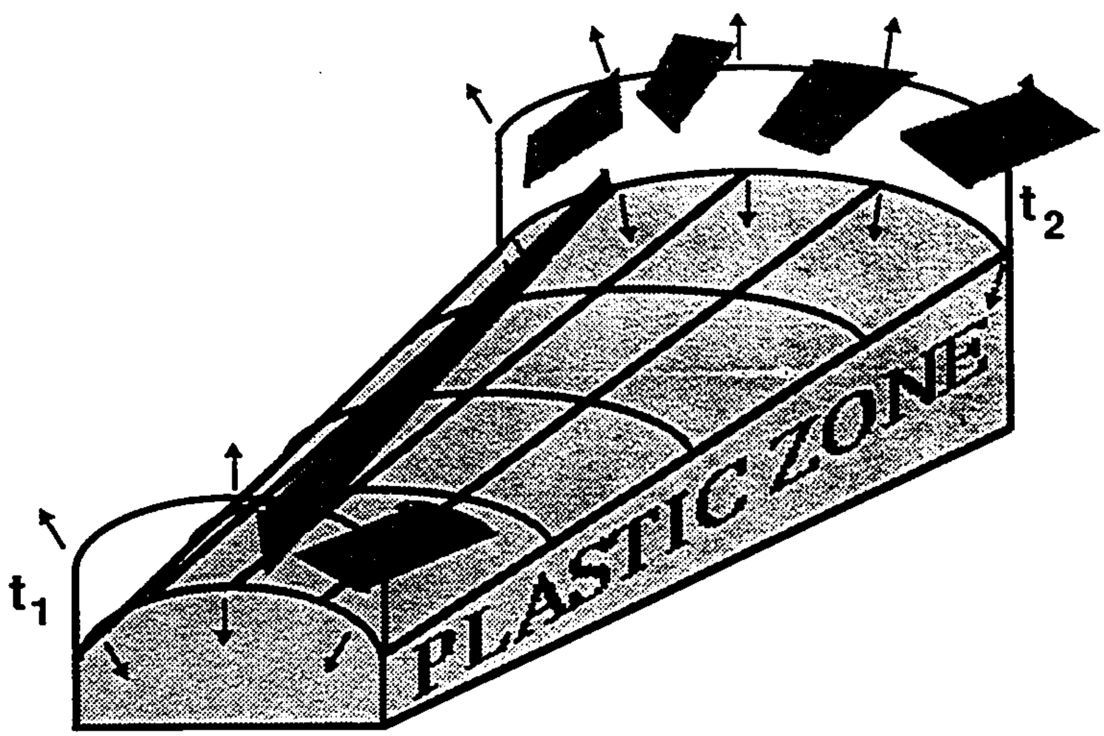

Fig 6.8 Schematic diagram of hypothetical shatter coning process. At some time t_1, numerous microfractures form along the plastic/elastic interface in response to radial tension (indicated by the arrows). These microfractures propagate some distance under inertial effects. Some fractures (A) intersect the expanding plastic zone and are stopped. Other fractures (B) extend for some time before stopping. At some later time, t_2, more fractures are nucleated and the process continues. See text for full explanation.

At some later time, t_2, (see Fig. 6.8), the zone of plastic deformation expands, and new microfractures are again nucleated along the plastic/elastic boundary. What has happened to the microfractures formed at t_1? The radiating striations on the surface of the shatter cone in Figs. 6.1 and 6.6, if they are fracture edges, indicate that some of these microfractures must have continued to propagate in their original plane of fracture. This presents a problem. Given hyper-velocity conditions, (i.e. fracture rates exceeding the velocity of a stress-wave) an existing fracture does not have time enough to concentrate stresses. Therefore, there are no stress-related reasons for a microfracture plane to extend itself. However, it is possible that the inertial effects of the hyper-velocity fracture front are strong enough to cause limited extension of existing microfractures. At t_2, the ring of greatest tension has expanded and some of the fractures formed at t_1, including those perpendicular to the radial tension, have propagated directly into the zone of plastic deformation where they are presumably arrested (see Fig. 6.8). Alternatively, once stress is removed, fractures decelerate very rapidly (see for example Dally, 1979). Therefore, some fractures may extend slightly and then simply stop.

The dynamics described above would create a conical envelope that contains many radially-extending microfractures. This is consistent with the observations noted above. However, it is not clear how these microfractures coalesce to form the penetrative convex conical fracture surfaces. Again, hyper-velocity conditions do not allow time for stress concentration around pre-existing fractures. Therefore, there are no stress-related reasons for the many adjacent microfractures to propagate as a single complex fracture surface. Again, one possible reason for the grouping of microfractures is the vector nature of the hyper-velocity fracture front inertia. This would imply that many new microfractures are created at the same time, along a curved front. This is not unreasonable given that new ring-like volumes of rock are simultaneously exposed to the radial tension. The microfractures along these fronts are accelerated to hyper-velocities, and the acquired inertia keeps the front moving in a constant direction, for some short period of time. What are the consequences of this hypothetical process? Fig. 6.9 demonstrates that if the fracture fronts continue to propagate vectorially (under inertial effects), they would eventually propagate into the plastic domain where they are presumably arrested. However, other fracture fronts are formed in the new tensional regions. This would lead to the continuous production of new convex fracture surfaces, which would be shingled on top of earlier fractures (see Fig. 6.9). This is consistent with the observations mentioned above. Furthermore, the imperfect spacing of the convex fracture surfaces implies that there is a random factor affecting the fracture process. Undoubtedly, the propagating hyper-velocity stress waves are not perfect, hence some variation in tension direction is expected. Furthermore, the abundant defects in rock affect the initiation of microfractures, and hence the propagation of the convex fracture fronts.

Eventually the actual shatter cone observed in outcrop is formed. This fracture surface is not a loose collection of conical fragments. Rather, the surface is intact. Therefore something has caused the conical fracture zone to be somewhat re-constituted. Fig. 6.4 illustrates one possible mechanism for this. If shattering occurs in response to the precursor elastic wave, then a few micro-seconds later the entire volume of rock is plastically deformed in response to the higher energy compression wave which immediately follows the precursor elastic wave. The actions of this pressure wave, and the corresponding increase in heat (see for example Melosh, 1989), might be sufficient to re-constitute the fragmented rock. Therefore, in the fraction of a second that the rock is exposed to the shock wave, it changes from the original rock into a highly-fractured equivalent, and then back into a re-constituted rock. Fig. 6.6 demonstrates that all could hypothetically happen without a great deal of mixing, since fossil outlines and quartz veins preserve their original shape and orientation.

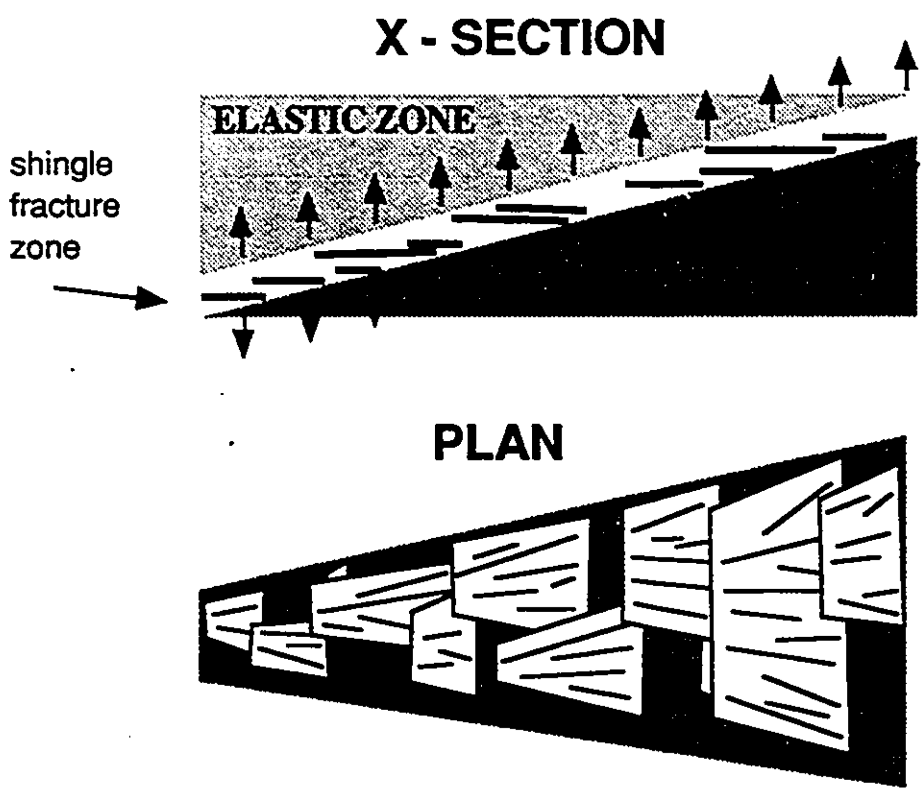

Fig. 6.9 Schematic X-section and plan view of shingled fracture zone formation. Radial tension (represented by arrows in x-section) causes fracture fronts to nucleate. Fracture front accelerates and propagates for some time under inertial effects. In some cases, front may be arrested at plastic zone. As the tensional and plastic zones expands, additional convex fractures are shingled atop of earlier ones. See text for full description.

As observed in the sample of Fig. 6.1, there are many possible final shapes to the shatter cone surface. Most shatter cones demonstrate a hierarchy of cone-sizes. In the above scenario, the final shape depends on how the fracture is eventually re-opened. This might occur during unloading of the compression wave, or long after the shock wave has passed. In either case, it is likely that the inherent weakness of the shingled fracture surfaces controls the final fracture opening, and thus the fractal nature of the outer shatter cone surface.

CHAPTER 7
SUMMARY AND CONCLUSIONS

Using the slit island technique, the fractal dimension of a self-affine plumose joint surface is estimated at 2.24. Surfaces of similar fractal dimension and appearance are produced by a 3D computer simulation of slow joint propagation in rock. In the simulator, randomly-distributed defects cause the propagating fracture front to be locally mis-oriented. Away from defects, the simulated fracture propagates perpendicular to remote tension. This process results in planar radial fracture segments (i.e. inclusion hackle) that collectively form the plumose pattern. For the simulation results, there is a linear relationship between the fractal dimension of the joint surface and the log of the defect density. Furthermore, the simulation shows a complex relationship between the fractal dimension of the propagating fracture front and the resulting fractal dimension of the joint surface.

Using a variation of the slit island technique, the fractal dimension of a shatter cone surface is estimated at 2.24. Multiple convex fracture surfaces, each radially-striated, are observed in the rock volume surrounding a shatter cone surface in fine-grained limestone. The striations are interpreted by the author as microfracture intersections which form when a hyper-velocity fracture front sweeps through the conical envelope at the elastic/plastic boundary (as proposed by Johnson and Talbot, 1964). The shingled appearance of the multiple convex fracture set is proposed to be due to the continuous nucleation of new fracture fronts along the expanding zone of radial tension. The inertia of these hyper-velocity fracture fronts is proposed to cause them to propagate vectorially. The fronts are proposed to eventually stop, either by extending into the expanding plastic zone, or by rapid deceleration after removal of tensional stress. These geometric features are consistent with the shatter cone model proposed by Johnson and Talbot (1964).

REFERENCES

Atkinson, B.K., 1987, Introduction to fracture mechanics and its geophysical applications, *in* Atkinson, B.K., ed., Fracture mechanics of rocks: Academic Press, London, England, p. 1-26.

Atkinson, B.K., and Meredith, P.G., 1987, The theory of subcritical crack growth with applications to minerals and rocks, *in* Atkinson, B.K., ed., Fracture mechanics of rock: London, England, Academic Press, p. 111-166.

Aviles, C.A., Scholz, C.H. and Boatwright J., 1987, Fractal analysis applied to characteristic segments of the San Andreas Fault: Journal of Geophysical Research, v. 92, p. 331-344.

Aydin, A., 1978, Small faults formed as deformation bands in sandstone: Pure and Applied Geophysics, v. 116, p. 913-930.

Bahat, D., and Engelder, T., 1984, Surface morphology on cross-fold joints of the Appalachian Plateau, New York and Pennsylvania: Tectonophysics, v. 104, p. 299-313.

Balk, R., 1937, Structural behavior of igneous rocks: Geological Society of America Memoir 5, 177 p.

Bankwitz, P., 1965, Uber klufte I. Beobachtungen im Thuringischen Schiefergebirge: Geologie, v. 14, p. 241-243.

Bankwitz, P., 1966, Uber klufte II. Die bildung der kluftlache und eine systematik ihrer strukturen: Geologie, v. 15, p. 896-941.

Barnsley, M.F., 1988, Fractals everywhere: Academic Press Inc., San Diego, U.S.A., 397 p.

Barton, C.C., 1983, Systematic jointing in the Cardium Sandstone along the Bow River, Alberta, Canada (Ph.D. Thesis): New Haven, Connecticut, Yale University, 301 p.

Becker, G.F., 1891, The structure of a portion of the Sierra Nevada of California: Geological Society of America Bulletin, v. 2, p. 49-74.

Becker, G.F., 1893, Finite homogeneous strain, flow and rupture of rocks: Geological Society of America Bulletin, v. 4, p. 13-90.

Becker, G.F., 1895, The torsional theory of joints: American Institute of Mining Engineering Transactions, v. 24, p. 130-138.

Bieniawski, Z.T., 1967, Mechanism of brittle fracture of rock, part I and part II: Int. J. Rock Mech. Min. Sci. , v. 4, p. 395-423.

Borg, I.Y., and Maxwell, J.C., 1956, Interpretation of fabrics of experimentally deformed sands: American Journal of Science, v. 254, p. 71-81.

Bouchaud, E., Lapasset, G., and Planes, J., 1990, Fractal dimension of fractured surfaces: a universal value?: Europhysics Lett. 13 (1), p.73-79.

Brace, W.F., and Bombolakis, E.G., 1963, A note on brittle crack growth in compression: Journal of Geophysical Research, v. 68, p. 3709-3712.

Bronowski, J., 1973, The ascent of man: British Broadcasting Corporation, London, U.K., 287 p.

Brown, S.R., and Scholz, C.H., 1985, Broad bandwidth study of the topography of natural rock surfaces: Journal of Geophysical Research, v.90, p.12575-12582.

Bucher, W.H., 1920, The mechanical interpretation of joints, Part I: Journal of Geology, v. 28, p. 707-730.

Bucher, W.H., 1921, The mechanical interpretation of joints, Part II: Journal of Geology, v. 29, p. 1-28.

Bunch, T.E., and Quaide, W.L., 1968, Shatter cones in the Danny Boy nuclear crater, *in* French, B.M., and Short, N.M., eds., Shock metamorphism of natural materials: Mono Book Corp., Baltimore.

Chermant, J.L. and Coster, M., 1979, Review quantitative fractography: Journal of Materials Science 14, p. 509-534.

Coster, M., and Chermant, J.L., 1983, Recent developments in quantitative fractography: International Metals Reviews, v.28, p.228.

Crosby, W.O., 1882, On the classification and origin of jointed structures: Proceedings of the Boston Society of Natural History, v. 22, p. 72-85.

Daccord, G., 1987, Chemical dissolution of a porous medium by a reactive fluid: Physics Review Letters, v. 58, p. 479-482.

Daccord, G., Nittman, J., and Stanley, H.E., 1986, Radial viscous fingers and diffusion-limited aggregation: fractal dimension and growth sites: Physics Review Letters, v. 56, p. 336-339.

Dauskardt, R.H., Haubensak, F., and Ritchie, R.O., 1990, On the interpretation of the fractal character of fracture surfaces: Acta metall. mater., v.38, p.143-159.

Dally, J.W., 1979, Dynamic photoelastic studies of fracture, Experimental Mechanics, v. 19, p. 349-361.

Davy, Ph., Sornette, A., and Sornette, D.,1990, Some consequences of a proposed fractal nature of continental faulting: Nature, v. 348, p.56-58.

DeGraff, J.M. and Aydin, A., 1987, Surface morphology of columnar joints and its significance to mechanics and directions of joint growth: Geological Society of America Bulletin, v.99, p.605-617.

Dennis, J.G., 1972, Structural geology: New York, Ronald Press, New York, 532 p.

Dietz, R.S., 1960, Meteorite impact suggested by shatter cones in rock: Science, 131, p. 1781.

Dietz, R.S., 1968, Shatter cones in cryptoexplosion structures, *in* French, B.M., and Short, N.M., eds., Shock metamorphism of natural materials: p. 267-285, Mono Book Corp., Baltimore.

Dietz, R.S., 1972, Shatter cones (shock fractures) in astroblemes, International Geological Congress, 24 th. session, sect. 15, p. 112-118.

Engelder, T., 1982, Reply to 'Is there a genetic relationship between selected regional joints and contemporary stress within the lithosphere of North America?': Tectonics, v. 1, p. 465-470.

Fowler, A.D., Stanley, H.E., and Daccord, G., 1989, Disequilibrium silicate mineral textures: fractal and non-fractal features: Nature, v. 341, p. 134-138.

Fowler, A.D., and Roach, D.E., 1991, Dimensionality analysis of objects and series data, *in* G.V. Middleton, ed., Non-linear dynamics, chaos and fractals with applications to geological systems: Geol. Assoc. Can. Short Course notes, v.9, p. 59-81.

Frechette, V.D., 1972, The fractology of glass, in Pye, L., *et al* eds., Introduction to glass science: Plenum Press, p. 432-450.

Freund, L.B., 1976, Dynamic crack propagation, *in* Redogan, F., ed., The mechanics of fracture: 19, ASME, p. 105-134.

Freund, L.B., 1978, The mechanics of dynamic shear crack propagation: Journal of Geophysical Research, v. 84, p. 2199-2209.

Freund, L.B., 1990, Dynamic fracture mechanics: Cambridge University Press, Cambridge, England, 563 p.

Gallagher, J.J., Friedman, M., Handin, J., and Sowers, G.M., 1974, Experimental studies relating to microfractures in sandstone: Tectonophysics, v. 21, p. 203-247.

Gell, M., and Smith, E., 1967, The propagation of cracks through grain boundaries in polycrystalline 3% silicon-iron: Acta Metallurgica, v. 15, p. 253-258,

Gilbert, G.K., 1882a, Post-glacial joints: American Journal of Science, v. 123, p. 25-27.

Gilbert, G.K., 1882b, On the origin of jointed structure: American Journal of Science, v. 124, p. 50-53.

Gilbert, G.K., 1884, On the origin of jointed structure: American Journal of Science, v. 127, p. 47-49.

Griffith, A.A., 1921, The phenomena of rupture and flow in solids: Royal Society of London Transactions, v. 2221, p. 163-198.

Guyon, E., and Stanley, H.E (eds.), 1991, Fractal forms, Elsevier Science Publishers B.V. and Palais de la Decouverte, Haarlem, The Netherlands, 50 p.

Hancock, P.L., 1985, Brittle microtectonics: Principles and practice: Journal of Structural Geology, v. 7, p. 437-457.

Hartmann, L., 1896, Distribution des deformations dans les metaux soumis a des efforts: Paris, France, Berger-Levrault.

Hodgson, R.A., 1961, Classification of structures on jointed surfaces: American Journal of Science, v. 259, p. 493-502.

Hoek, E., and Bieniawaski, Z.T., 1965, Brittle fracture propagation in rock under compression: International Journal of Fracture Mechanics, v. 1, p. 137-155.

Hopkins, W., 1835, Researches in physical geology: Transactions of the Cambridge Philosophical Society, v. 9, p. 1-84.

Hopkins, W., 1841, On the geological structure of the Weldon District and of the Bas Boullonais: Geological Society of London Transactions, 2nd. ser, v. 12, p. 1-51.

Hoskins, L.M., 1896, Flow and fracture of rocks as related to structure, *in* Van Hise, C.R., Principles of North American Pre-Cambrian geology: U.S. Geological Survey 16th Annual Report, p. 845-879.

Inglis, C.E., 1913, Stresses in a plate due to the presence of cracks and sharp corners: Royal Institute of Naval Architects Transactions, v. 55, p. 219-230.

Ingrafea, A.R., 1981, Mixed-mode fracture initiation in Indiana limestone and Westerly granite: U.S. Symposium on Rock Mechanics, 22nd. Proceedings, p. 186-191.

Irwin, G.R., 1957, Analysis of stresses and strains near the end of a crack traversing a plate: Journal of Applied Mechanics, v. 224, p. 361-364.

Irwin, G.R., 1958, Fracture, in Flugge, S., ed., Encyclopedia of physics: Berlin, Springer-Verlag, p. 551-590.

Irwin, G.R., 1960, Fracture mechanics, in Goodier and Hoff, eds., Structural mechanics: Pergammon Press, New York, p. 557-592.

Irwin, G.C., 1962, Crack-extension force for a part-through crack in a plate: Journal of Applied Mechanics, 29, p. 651-654.

Jaeger, J.C., and Cook, N.G.W., 1969, Fundamentals of rock mechanics: London, England, Metheun and Co., 513 p.

Johnson, J.W., & Holloway, D.G., 1966, Shape and size of the fractured zones on glass fracture surfaces: Philosophical Magazine, 14, p. 731.

Johnson, G.P., and Talbot, R.J., 1964, A theoretical study of the shock wave origin of shatter cones, Air Force Inst. Tech., M.S. thesis: Wright-Patterson AFB, Ohio, GSF/Mech 64-35, 92 p.

Kanninen, M.F., and Popelar, C.H., 1985, Advanced fracture mechanics: New York, Oxford University Press, 563 p.

Kies, J.A., Sullivan, A.M., and Irwin, G.R., 1950, Interpretation of Fracture Markings: Journal of Applied Physics, v. 21, p. 716-721.

King, W., 1875, Report on the superinduced divisional structure of rocks, called jointing; and its relation to slaty cleavage: Royal Irish Academy Transactions, v. 25, p. 605-662.

Kulander, B.R., Barton, C.C., and Dean S.L., 1979, The application of fractography to core and outcrop fracture investigations: Morgantown Energy Technology Center, METC/SP-79/3, 174 p.

Kulander, B.R., and Dean, S.L., 1985, Hackle plume geometry and joint property dynamics, *in* International Symposium on Fundamentals of Rock Joints, Proceedings, p. 85-94.

Lachenbruch, A.H., 1961, Depths and spacing of tension cracks: Journal of Geophysical Research, v. 66, p. 44273-4292.

Lachenbruch, A.H., 1962, Mechanics of thermal contraction cracks and ice-wedge polygons in permafrost: Geological Society of America Special Paper 70, 69 p.

Lawn, B.R., and Wilshaw, T.R., 1975, Fracture of brittle solids: Cambridge University Press, Cambridge, England, 204 p.

LeConte, J., 1882, Origin of jointed structure in undisturbed clay and marl deposits: American Journal of Science, v. 123, p. 233-234.

Liberty, B.A., 1971, Paleozoic geology of Wolfe Island, Bath, Sydenham, and Gananoque map-areas, Ontario: Geological Survey of Canada Paper 70-35, 12p.

Lockner, D.A., Byerlee, J.D., Kuksenko, V., Ponomarev, A., and Sidorin, A., 1991, Quasi-static fault growth and shear fracture energy in granite: Nature, v. 350, p. 39-42.

Long, Q.Y., Suqin, L., and Lung, C.W., 1991, Studies on the fractal dimension of a fracture surface formed by slow stable crack propagation: J. Phys. D: Appl. Phys. 24, p.602-607.

Louis, E., and Guinea, F., 1987, The fractal nature of fracture: Europhysics Letters, 3(8), p. 871-877.

Louis, E., Guinea, F., and Flores, F., 1985, The fractal nature of fracture, *in* Pietronero, L., and Tosatti, E., eds., Fractals in Physics: North Holland, Amsterdam, p. 177-180.

Lung, C.W. and Mu, Z.Q., 1988, Fractal dimension measured with perimeter-area relation and toughness of materials: Phys. Rev. B, v.38, p.781-789.

Lutton, R.J., 1969, Systematic mapping of fracture morphology: Geological Society of America Bulletin, v. 80, p. 2062-2065.

Maloy, K.J., Feder, J. and Jossang, T., 1985, Viscous fingering fractals in porous media: Physics Review Letters, v. 55, p. 2688-2691.

Mandelbrot, B.B., and van Ness, J.W., 1968, Fractional Brownian motion, fractional noises and applications: SIAM Review, 10, 4, p. 422-437.

Mandelbrot, B.B., 1975, Les Objet Fractals:Forme, Hasard, et Dimension: Paris, France, Flammarion.

Mandelbrot, B.B., 1982, The fractal geometry of nature: W.H. Freeman and Co., New York, 460 p.

Mandelbrot, B.B., Passoja, D.E., and Paullay, A.J., 1984, Fractal character of fracture surfaces of metals: Nature, v. 308, p. 721-722.

McGarr, A.M., and Gay, N.C., 1978, State of stress in the earth's crust: Annual Reviews of Earth and Planetary Science, v. 6, p. 401-436.

McGarr, A.M., 1982, Analysis of stress between provinces of constant stress: Journal of Geophysical Research, v. 87, p. 9279-9288.

McGee, W.J., 1883, Note on jointed structure: American Journal of Science, v. 125, p. 152-153.

Meakin, P., and Fowler, A.D., (in press), Diffussion-limited aggregation in the Earth Sciences, *in* CC. Barton, P. Lapointe, eds., Fractals in Petroleum Geology: A.A.P.G., special volume.

Meakin, P., Ball, R.C., Ramanlal, P., and Sander, L.M., 1987, Structure of large two-dimensional square-lattice diffusion-limited aggregates:Approach to Asymptotic Behavior: Phys. Rev. A35, p. 5233-5239.

Melosh, H.J., 1989, Impact cratering: a geological process: Oxford University Press, Inc., New York, U.S.A., 245 p.

Michalske, T.A., Singh, M., and Frechette, D., 1981, Experimental observations of crack velocity and crack front shape effects in double-torsion fracture mechanics tests: *in* Freiman, S.W., and Fuller, E.R., eds., Fracture mechanics methods for ceramics, rocks, and concrete: ASTM STP 745, American Society for Testing and Materials, p. 3-12.

Meisel, L.V., 1991, Perimeter-area analysis, the slit-island method and the fractal characterization of metallic fracture surfaces: J. Phys. D: Appl. Phys. 24, p. 942-952.

Milton, D.J., 1977, Shatter cones - An outstanding problem in shock mechanics; *in* Roddy, D.J., Pepin, R.O., and Merrill, R.B., eds., Impact and Explosion Cratering: Pergammon Press, New York, p. 703-714.

Mohr, O., 1900, Welche Umstande bedingen die elastizitatsgrenze und den bruch eines materials: Zeitschrift des Vereines Deutscher Ingenieure, v. 44, p. 1524.

Mu, Z.Q. and Lung, C.W., 1988, Studies on the fractal dimension and fracture toughness of steel: J. Phys. D: App. Phys. 21, p. 848-850.

Muehlberger, 1961, Conjugate joint sets of small dihedral angle: Journal of Geology, v. 69, p. 211-218.

Nemat-Nasser, S., and Horii, H., 1982, Compression-induced nonplanar crack extension with application to splitting, exfoliation, and rockburst: Journal of Geophysical Research, v. 87, p. 6805-6821.

Nickelsen, R.P., and Hough, V.N.D., 1967, Jointing in the Appalachian Plateau of Pennsylvania: Geological Society of America Bulletin, v. 78, p. 609-629.

Nickelsen, R.P., and Hough, V.N.D., 1969, Jointing in the south central New York:Reply: Geological Society of America Bulletin, v. 80, p. 923-926.

Niemeyer, L., Pietronero, L., and Wiesmann, H.J., 1984, Fractal dimension of dielectric breakdown: Physics Review Letters, v. 52, p. 1033.

Nittmann, J. and Stanley, H.E., 1986, Tip splitting without interfacial tension and dendritic growth patterns arising from molecular anisotropy: Nature, v. 321, p. 663.

Nittmann, J., Daccord, G. and Stanley, H.E., 1985, Fractal growth of viscous fingers: quantitative characterization of a fluid instability phenomenon: Nature, v. 314, p. 141-144.

Okubu, P.G., and Aki, K., 1987, Fractal geometry in the San Andreas fault system: Journal of Geophysical Research, v. 92, p. 345-355.

Pande, C.S., Richards, L.E., Louat, N., Dempsey, B.D., and Schwoeble, A.J., 1987, Fractal characterization of fractured surfaces: Acta metall. v.35, p.1633-1637.

Parker, J.M., 1942, Regional systematic jointing in slightly deformed sedimentary rocks: Geological Society of America Bulletin, v. 53, p. 381-408.

Parker, J.M., 1969, Jointing in south-central New York: Discussion: Geological Society of America Bulletin, v.80, p.19-22.

Pollard D.D., and Segall, P., 1987, Theoretical displacements and stresses near fractures in rock, with applications of faults, joints, veins, dikes, and solution surfaces, *in* Atkinson, B.K., ed., Fracture mechanics of rock: London, England, Academic Press, p. 277-349.

Pollard D.D., and Aydin, A., 1988, Progress in understanding jointing: Geological Society of America Bulletin, v. 100, p. 1181-1204.

Poncelet, E.F., 1958, The markings on fracture surfaces: Jour. Soc.. Glass Tech., v. 42, p. 279T-288T.

Poncelet, E.F., 1965, Modern concepts of fracture and flaw: Poulter Research Laboratories technical report 002-65, 160 p.

Preston, F.W., 1926, A study of the rupture of glass: Jour. Soc. Glass Tech., v. 10, p. 234-269.

Preston, F.W., 1939, Bottle breakage - causes and types of fractures : Bull. Amer. Ceram. Soc. v. 18, p. 35-60.

Ramulu M., and Kobayashi, A.S., 1983, Dynamic crack curving - a photoelastic evaluation: experimental mechanics, v. 23, p.1-9.

Roddy , D.J. and Davis, K.L., 1977, Shatter cones formed in large-scale experimental explosion craters, *in* Roddy, D.J., Pepin, R.O. and Merrill, R.B., eds., Impact and explosion cratering: p. 715-750, Pergammon Press, New York.

Rubey, W.W., and Hubbert, , M.K., 1959, Role of fluid pressure in overthrust faulting: Geological Society of America Bulletin, v. 70, p. 167-206.

Saouma, V.E., Barton, C.C., and Gamaleldin, N.A., 1990, Fractal characterization of fracture surfaces in concrete: Engineering Fracture Mechanics, v.35, p. 47-53.

Schand, E.B., 1954, Breaking strength of glass determined from dimensions of fracture mirrors: Jour. Am. Ceram. Society., v. 42, p. 474-477.

Schardin, H., 1959, Velocity effects in fracture, *in* Averbach, B.L., *et al*, eds., Fracture: John Wiley and Sons, New York., p. 297-329.

Scheidegger, A.E., 1982, Comment on 'Is there a genetic relationship between selected regional joints and contemporary stress within the lithosphere of North America?': Tectonics, v. 1, p. 465.

Segal, P., and Pollard, D.D., 1980, Nucleation and growth of strike-slip faults in granite: Journal of Geophysical Research, v. 88, p. 555-568.

Segal, P., and Pollard, D.D., 1983, Nucleation and growth of strike-slip faults in granite: Journal of Geophysical Research, v. 88, p.555-568.

Segal, P, 1984, Rate-dependent extensional deformation resulting from crack growth in rock: Journal of Geophysical Research, v. 89, p. 4185-4195.

Skjeltorp, A.T., and Meakin, P., 1988, Fracture in microsphere monolayers studied by experiment and computer simulation: Nature, v. 335, p. 424-426.

Sornette A., Davy, P. and Sornette, D., 1990a, Growth of fractal fault patterns: Physical Review Letters, v. 65, 18, p. 2266-2269.

Sornette A., Sornette, D., and Davy, P., 1990b, Fractal fault patterns as a dual DLA problem, *in* Rossmanith ed. , Mechanics of Jointed and Faulted Rock: Balkema, Rotterdam.

Skjeltorp, A.T. and Meakin, P., 1988, Fracture in microsphere monolayers studied by experiment and computer simulation: Nature, v. 335, p. 424-426.

Streit R. and Finnie, I., 1980, An experimental investigation of crack-path directional stability: Experimental Mechanics, v. 20(1), p. 17-23.

Suppe, J., 1985, Principles of structural geology: Englewood Cliffs, New Jersey, Prentice-Hall, Inc., 537 p.

Thursteinsson, R., and Mayr, U., 1987, The sedimentary rocks of Devon Island, Canadian Arctic Archipelago: Geological Survey of Canada Memoir 411, 182p.

Tolman, S., and Meakin, P., 1989, Off-lattice and hypercubic lattice models for diffusion-limited aggregation in dimensionalities 2-8: Physics Review Letters, A 40, p. 428.

Tsonis, A.A., 1991, A fractal study of dielectric breakdown in the atmosphere, *in* Schertzer, D., and Lovejoy, S., eds., Non-linear variability in geophysics: Kluwer Academic Publishers, Netherlands, p. 167-174.

Van Damme, 1989, Flow and interfacial instabilities in Newtonian and colloidal fluids, *in* Avnir, D., ed., The fractal approach to heterogeneous chemistry: John Wiley & Sons, Chichester, Great Britain.

Van Hise, C.R., 1896, Principles of North American Pre-Cambrian geology: U.S. Geological Survey 16th Annual Report, p. 581-874.

Voss, R.F., 1988, Fractals in nature: From characterization to simulation, *in* Peitgen, H.O., and Saupe, D., eds., The science of fractal images: Springer-Verlag, New York, USA, 312 p.

Wallner, H., 1939, Linienstrchturen an bruch flachen: Zeitschrift fur Physik, v.13, p.103-112.

Wise, D.U., 1964, Microjointing in basement, middle Rocky Mountains of Montana and Wyoming: Geological Society of America Bulletin, v. 75, p. 287-306.

Witten, T.A. and Sander, L.M.,1981, Diffusion-limited aggregation, a kinetic critical phenomena: Physics Review Letters, v. 47, p. 1400-1403.

Woodworth, J.B., 1896, On the fracture system of joints, with remarks on certain great fractures: Boston Society of Natural Historical Proceedings, v. 27, p. 163-183.

Yoffe, E.H., 1951, The moving Griffith crack: Philosophical Magazine, v. 42, p. 739-750.

York, Derek, 1966, Least-squares fitting of a straight line: Can. J. Physics, v. 44, p. 1079-1086.

APPENDIX A

POTENTIAL APPLICATION OF THE LAPLACE EQUATION TO DYNAMIC FRACTURE BIFURCATION AND SUBCRITICAL FRACTURE PROPAGATION

A.1 Introduction - where is the link?

At first glance it seems unusual to read (or write) a single section relating dynamic fracture bifurcation and subcritical fracture propagation. Generally, dynamic fracture bifurcation involves rapidly moving fractures that bifurcate due to excesses of stress and velocity. In contrast, subcritical fractures propagate slowly, since they form at stresses less than that normally required to fracture rock. What then possibly links these diverse fracture processes?

The two processes are linked by their similarity in pattern and by geometric similarities in their growth dynamics. More specifically, both processes yield fractal patterns, and both processes involve random growth controlled by potential fields, $\emptyset(r)$, which approximately satisfy the Laplace equation, $\nabla^2\emptyset(r) = 0$. For dynamic fracture bifurcation, the stress field is the dominant control. Under the low stress conditions of subcritical fracture propagation, the dominant control need not be stress. Instead, pore-pressure fields may greatly influence subcritical fracture propagation.

A.2 Dynamic fracture bifurcation

A.1 Introduction

Since the advent of fractal geometry there has been a resurgence of investigation into branching patterns associated with fractures (Louis and Guinea, 1987; Louis *et al*, 1985; Skjeltorp and Meakin, 1988), joints (Barton, 1990 pers. comm.) and faults (Davy *et al*, 1990; Sornette *et al*, 1990a; Sornette *et al*, 1990b; Aviles *et al*, 1987; Okubu and Aki, 1987). Much of this work involves the experimental study of fracture mechanics using matched physical and computer models. These models have yet to be extended into the field of dynamic fracture bifurcation (DFB), where fractures bifurcate due to excesses of fracture velocity and stresses at the crack tip. The paucity of DFB simulation is due primarily to the lack of fracture mechanic theory underlying the formation of DFB patterns. Kanninen and Popelar (1985), in their book **Advanced Fracture Mechanics,** state that "fracture bifurcation is an outstanding problem in fracture mechanics, and as yet, no universal crack branching criterion has emerged". Dynamic fracture bifurcation under Mode I loading produces scale-invariant branching patterns such as the one in Fig. A.1. In this section, the fractal dimension of a published mode I DFB pattern is estimated using the box method program (listed in Appendix E). These results are compared with D_f estimates for other scale-invariant patterns produced by growth phenomena proven to be physically and mathematically related, e.g. diffusion-limited aggregation (DLA) and dielectric breakdown. The underlying mechanics of DFB are discussed in light of recent theoretical advances in fracture mechanics and DLA-type growth processes.

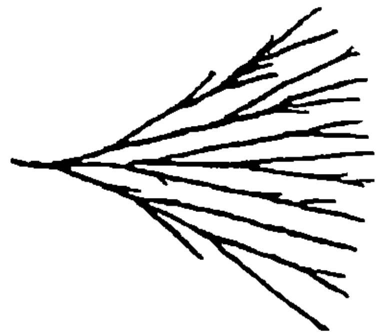

Fig. A.1 Fracture bifurcation pattern in glass formed under mode I loading fracture (digitized image from Schardin, 1959).

A.2.2 Literature review and theory

Preston (1926), Schardin (1959), Irwin (1960), and Bieniawski (1967) conclude that the onset of dynamic fracture bifurcation marks the point where energy at the fracture front exceeds the maximum for a single fracture surface, resulting in the creation of additional surfaces. More specifically, Lawn and Wilshaw (1975) suggest several possible causes of dynamic fracture bifurcation, including 1) dynamic crack-tip stress field distortion (e.g. Yoffe, 1951; Freund, 1976, 1978, 1990), 2) initiation of secondary fractures ahead of the main fracture front when local stress reaches some critical value, and 3) interaction between generated stress waves and the propagating fracture front. Freund (1990), in his comprehensive book **Dynamic Fracture Mechanics** reviews several productive avenues of DFB research. These include DFB models that combine dynamic stress field distortion with initiation of secondary fractures (Streit and Finnie, (1980); and Ramulu and Kobayashi (1983)).

Kulander *et al* (1979) conclude that natural rock joints propagate at velocities less than that needed to produce dynamic fracture bifurcation. Therefore, much of this discussion may not concern naturally occurring joints. However, this discussion can be applied to fracture networks produced by explosive or other non-natural means. Furthermore, mathematical elements of the discussion can be applied to slow-forming fracture networks, such as desiccation cracks.

Several key aspects of DFB are demonstrated in the graph of Fig. A.2 (after Dally, 1979). The graph relates crack velocity and the dynamic stress intensity factor (K) as measured in fracture experiments using toughened epoxy. Note that there is a non-linear response of crack velocity to increases in stress intensity. Initially, small increases in K result in very sharp increases in crack velocity. At high velocities, significant increases in K are required to drive the crack at slightly increased velocities. Immediately preceding successful fracture bifurcation, the fracture surface is reported to be extremely rough. This surface roughness is analogous to the velocity hackle of chapter 3. These results indicate that upon reaching the critical fracture velocity, further increases in stress intensity (and hence increases in fracture propagation energy) are used in attempting to create additional fracture surfaces.

Dally (1979) suggests that as K increases, "the process zone at the tip of the crack expands, and the crack advances by a coalescence of many off-line microcracks". Furthermore, at K of branching, "the fracture-process zone becomes large enough to form additional off-line microcracks which are sufficiently long and are extending at a sufficiently high velocity that

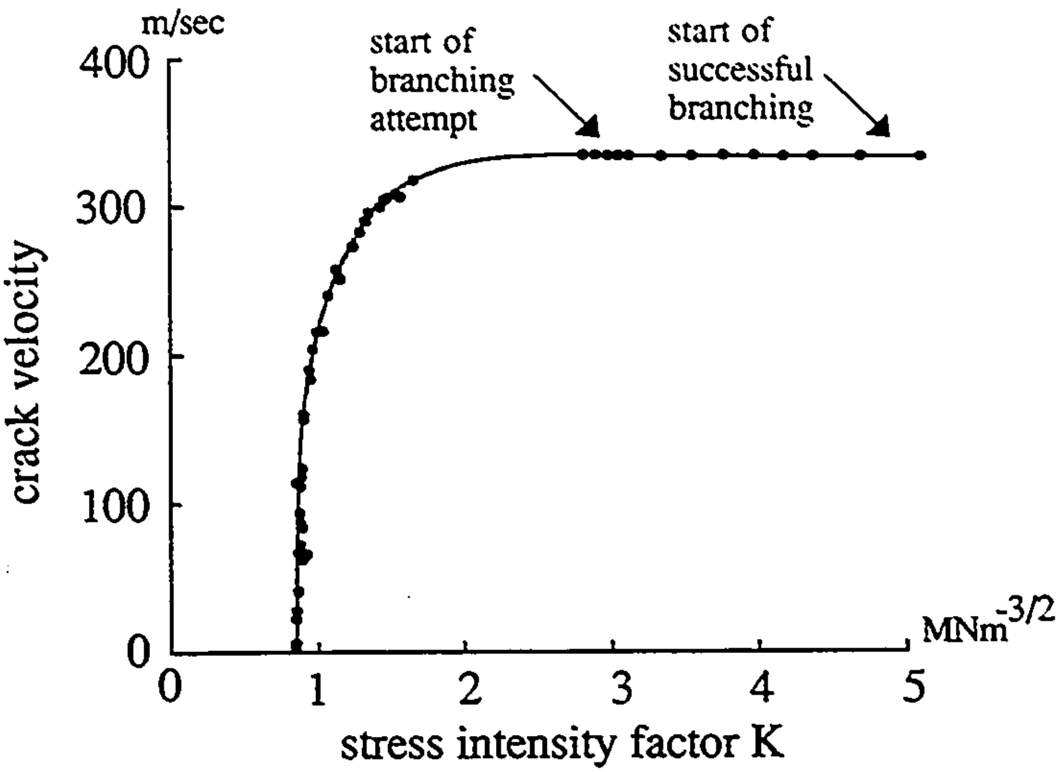

Fig. A.2 Relationship between crack velocity and dynamic stress intensity factor for propagating and branching fracture. Note the non-linear response of fracture velocity to increases in stress intensity factor. Also note that upon attaining a critical fracture velocity, any further increase in stress intensity results in surface roughening and eventually successful fracture bifurcation. Modified from Dally (1979).

they are not unloaded by extension of the main crack". Thus, they become self-propagating. A conceptual sketch of this process is seen in Fig. A.3. More recent models of dynamic fracture bifurcation combine distortion of the dynamic stress field and loss of crack directional stability at some critical distance ahead of the propagating fracture (Streit and Finnie, 1980; Ramulu and Kobayashi, 1983). All suggest that a propagating fracture will bifurcate if an incipient fracture, formed at some distance ahead of the tip of the parent fracture, has sufficient velocity and position so as not to be unloaded by the parent fracture.

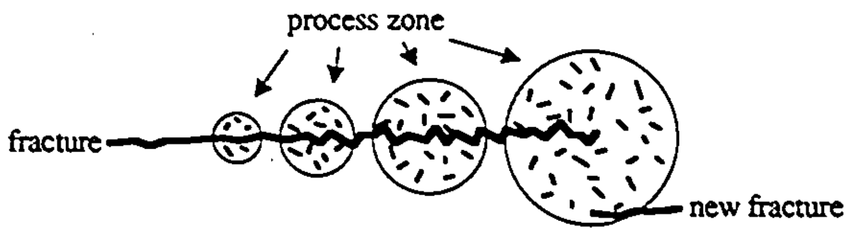

Fig. A.3 Sketch of dynamic fracture bifurcation model conceptualized by Dally, (1979). As stress intensity factor and velocity increase, the fracture surface roughens and the process zone increases in size. Eventually the process zone is enlarged sufficiently that a new fracture is nucleated in a position where the stress has not been unloaded by the parent fracture. This marks the location of dynamic fracture bifurcation.

A.2.3 Fractal characteristics of DFB patterns

Examples of fracture networks formed through dynamic fracture bifurcation are seen in Fig. A.4. This figure (digitized from Schardin,1959) shows scale-invariant crack branching in a glass plate subjected to mode I loading. The patterns are geometrically similar in many respects to bifurcating fractal patterns (see Fig. A.5) associated with other physical phenomena, such as diffusion-limited aggregation (DLA) (Witten and Sander, 1981), dielectric discharge (Niemeyer *et al*, 1984; Tsonis, 1991), viscous fingering (for example Nittmann *et al*, 1985; Maloy *et al*, 1985, Daccord *et al*, 1986), chemical dissolution of a porous medium (Daccord, 1987), and models for dilational fracturing (Louis and Guinea,1987).

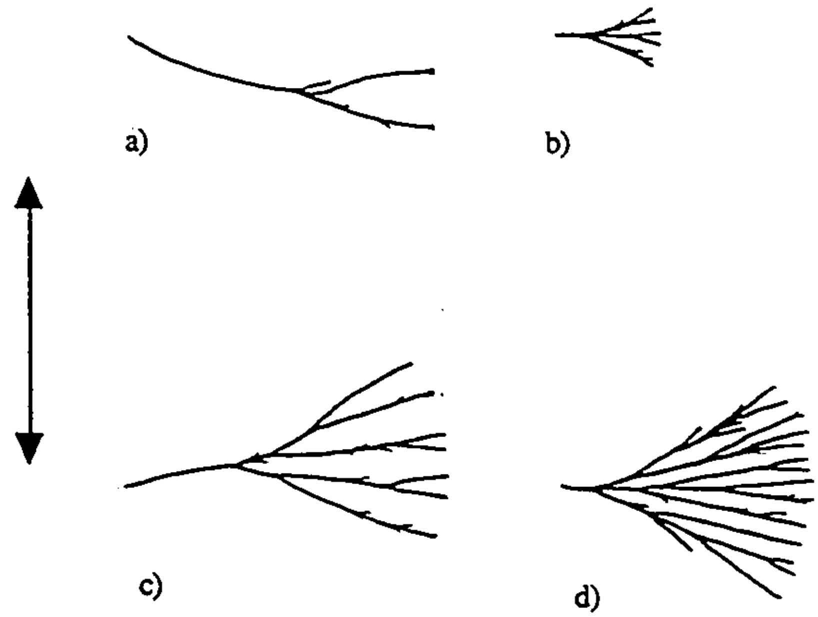

Fig. A.4 Digitized images of several dynamic fracture bifurcation patterns formed in glass plates under Mode I loading (in the direction of arrows). The loading stresses used in the experiments increases from (a) to (d). Original images from Schardin, 1959.

The qualitative similarities between the DFB patterns of Fig. A.4 and the patterns of Fig. A.5 suggest that the branching fracture networks of Fig. A.4 might be fractal. This is supported by analyzing Fig. A.4d using the box method (see section 3.6.2 and Appendix E). The well-defined slope (see Fig. A.6) indicates that the pattern has a fractal dimension $D_f = 1.47 \pm .02$.

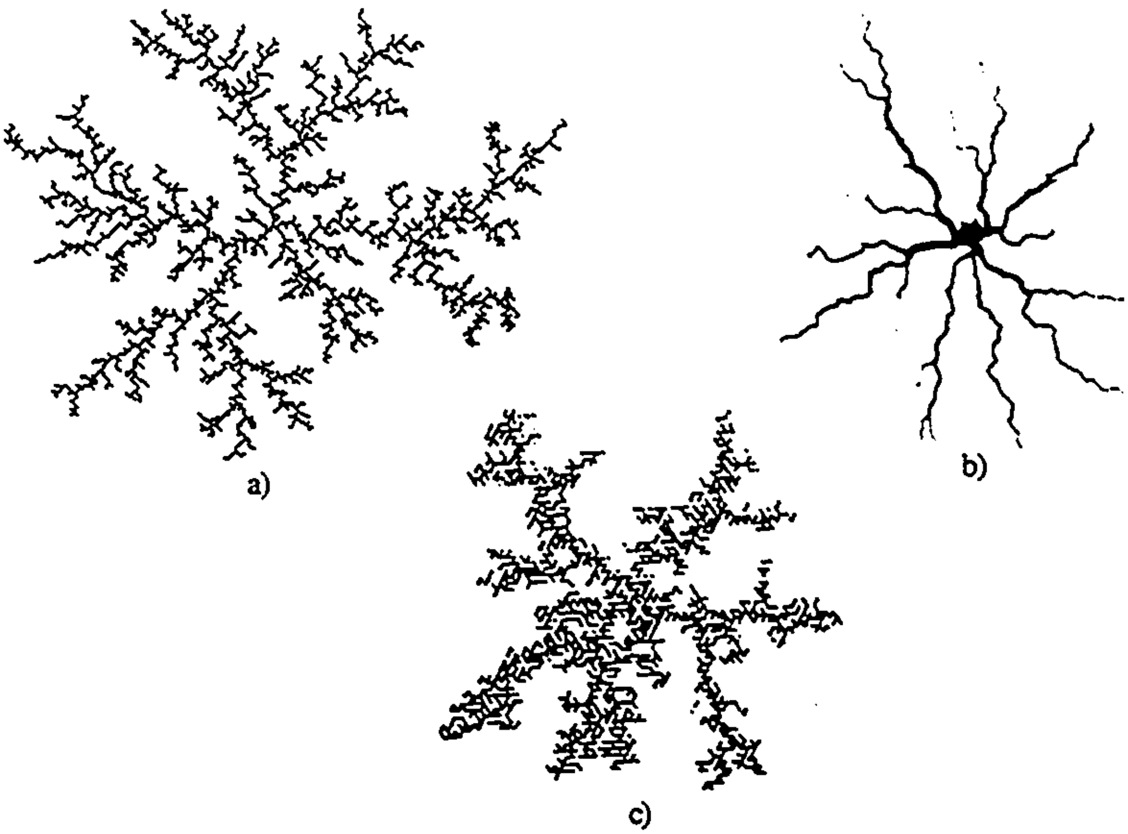

Fig. A.5 Similar fractal patterns formed by different physical process. **a)** Results from diffusion-limited aggregation (DLA) program, D_f=1.7 (see Appendix B). **b)** Dielectric discharge on a glass plate, D_f = 1.7 (Niemeyer *et al*, 1984). **c)** Simulated uniform dilational fracture, D_f=1.55 (Louis and Guinea, 1987). All patterns demonstrate scale-invariant branching.

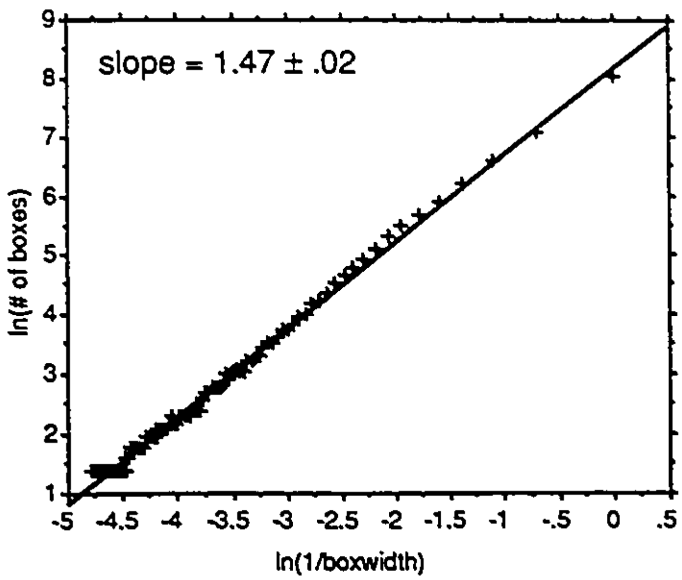

Fig. A.6 Box method plot for image of Fig. A.4d. Fractal dimension is estimated by the slope of the regression line through the data. D_f equals 1.47 ± .02.

A.2.4 Discussion

The $D_f = 1.47$ estimate for the DFB pattern is appreciably less than $D_f = 1.7$ reported for most of the other phenomena in Fig. A.5. However, it is close to $D_f = 1.55$ determined by Louis and Guinea (1987) for their model of uniform dilational fracturing (see Fig. A.5c). Fractal dimensions of 1.68 are measured for desiccation crack experiments (Skjeltorp and Meakin, 1988), while models of continental faulting yield D_f estimates of 1.70 (Sornette *et al*, 1990). Although the D_f values are different, the important fact is that they are all fractal over a significant range of scales.

The most obvious question to be posed when observing the scale-invariant patterns produced by the variety of physical systems represented by Figs. A.4 and A.5 is:

What mathematical and/or physical properties do the different processes share such that their branching patterns are fractal?

This question has been addressed by many, (e.g. Tolman and Meakin, 1989; Meakin and Fowler, in press). They suggest that the various physical phenomena producing fractal growth patterns share two mathematical characteristics:

1) growth is controlled by a field which approximately satisfies the Laplace equation,

$$\nabla^2 \emptyset(r) = 0,$$

where $\emptyset(r)$ is the potential at radius r, and;

2) growth involves a random process.

For example, in the basic diffusion-limited aggregation (DLA) model (see program Appendix C), an aggregate is started with a single seed. A walker is released (at some distance from the seed) and allowed to wander randomly, (via Brownian motion), in the space containing the seed. If the walker moves into a position neighbouring the seed then the walker "sticks" and becomes part of the growing aggregate.

Mathematically, DLA imposes a scalar field of growth probabilities $\emptyset(r)$, where $\emptyset(r)$ is the probability that growth will occur at some distance (r) from a point on the aggregate. This scalar field obeys the Laplace equation, such that

$$\nabla^2 \varnothing(r) = 0,$$

with the boundary conditions $\varnothing(r) = 0$ for all positions occupied by the aggregate, and $\varnothing(r)$ = a constant, as r approaches infinity. The scale-invariant ramified pattern (see Fig. A.5a) results from screening effects of the growing branches in the aggregate. In other words, there is a decreasing probability that random walkers can travel from outside the cluster into ever deeper sections of the cluster without sticking to one of the extending branches.

Similarly, the work of Louis and Guinea (1987) simulates two-dimensional fracture pattern (see Fig. A.5c) formed under quasi-static conditions where the bond breaking probability at the edge of the crack is proportional to stress. They point out that the stress field is a vectorial displacement field instead of a scalar potential field (as are DLA and other diffusional phenomena). Their simulation results are very similar to DLA patterns, confirming a "close formal connection" between the fracture process and DLA (Louis and Guinea,1987). In their model, the bonds to be broken are selected at random, based on a probability proportional to the stress in the bond. This example demonstrates that fractal patterns can be produced in model systems where the controlling field is not a perfect scalar field. This model also demonstrates the importance of randomness in the growth process. If growth did not involve randomness, then the fracture would simply grow in a direction of greatest stress, and the resulting pattern would be a straight line. Randomness allows the fracture to extend into areas which are not necessarily under the greatest stress (i.e. the bonds to be broken are selected at **random**, based on a **probability** proportional to the stress in the bond). Therefore, the fracture is capable of branching. After doing so, the surrounding stress field re-adjusts and the two branch tips become points of stress concentration. Each tip then continues to grow and randomly branch. The physical structure of the rock (i.e. defects or inhomogeneities) provides the randomness in the fracturing process. As discussed in section 5.5, a rock contains many scattered defects which are potential stress concentrators. If the propagating fracture encounters a defect, then the fracture can change direction and/or bifurcate.

Dynamic fracture bifurcation is similar to the fracturing models of Louis and Guinea (1987) in that the process approximately satisfies the mathematical requirements, 1 and 2, above. In DFB, the mode I dynamic stress field is similar to the static stress field of Louis and Guinea in that the local stress varies as the inverse square root of the radial distance from the crack tip (Freund, 1990). However, as indicated by Streit and Finnie (1980), the dynamic mode I stress field loses symmetry, hence directional stability, at some distance r_o ahead of the propagating fracture tip. Furthermore, r_o decreases with increasing velocity. If r_o becomes smaller than r_c, (the critical distance ahead of the crack tip where crack initiation can occur), then the crack direction will become unstable. Therefore, new fracture branches can form at an angle to the parent branch. The DFB patterns in Figure A.4 qualitatively support the theory of Streit and Finnie (1980) in that under increased fracture stresses, the fracture does not necessarily remain perpendicular to remote tension. Instead, the fracture branches at an angle such that the newly formed branches are not unloaded by the parent branches.

The branching patterns of Fig. A.4 are statistically self-similar. Therefore, there must again be some random input into the branching mechanism. One possibility is that the material is not homogeneous down to the scale where fractures are nucleated, i.e. there may be a random distribution of defects. A second possible source of randomness is the reflection and interference of induced stress waves. This might be significant in Schardin's experiments with glass (1959). It would be useful to repeat these experiments using a toughened epoxy that rapidly attenuates stress waves, thereby eliminating induced stress waves as a potential source of randomness.

It is interesting to compare the image of Fig. A.4d with the fractal patterns of other systems (see Fig. A.5). For instance, in the DLA pattern, there is a pronounced screening effect, where the most exposed parts of the cluster prevent penetration of random walkers into the interior regions of the cluster. This screening effect is critical to the formation of structures with fractal dimensions less than the embedding spaces (Meakin and Fowler, in press). Dynamic fracture bifurcation has the same type of inherent screening. The most exposed fracture branches tend to unload stresses in the areas between them, thereby preventing nucleation of new fractures in those areas. However, the patterns produced by DFB in Fig. A.4 are different from the patterns produced by DLA and the other related phenomena of Fig. A.5. Most notably, the DFB pattern does not spread equally in all directions, and there is a lack of scaling in the void space between fracture branches (especially in Fig. A.4d). This might be due to differences between the vectorial displacement stress field of DFB and the scalar fields of the diffusional phenomena. The differences in patterns may also be due to the fact that branching in DFB is dependent on the rate of loading increase. If stress intensities do not increase, then the existing fractures will continue to propagate, but they will not branch. This is demonstrated by the DFB pattern of Fig. A.4a, where the loading stress was relatively small. The individual branches are somewhat longer because the loading stress was not increased very rapidly. Furthermore, the fractures eventually curve back to orientations perpendicular to remote stress. In this way, DFB patterns are extremely sensitive to the loading-unloading characteristics of a system.

In summary, dynamic fracture bifurcation can be described by a qualitative conceptual model involving a combination of dynamic stress field distortion and initiation of secondary fractures ahead of the main front. Collectively, these mechanisms approximately satisfy the requirements for scale-invariant growth, i.e. random growth controlled by a potential field which satisfies the Laplace equation.

A.3 Subcritical joint propagation

In this section, the conceptual model described theory from the previous discussion is applied to subcritical joints. However, instead of studying fracture networks, this discussion reverts to investigating the nature of a propagating fracture front within a planar joint surface.

As discussed in section 5.6.3.1, most joint surfaces display rounded hesitation lines and radial plumose patterns. Using fractographic techniques described by Kulander *et al* (1979), fracture fronts can be reconstructed by drawing continuous line segments perpendicular to adjacent plumose components. Such reconstructions indicate that relatively smooth, rounded fracture fronts are associated with radial plumose patterns. Bahat and Engelder (1984) describe a different joint surface morphology, where the axes of the plumose patterns are irregular and curving (see Fig. A.7a). Using the fractographic technique of Kulander *et al* (1979), their reconstructed fronts are also irregular (see Fig. A.7b). Furthermore, these reconstructed fronts have a lobate appearance similar to some of the fractal images presented in a photographic collection entitled **Fractal Forms** (1991). In particular, Fig. A.7 is similar to the image of a spontaneous crack in glass (see Fig. A.8). This image demonstrates a very irregular fracture front, not at all like the smooth circular forms indicated by most hesitation features (see section 5.6.3.1). Furthermore, this image demonstrates that fracture fronts in glass are not always perpendicular to plumose components. Unfortunately, a detailed description of the material properties and loading configuration for the fracture is lacking. Hypothetically, what conditions could lead to

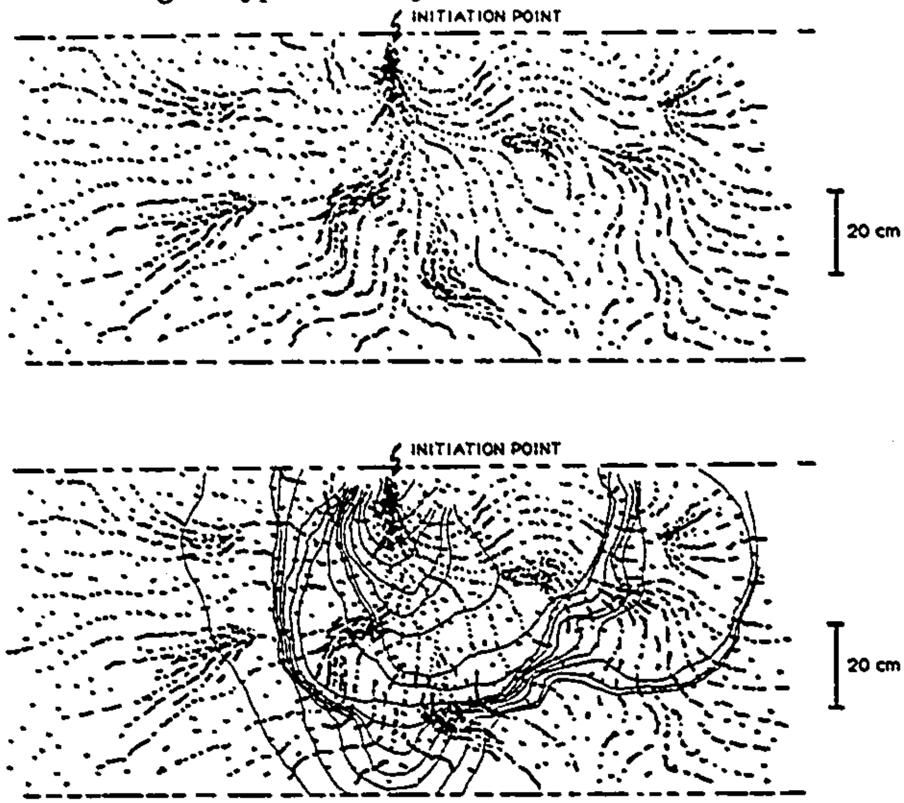

Fig. A.7 a) Sketch of irregular plumose structure on joint surfaces in massive siltstone from the Appalachian Plateau, New York and Pennsylvania (after Bahat and Engelder, 1984). b) Reconstructed fracture fronts (using technique of Kulander *et al*, 1979). Note their irregular lobate appearance and the implied non-uniform growth along the fracture front.

Fig. A.8 Digitized image of a spontaneous crack in glass (from **Fractal Forms**, image #37). Note the irregular fracture front and the irregular surface patterns.

irregular fracture fronts in glass or rock?

One possible answer to this question is provided partially by Bahat and Engelder (1984). They suggest, that these joints formed slowly, possibly under low fracture-stresses, in response to variations in pore-pressure. Given these hypothetical conditions, it is not unreasonable to suggest that the direction of fracture growth is not entirely controlled by remote stresses, rather, it is strongly influenced by the pore-pressure field. The pore-pressure field in a porous medium can be derived from Darcy's equation for fluid velocity (V) (e.g. Meakin and Fowler, in press),

$$V=-M \nabla P$$

where P is the pressure, and M is the fluid mobility (M=k/u where k is the permeability and u is the fluid viscosity). Expressed as a fluid pressure potential (Ø),

$$V=-M\nabla Ø.$$

For an incompressible fluid, conservation requires $\nabla V=0$, so that

$$\begin{aligned} \nabla V &= -M\, \nabla^2(Ø) \\ &= 0, \end{aligned}$$

and the fluid pressure potential obeys the Laplace equation. Daccord (1987) demonstrates this in his 2-dimensional experiments of chemical dissolution in a porous medium (i.e. plaster). In these experiments, the fluid pressure is at a maximum in the dissolved channels, and it decreases in the adjacent porous medium according to the Laplace equation. Dissolution (i.e. pattern growth) is determined by the fluid flux across the water/plaster interface. This flux, in turn, is controlled by the fluid pressure field. Therefore, dissolution preferentially occurs in areas of greatest pressure gradient. For his boundary conditions, the growth is predominantly radial since the pressure gradient between dissolved channels is less than the pressure gradient at the channel tips. This results in the familiar screening effect. In Daccord's experiments, randomness is provided by the porous nature of the medium. Fig. A.9 is a typical dissolution pattern. Note its similarity with the patterns in Fig. A.5.

Fig. A.9 Image of fractal dissolution network from 2-dimensional radial dissolution experiment (after Daccord, 1987). Water was injected at center, and over time dissolution of the porous medium (plaster) resulted in the fractal pattern. Note the similarity with **Fig. A.8.** See text for more discussion.

It would be interesting to repeat Daccord's experiment, but with the plaster sample under slight remote tension. It is possible that a joint surface, also with a fractal front, would arise. Such a surface would probably look very much like the crack in Fig. A.8.

In order to develop such a fracture front in rock, fracture propagation would have to be subcritical. Furthermore, the active subcritical process would have to be dependent on fluid flux along the fracture front. Atkinson and Meredith (1987) indicate several subcritical fracture mechanisms, such as stress corrosion, dissolution, diffusion, ion-exchange and microplasticity that are influenced by the chemical effects of pore water. Hypothetically, if the rock is under slight remote tension, then it is not unreasonable to suggest that a fracture front would propagate into areas where a subcritical fracture process, such as dissolution, is most active (i.e. areas of greatest fluid flux, hence greatest pressure gradient).

As illustrated in Figs. A.7 and A.8, the fracture surfaces do not extend as extremely narrow branches, as do the other fractal phenomena of Fig. A.5. Instead, the extending branches have appreciable width. This may reflect an interplay between the potential effects of the stress field and the potential effects of the pore-pressure field. More precisely, stress concentrations along the fracture front favour fracture extension into high stress sites adjacent to the fracture front, whereas pore-pressure fields and processes of subcritical fracture propagation favour growth into areas of greatest pressure gradient. Given a random medium such as rock, and the possibility that one control does not completely dominate over the other, both potential fields are expected to exercise control on fracture propagation. In other words, the random medium allows both the stress and pore-pressure fields to control propagation. Consider the following hypothetical example. A proportion of bonds along the fracture front are weak enough to fracture without significant action of subcritical processes. This causes a certain amount of extension along the entire length of the fracture front. However, there are also bonds along the fracture front that will only break after being subjected to prolonged subcritical fracture processes. This would cause a greater proportion of bonds to be broken in areas of greatest flux, hence areas of greatest pore-pressure gradients. Therefore after some time, it is conceivable that such a combination of potential fields could produce the wide irregular fracture fronts observed in Figs. A.7 and A.8. Furthermore, the resulting patterns would be influenced by the statistical distribution of bond strengths, and by the interplay between remote tension and subcritical fracture mechanisms.

In order for such patterns to develop in rock, there have to be geological circumstances where a pore-pressure field can develop. This is possible in regions of hydrothermal activity. It is also possible in areas of hydraulic overpressure, particularly when an impermeable barrier is ruptured causing the adjacent rock to be exposed to increased fluid pressure. Undoubtedly, few, if any of these pore-pressure fields will develop with the same boundary conditions as in Daccord's experiments, i.e. greatest fluid pressure at a single point. There may be cases were greatest fluid pressure occurs in linear "pipes", or along thin planar volumes. These different geometrical arrangements would cause the corresponding pore-pressure fields, and hence fracture fronts, to develop differently. The dielectric breakdown (i.e. lightning) simulation by Tsonis (1991) demonstrates that boundary conditions can influence the fractal dimension of the resulting pattern growth. The boundary conditions for his simulation are illustrated in Fig. A.10. There is a horizontal upper boundary (representing a layer of clouds), where the electric potential is held at upper boundary condition - electric potential held at 0

000000000000000000000000000000000000000

111111111111111111111111111111111111111

lower boundary condition - electric potential held at 1

Fig. A.10 Boundary conditions used, and fractal pattern ($D_f = 1.37$) produced in computer simulation of lightning (see Appendix C). This computer generated image represents electric potential as shades of blue. Upper boundary maintained at electric potential of **0**, (dark blue). Lower boundary maintained at electric potential of **1**, (light blue). Discharge is started by setting nucleation site potential to **0** and recalculating the electric potential field between boundaries using discretized Laplace equation. A new discharge site is randomly selected based on its potential. The potential of this site is set to **0** and the field is recalculated. Process is repeated. Notice that the discharge pattern extends more in the vertical direction than in the horizontal direction.

zero, and a lower horizontal boundary where the potential field is held at 1. The electric potential at all sites of an imposed grid between the boundaries is constantly maintained by iterating the discretized Laplace equation,

$$\varnothing_{i,j} = (1/4)*(\varnothing_{i+1,j} + \varnothing_{i-1,j} + \varnothing_{i,j+1} + \varnothing_{i,j-1}),$$

over the 2-dimensional grid. Pattern growth is then initiated by setting the electric potential of the centre site of the row just below the upper boundary to zero. New growth is randomly selected based on the potential within the neighbouring sites. Each time the pattern grows, the potential field is re-established using the discretized Laplace equation. The enlargement of the pattern tip in Fig. A.11, shows how the potential field is reduced between branch tips. An algorithm for this process has been written and is listed in Appendix D.

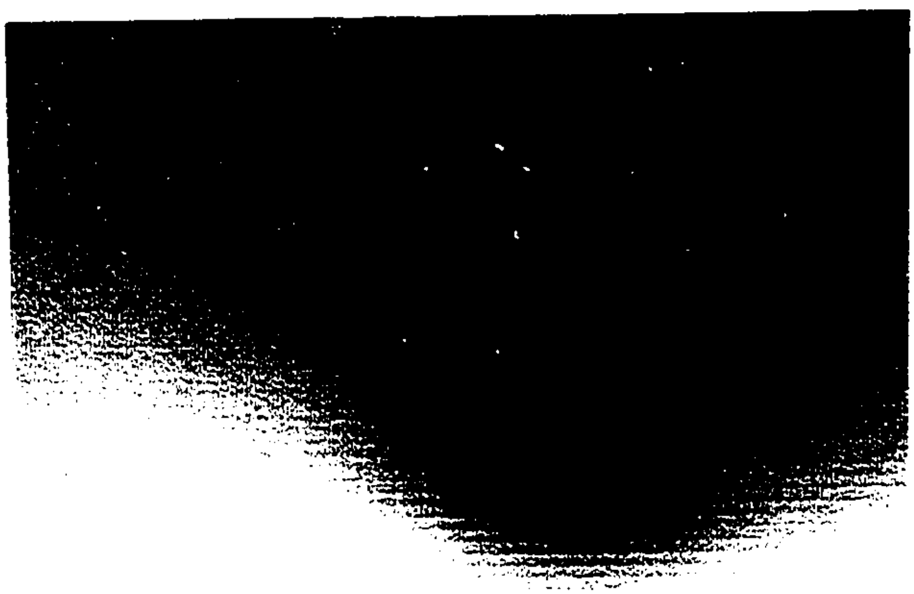

Fig. A.11 Enlargement of branch tip areas of Fig. A.10. Note how the potential field, and hence the probability of growth is significantly reduced between branch tips.

Note the difference between patterns produced by these initial boundary conditions and the patterns of Fig. A.5. The upper and lower planar boundaries cause the pattern to grow and branch primarily in one direction (down). Estimates for the fractal dimension of the resulting patterns are 1.37. This example illustrates that different boundary conditions can have some influence on the potential field, and hence the fractal nature of the resulting growth pattern.

In summary, subcritical fracture propagation in regions of fluid-pressure gradients can hypothetically result in the propagation of very irregular fracture fronts. The fractal nature of these fronts is thought to be controlled by several parameters, including 1) the defects in the rock, 2) the relative interplay between stress and subcritical fracture processes, and 3) the geometrical arrangement (i.e. boundary conditions) of the initial fluid-pressure field.

APPENDIX B

PLUMOSE JOINT PROGRAM LISTING -conceived and coded by D. Roach

The following program is written in Think Pascal for use on a Macintosh IIfx computer with a 24-bit colour graphics card. This program does the following:

1) generate a simulated plumose joint section,

2) display the plumose joint in shaded relief, and

3) generate and measure slit island sections.

```
{PLUMOSE JOINT PROGRAM, DEC.1990, BY DAN ROACH}
{PROGRAM DESIGNED TO GENERATE PLUMOSE JOINT SURFACES, SHADED RELIEF MAP
{ISLAND SECTIONS}
program plumose;
	label
		1, 4, 6;
	type
		xy = array[0..400, 0..400] of longint;
		xyptr = ^xy;
		x = array[0..100000] of integer;
		y = array[0..100000] of integer;
		z = array[0..100000] of real;
		nx = array[0..10000] of integer;
		ny = array[0..10000] of integer;
		ttx = array[0..10000] of integer;
		tty = array[0..10000] of integer;
		ttz = array[0..10000] of real;
		nod = array[0..100000] of integer;
		xptr = ^x;
		yptr = ^y;
		zptr = ^z;
		nxptr = ^nx;
```

```
            nyptr = ^ny;
            nodptr = ^nod;
            txptr = ^ttx;
            typtr = ^tty;
            tzptr = ^ttz;
      var
            nax: nxptr;
            nay: nyptr;
            xya: xyptr;
            tx: txptr;
            ty: typtr;
            tz: tzptr;
            nz: real;
            px: xptr;
            py: yptr;
            pz: zptr;
            pnod: nodptr;
            gWindRecPtr: WindowPtr;
            clsrect, srect: rect;
            k1, k2, k3, k4, operi, peri, m, st, nnd, n, ln, ki, xi, yi, c, xx, ei, si, h, i, j, k: longint;
            seconds: longint;
            dan, nc, mc: rgbcolor;
            sil: real;
            mp: point;
            itn, xoff, xt, yt: integer;
            ph: polyhandle;

begin
(set aside memory for arrays}
      new(px);
      new(py);
      new(pz);
      new(pnod);
      new(nax);
      new(nay);
      new(tx);
      new(ty);
      new(tz);
      new(xya);
{seed random number generator with timer}
      getdatetime(seconds);
      randseed := seconds;
(open million colour window}
      gWindRecPtr := GetNewCWindow(10, nil, Pointer(-1));
      SetPort(gWindRecPtr);
      ShowWindow(gWindRecPtr);
      nc.red := 0;
      nc.green := 0;
      nc.blue := 0;
      rgbforecolor(nc);
      nc.red := 1;
      srect.top := 0;
      srect.left := 0;
      srect.bottom := 600;
```

```
        srect.right := 700;
        paintrect(srect);
        k := 1;
{main loop, 66000 fracture increments}
        while k < 66000 do
          begin
            itn := itn + 1;
            i := 0;
            for h := 1 to k do
              begin
{make sure nre fracture increment is on screen}
                if (pnod^[h] = 0) and (py^[h] > 0) and (px^[h] < 400) and (px^[h] > 0) then
                  begin
                    si := i;
                    xi := px^[h];
                    yi := py^[h];
                    nz := pz^[h];
{probability that current fracture increment is a defect}
                    if (band(random, 8191) / 8191) < 0.2 then
                      begin
{offset current fracture increment random amount between -1 and +1}
                        nz := pz^[h] + (band(random, 8191) / 8191) - (band(random, 8191) / 8191);
                      end;
                    pz^[h] := nz;
{determine all potential fracture sites}
                    if xya^[xi - 1, yi - 1] = 0 then
                      begin
                        tx^[i] := px^[h] - 1;
                        ty^[i] := py^[h] - 1;
                        tz^[i] := nz;
                        i := i + 1;
                      end;
                    if xya^[xi, yi - 1] = 0 then
                      begin
                        tx^[i] := px^[h];
                        ty^[i] := py^[h] - 1;
                        tz^[i] := nz;
                        i := i + 1;
                      end;
                    if xya^[xi, yi - 1] = 0 then
                      begin
                        tx^[i] := px^[h] + 1;
                        ty^[i] := py^[h] - 1;
                        tz^[i] := nz;
                        i := i + 1;
                      end;
                    if xya^[xi - 1, yi] = 0 then
                      begin
                        tx^[i] := px^[h] - 1;
                        ty^[i] := py^[h];
                        tz^[i] := nz;
                        i := i + 1;
                      end;
                    if xya^[xi + 1, yi] = 0 then
```

```
                    begin
                      tx^[i] := px^[h] + 1;
                      ty^[i] := py^[h];
                      tz^[i] := nz;
                      i := i + 1;
                    end;
                  if xya^[xi - 1, yi + 1] = 0 then
                    begin
                      tx^[i] := px^[h] - 1;
                      ty^[i] := py^[h] + 1;
                      tz^[i] := nz;
                      i := i + 1;
                    end;
                  if xya^[xi, yi + 1] = 0 then
                    begin
                      tx^[i] := px^[h];
                      ty^[i] := py^[h] + 1;
                      tz^[i] := nz;
                      i := i + 1;
                     end;
                  if xya^[xi + 1, yi + 1] = 0 then
                    begin
                      tx^[i] := px^[h] + 1;
                      ty^[i] := py^[h] + 1;
                      tz^[i] := nz;
                      i := i + 1;
                    end;
                  ei := i;
                  if (ei = si) and (pnod^[h] = 0) then
                    begin
                      pnod^[h] := 1;
                     end;
                end;
            end;
          i := i - 1;
{now, from all the potential sites, randomly select only a certain percentage, i.e. the site potential}
          for h := 1 to 1 + round(i / 4) do
            begin
              j := round(i * band(random, 8191) / 8191);
              xi := tx^[j];
              yi := ty^[j];
              if xya^[xi, yi] = 0 then
                begin
                  k := k + 1;
                  px^[k] := tx^[j];
                  py^[k] := ty^[j];
                  pz^[k] := tz^[j];
                end;
              xya^[xi, yi] := k;
{do some grey scaling}
              ln := 32000 + round(5000 * pz^[k]);
              if ln < 0 then
                begin
                  ln := 0;
```

```
                    end;
                  mc.blue := ln;
                  mc.red := ln;
                  mc.green := ln;
                  rgbforecolor(mc);
                  moveto(tx^[j] + 20, ty^[j] + 10);
                  line(0, 0);
               end;
           end;
        end;
{this is shaded relief portion}
{clear screen to black}
        srect.top := 0;
        srect.left := 0;
        srect.bottom := 500;
        srect.right := 750;
        nc.red := 0;
        nc.green := 0;
        nc.blue := 0;
        rgbforecolor(nc);
        paintrect(srect);
        for yi := 1 to 399 do
          begin
            for xi := 1 to 399 do
              begin
                k1 := xya^[xi, yi];
                k2 := xya^[xi + 1, yi];
                k3 := xya^[xi, yi + 1];
                k4 := xya^[xi + 1, yi + 1];
{for colour use x gradient and height}
                ln := 35000 + round(35000 * (pz^[k1] - pz^[k2])) - round(1000 * pz^[k1]);
{too dark}
                if ln < 2000 then
                  begin
                    ln := 2000;
                  end;
{too bright}
                if ln > 65000 then
                  begin
                    ln := 65000;
                  end;
                if pnod^[k1] = 0 then
                  begin
                    ln := 0;
                  end;
{set colours}
                mc.blue := round(ln * 1);
                mc.red := ln;
                mc.green := round(ln * 1);
                rgbforecolor(mc);
{draw}
                moveto(175 + 1 * xi, 40 + 1 * yi);
                lineto(175 + 1 * (xi + 1), 40 + 1 * yi);
              end;
```

```
            end;
{wait until mouse button is pressed and then on with slit island tchnique}
        repeat
        until button;
{clear screen, white this time}
        nc.red := 65535;
        nc.green := 65535;
        nc.blue := 65535;
        rgbforecolor(nc);
        paintrect(srect);
4:
        write(123, '    ');
{get  slit island level from keyboard}
        readln(sil);
{clear screen again}
        eraserect(srect);
        nc.red := 0;
        nc.green := 0;
        nc.blue := 0;
        rgbforecolor(nc);
        dan.red := 0;
        dan.blue := 0;
        dan.grecn := 0;
{redraw  new slit island level}
        for n := 1 to 66000 do
           begin
              if pz^[n] > sil then
                 begin
                    rgbforecolor(dan);
                    moveto(200 + px^[n], 20 + py^[n]);
                    line(0, 0);
                 end;
           end;
6:
{wait for user to isolate island to be analyzed}
        while not button do
           begin
           end;
{do area/perimeter calcs on island pointed to with mouse}
        getmouse(mp);
        xt := mp.h;
        yt := mp.v;
        nnd := 2;
        nax^[1] := xt;
        nay^[1] := yt;
        st := 1;
        n := 1;
        m := 1;
        k := 1;
        xoff := 300;
        while n < nnd do
           begin
              xt := nax^[n];
              yt := nay^[n];
```

```
          yt := yt - 1;
{complicated little routine to "fill the island" and calculate the area}
          while not getpixel(xt - xoff, yt) and getpixel(xt, yt) do
            begin
              nax^[m] := xt;
              nay^[m] := yt;
              moveto(xt - xoff, yt);
              line(0, 0);
              m := m + 1;
              k := n;
              yt := yt - 1;
            end;
          xt := nax^[n];
          yt := nay^[n];
          xt := xt - 1;
          while not getpixel(xt - xoff, yt) and getpixel(xt, yt) do
            begin
              nax^[m] := xt;
              nay^[m] := yt;
              moveto(xt - xoff, yt);
              line(0, 0);
              m := m + 1;
              k := n;
              xt := xt - 1;
            end;
          xt := nax^[n];
          yt := nay^[n];
          yt := yt + 1;
          while not getpixel(xt - xoff, yt) and getpixel(xt, yt) do
            begin
              nax^[m] := xt;
              nay^[m] := yt;
              moveto(xt - xoff, yt);
              line(0, 0);
              m := m + 1;
              k := n;
              yt := yt + 1;
            end;
          xt := nax^[n];
          yt := nay^[n];
          xt := xt + 1;
          while not getpixel(xt - xoff, yt) and getpixel(xt, yt) do
            begin
              nax^[m] := xt;
              nay^[m] := yt;
              moveto(xt - xoff, yt);
              line(0, 0);
              m := m + 1;
              k := n;
              xt := xt + 1;
            end;
          xt := nax^[n];
          yt := nay^[n];
          yt := yt - 1;
```

```
xt := xt - 1;
while not getpixel(xt - xoff, yt) and getpixel(xt, yt) do
    begin
        nax^[m] := xt;
        nay^[m] := yt;
        moveto(xt - xoff, yt);
        line(0, 0);
        m := m + 1;
        k := n;
        yt := yt - 1;
        xt := xt - 1;
    end;
xt := nax^[n];
yt := nay^[n];
xt := xt - 1;
yt := yt + 1;
while not getpixel(xt - xoff, yt) and getpixel(xt, yt) do
    begin
        nax^[m] := xt;
        nay^[m] := yt;
        moveto(xt - xoff, yt);
        line(0, 0);
        m := m + 1;
        k := n;
        yt := yt + 1;
        xt := xt - 1;
    end;
xt := nax^[n];
yt := nay^[n];
yt := yt + 1;
xt := xt + 1;
while not getpixel(xt - xoff, yt) and getpixel(xt, yt) dc
    begin
        nax^[m] := xt;
        nay^[m] := yt;
        moveto(xt - xoff, yt);
        line(0, 0);
        m := m + 1;
        k := n;
        yt := yt + 1;
        xt := xt + 1;
    end;
xt := nax^[n];
yt := nay^[n];
xt := xt + 1;
yt := yt - 1;
while not getpixel(xt - xoff, yt) and getpixel(xt, yt) do
    begin
        nax^[m] := xt;
        nay^[m] := yt;
        moveto(xt - xoff, yt);
        line(0, 0);
        m := m + 1;
        k := n;
```

```
                    yt := yt - 1;
                    xt := xt + 1;
                 end;
              n := n + 1;
              nnd := m;
           end;
{finished filling, have calculated area}
        showtext;
{now, see how many pixel edges are on perimeter}
        for n := 1 to nnd - 1 do
           begin
              xt := nax^[n];
              yt := nay^[n];
              operi := peri;
              if not getpixel(xt, yt - 1) then
                 begin
                    peri := peri + 1;
                 end;
              if not getpixel(xt - 1, yt) then
                 begin
                    peri := peri + 1;
                 end;
              if not getpixel(xt + 1, yt) then
                 begin
                    peri := peri + 1;
                 end;
              if not getpixel(xt, yt + 1) then
                 begin
                    peri := peri + 1;
                 end;
           end;
        nnd := nnd - 1;
{write out the data to text screen, also goes to echo file set in run options}
        writeln(nnd, peri);
        nnd := 0;
        operi := 0;
{if check the same island, then get new slit island level}
        if peri = 0 then
           begin
              goto 4
           end;
        peri := 0;
        goto 6;
        halt;
end.
```

APPENDIX C

DLA PROGRAM LISTING-conceived by Witten and Sander (1981) and coded by D. Roach

The following program is written in Think Pascal for use on a Macintosh IIfx computer with a 24-bit colour graphics card. This program generates a DLA pattern.

```
{DLA program by Dan Roach, Feb. 1990}
program originaldla;
	type
		bigary = array[1..512, 1..512] of integer; {array that holds DLA aggregate}
		bigaryptr = ^bigary;
		bigaryhandle = ^bigaryptr;

	var
		a, r, cx, cy, x, y, seconds: longint;
		dxdy: array[0..7, 1..2] of integer;
		radius, xre, yre, rrad, xr, yr, ar, angr, dlarad, circrad: real;
		big: bigaryhandle;
		counter, crad, xc, yc: integer;
		crect: rect;
		fd: text;


begin

	big := bigaryhandle(newhandle(sizeof(bigary)));
{clear out array}
	for xc := 1 to 512 do
		begin
			for yc := 1 to 512 do
				begin
					big^^[xc, yc] := 0;
				end;
		end;
{open file for output}
	open(fd, 'dlaoutput');
{seed random number generator with timer value}
	getdatetime(seconds);
	randseed := seconds;
{set up array of possible walker directions}
	dxdy[1, 1] := -1;
	dxdy[2, 1] := 0;
	dxdy[3, 1] := 1;
```

```
        dxdy[4, 1] := 1;
        dxdy[5, 1] := 1;
        dxdy[6, 1] := 0;
        dxdy[7, 1] := -1;
        dxdy[0, 1] := -1;
        dxdy[1, 2] := -1;
        dxdy[2, 2] := -1;
        dxdy[3, 2] := -1;
        dxdy[4, 2] := 0;
        dxdy[5, 2] := 1;
        dxdy[6, 2] := 1;
        dxdy[7, 2] := 1;
        dxdy[0, 2] := 0;

        cx := 250;
        cy := 250;
        showdrawing;
{start with one pixel at cx,cy}
        big^^[cx, cy] := 1;
        moveto(cx, cy);
        line(0, 0);
{get random angle for positionoing walker on circle shell}
        a := band(random, 255);
        ar := a;
        angr := (ar / 255) * 6.2830;
        xr := dlarad * sin(angr) + cx;
        yr := dlarad * cos(angr) + cy;
        x := round(xr);
        y := round(yr);
{set starting radius for circle}
        circrad := 14;
        dlarad := 4;
{main loop now,  object only grows to max circle radius of 100}
        while circrad < 100 do
                begin
{get random direction}
                        r := band(random, 7);
{move walker}
                        x := x + dxdy[r, 1];
                        y := y + dxdy[r, 2];
                        xr := x;
                        yr := y;
                        rrad := sqrt(sqr(xr - cx) + sqr(yr - cy));
{check if walker leaves circle, if yes get new walker}
                        if rrad > circrad then
                                begin
                                        a := band(random, 511);
                                        ar := a;
                                        angr := (ar / 511) * 6.2830;
                                        xr := circrad * sin(angr) + cx;
                                        yr := circrad * cos(angr) + cy;
                                        x := round(xr);
                                        y := round(yr);
                                end;
```

```
{check if walker is next to a part of the aggregate}
                    if (big^^[x - 1, y - 1] > 0) or (big^^[x, y - 1] > 0) or (big^^[x + 1,
y - 1] > 0) or (big^^[x - 1, y] > 0) or (big^^[x + 1, y] > 0) or (big^^[x - 1, y + 1] > 0) or
(big^^[x, y + 1] > 0) or (big^^[x + 1, y + 1] > 0) then
                        begin
                            counter := counter + 1;
                            if counter = 500 then
                                begin
                                    close(fd);
                                    halt;
                                end;
{draw it}
                            moveto(x, y);
                            line(0, 0);
                            big^^[x, y] := 1;
                            xre := x - cx;
                            yre := y - cy;
                            radius := sqrt(sqr(xre) + sqr(yre));
{write off data if you want it}
                            writeln(radius : 10 : 10);
                            writeln(fd, radius : 10 : 10);
                            dlarad := sqrt(sqr(xr - cx) + sqr(yr - cy)) + 5;
{if aggregate has grown to large then must increase seeding radius}
                            if dlarad > (circrad - 5) then
                                begin
                                    penmode(patbic);
                                    frameoval(crect);
                                    circrad := dlarad + 10;
                                    crad := round(circrad);
                                    crect.top := cy - crad;
                                    crect.bottom := cy + crad;
                                    crect.left := cx - crad;
                                    crect.right := cx + crad;
                                    penmode(pator);
                                    frameoval(crect);
                                end;
{get new random walker direction}
                            a := band(random, 511);
                            ar := a;
                            angr := (ar / 511) * 6.2830;
                            xr := circrad * sin(angr) + cx;
                            yr := circrad * cos(angr) + cy;
                            x := round(xr);
                            y := round(yr);
                            note(1000, 200, 1);
                        end;
            end;

    savedrawing('originaldla');

end.
```

APPENDIX D

DIELECTRIC BREAKDOWN SIMULATION-conceived by (Tsonis, 1991) and coded by D. Roach

PROGRAM LISTING

The following program is written in Think Pascal for use on a Macintosh IIfx computer with a 24-bit colour graphics card. This program simulates a lightning discharge between charged clouds and the earth. It is modeled after the algorithm described by Tsonis, (1991). Briefly, a potential electric field (satisfying the Laplace equation) is established between two horizontal boundaries. Discharge is initiated near the centre of the top boundary and the potential field is recalculated using the discretized Laplace equation. The direction of new discharge is randomly selected based on the potential of neighbouring sites. The pattern grows one pixel, and the process is repeated.

```
{Dielectric discharge simulation, by Dan Roach}
{August, 1991}
{after Tsonis, 1991}
program laplace;
        label
                1, 2, 3, 4, 5;

        type
                grida = array[0..100, 0..100] of real;
                gridaptr = ^grida;
                gridahandl = ^gridaptr;

                canda = array[0..100, 0..100] of real;
                candaptr = ^canda;


        var
                sumpotsq, sumofprob: real;
```

```
                newgrow, c, cx, cy, noc, spipa, cc, agx, agy, pia, totpia: integer;
                agga: array[0..500, 0..1] of integer;
                canpos: array[0..1500, 0..1] of integer;
                proba: array[0..4100] of integer;
                gwindrecptr: windowptr;
                nc: rgbcolor;
                grid: gridaptr;
                n, x, y, t: integer;
                cand: candaptr;
                seconds: longint;

begin
{make space for arrays}
        new(grid);
        new(cand);
{seed random number generator with timer value}
        getdatetime(seconds);
        randseed := seconds;
{set up colour graphics window}
        gwindrecptr := getnewcwindow(10, nil, pointer(-1));
        setport(gwindrecptr);
        showwindow(gwindrecptr);
        showtext;
{set initial Laplace field in grid^[x,y] and show it}
        for y := 0 to 100 do
          begin
            for x := 0 to 100 do
              begin
                grid^[x, y] := y / 100;
                nc.red := round(y * 650);
                nc.blue := round(y * 650);
                nc.green := round(y * 650);
                rgbforecolor(nc);
                moveto(10 + x, 10 + y);
                line(0, 0);
              end;
          end;
{set initial seed in middle of second row}
        totpia := 1;
        agga[1, 0] := 50;
        agga[1, 1] := 1;
{start of main loop, will stop when pattern totals 500 pixels}
        while totpia < 500 do
          begin
{number of times we apply discretized Laplace equation between each growth}
             for n := 1 to 50 do
               begin
                 writeln(n);
{apply discretized Laplace equation in grid space}
                 for y := 1 to 99 do
                   begin
                     for x := 0 to 100 do
                       begin
{special condition, left boundary, must do unique calculation}
```

```
                        if x = 0 then
                         begin
                           grid^[x, y] := (1 / 3) * (grid^[x, y - 1] + grid^[x, y + 1] +
grid^[x + 1, y]);
                            goto 1;
                         end;
{special condition, right boundary, must do unique calculation}
                         if x = 100 then
                          begin
                            grid^[x, y] := (1 / 3) * (grid^[x, y - 1] + grid^[x, y + 1] +
grid^[x - 1, y]);
                            goto 1;
                           end;
{general discetized Laplace equation}
                         if grid^[x, y] > 0 then
                          begin
                            grid^[x, y] := 0.25 * (grid^[x, y - 1] + grid^[x, y + 1] +
grid^[x + 1, y] + grid^[x - 1, y]);
                          end;
1:
                    end;
                end;
        end;
{now show update field in grey scale}
        for y := 1 to 99 do
          begin
            for x := 0 to 100 do
              begin
                nc.red := round(grid^[x, y] * 65000);
                nc.blue := round(grid^[x, y] * 65000);
                nc.green := round(grid^[x, y] * 65000);
                rgbforecolor(nc);
                moveto(10 + x, 10 + y);
                line(0, 0);
             end;
         end;
{determine next increment of growth based on square of potential}
        sumpotsq := 0;
        for pia := 1 to totpia do {pia=points in aggregate, totpia=total number points in
aggregate}
          begin
            agx := agga[pia, 0];
            agy := agga[pia, 1];
{check right candidate}
            if (grid^[agx + 1, agy] = 0) or (cand^[agx + 1, agy] > 0) then
              begin
                goto 2;
             end;
            cand^[agx + 1, agy] := sqr(grid^[agx + 1, agy]);
            sumpotsq := sumpotsq + sqr(grid^[agx + 1, agy]);
2:
{check left candidate}
            if (grid^[agx - 1, agy] = 0) or (cand^[agx - 1, agy] > 0) then
              begin
```

```
                goto 3;
              end;
            cand^[agx - 1, agy] := sqr(grid^[agx - 1, agy]);
            sumpotsq := sumpotsq + sqr(grid^[agx - 1, agy]);
3:
{check up candidate}
            if (grid^[agx, agy - 1] = 0) or (cand^[agx, agy - 1] > 0) then
              begin
                goto 4;
              end;
            cand^[agx, agy - 1] := sqr(grid^[agx, agy - 1]);
            sumpotsq := sumpotsq + sqr(grid^[agx, agy - 1]);
4:
{check down candidate}
            if (grid^[agx, agy + 1] = 0) or (cand^[agx, agy + 1] > 0) then
              begin
                goto 5;
              end;
            cand^[agx, agy + 1] := sqr(grid^[agx, agy + 1]);
            sumpotsq := sumpotsq + sqr(grid^[agx, agy + 1]);
5:
        end;


{determine sum of probabilities, and recalculate probability for each candidate}
      sumofprob := 0;
      cc := 1;
      for y := 1 to 99 do
        begin
          for x := 1 to 99 do
            begin
              if cand^[x, y] > 0 then
                begin
                  cand^[x, y] := cand^[x, y] / sumpotsq;
                  sumofprob := sumofprob + cand^[x, y];
                  canpos[cc, 0] := x;
                  canpos[cc, 1] := y;
                  cc := cc + 1;
                end;
            end;
        end;
{set up array from which neighbour is randomly selected based on normalized probabilit}
        spipa := 0;
        for noc := 1 to cc - 1 do
          begin
            cx := canpos[noc, 0];
            cy := canpos[noc, 1];
            cand^[cx, cy] := cand^[cx, cy] / sumofprob;
            for c := spipa to spipa + round(4095 * cand^[cx, cy]) do {spipa=starting point
in prob aray}
              begin
                proba[c] := noc;
              end;
            spipa := spipa + round(4095 * cand^[cx, cy]);
```

```
                end;
{choose the newg growth}
            newgrow := proba[band(random, 4095)];
            totpia := totpia + 1;
            agga[totpia, 0] := canpos[newgrow, 0];
            agga[totpia, 1] := canpos[newgrow, 1];
            grid^[canpos[newgrow, 0], canpos[newgrow, 1]] := 0;

            writeln(agga[totpia, 0], agga[totpia, 1]);
            nc.red := 65000;
            nc.green := 0;
            nc.blue := 0;

            rgbforecolor(nc);
{superimpose pattern onto grey scale field}
            for t := 1 to totpia do
              begin
                moveto(10 + agga[t, 0], 10 + agga[t, 1]);
                line(0, 0);
              end;


{clear out candidate array}
            for y := 1 to 99 do
              begin
                for x := 1 to 99 do
                  begin
                    cand^[x, y] := 0;
                  end;
              end;
        end;

end.
```

APPENDIX E

BOX METHOD FOR DETERMINING FRACTAL DIMENSION, e.g. Barnsley,1988; Voss, 1988 coded by D. Roach

PROGRAM LISTING

The following program in Think Pascal for use on a Macintosh IIfx computer with a 24-bit colour graphics card. This program estimates the fractal dimension of patterns previously stored in a PICT format. The data is written off to a text screen, which can be stored for future regression analysis.

```
program boxmethod;


type
        ba = array[0..150000] of integer;
        baptr = ^ba;
        opa = array[0..1, 0..50000] of integer;
        opaptr = ^opa;

        f = file of integer;
        ca = record
                x: integer;
                y: integer;
        end;
        radi = record
                tot: longint;
                occ: longint;
                n: longint;
        end;

var
        bar: baptr;
        cpr, creck, picrect, erect, c, center, drawrect: rect;
        cr, ox, oy, rad, px, py, ax, ay, cx, cy, x, y: integer;
        rn, art, cc, xr, ar, sr, yr: real;
        oarad, mi, bigx, litx, bigy, lity, cp, ard, arad, k, q, n, m: longint;
        name: str255;
        fd: f;
        numbox, numinbox, xf, yf, xmax, ymax, truemax, bwidth, xc, yc, xleft, ytop,
        globalref: integer;
        mywindow: windowptr;
```

```
        ra: array[0..500] of radi;
        pc: point;
        fe: text;
        pa: opaptr;

procedure getpictdata (dataptr: ptr; bytecount: integer);
var
        err: integer;
        longcount: longint;
begin
        longcount := bytecount;
        err := fsread(globalref, longcount, dataptr);
end;

procedure getanddrawpictfile;
var
        wher: point;
        reply: sfreply;
        myfiletypes: sftypelist;
        numfiletypes: integer;
        err: oserr;
        myprocs: qdprocs;
        picthand: pichandle;
        longcount: longint;
        mypb: paramblockrec;
begin
        wher.h := 20;
        wher.v := 20;
        numfiletypes := 1;
        myfiletypes[0] := 'PICT';
        sfgetfile(wher, '', nil, numfiletypes, myfiletypes, nil, reply);
        if reply.good then
                begin
                        err := fsopen(reply.fname, reply.vrefnum, globalref);
                        setstdprocs(myprocs);
                        mywindow^.grafprocs := @myprocs;
                        myprocs.getpicproc := @getpictdata;
                        picthand := pichandle(newhandle(sizeof(picture)));
                        err := setfpos(globalref, fsfromstart, 512);
                        longcount := sizeof(picture);
                        err := fsread(globalref, longcount, ptr(picthand^));
                        drawpicture(picthand, picthand^^.picframe);
                        err := fsclose(globalref);
                        mywindow^.grafprocs := nil;
                        disposhandle(handle(picthand));
                end;
        end;
begin
        new(bar);
        new(pa);
        picrect.top := 40;
        picrect.left := 0;
        picrect.right := 600;
```

```
picrect.bottom := 480;
setdrawingrect(picrect);
showdrawing;
getport(mywindow);
getanddrawpictfile;
m := 1;
bigx := 0;
litx := 1000;
bigy := 0;
lity := 1000;
showtext;

for y := 1 to 300 do
begin
   for x := 1 to 300 do
      begin
         if getpixel(x, y) then
           begin
              m := m + 1;
              if x > bigx then
                 bigx := x;
              if x < litx then
                 litx := x;
              if y > bigy then
                 bigy := y;
              if y < lity then
                 lity := y;
           end;
      end;
end;

creck.top := lity - 2;
creck.bottom := bigy + 3;
creck.left := litx - 2;
creck.right := bigx + 3;
framerect(creck);
creck.top := lity;
creck.bottom := bigy;
creck.left := litx;
creck.right := bigx;

xmax := bigx - litx;
ymax := bigy - lity;

if xmax > ymax then
   truemax := xmax
else
   truemax := ymax;

xleft := litx;
ytop := lity;

for bwidth := 1 to truemax do
begin
```

```
            for yc := ytop to (ytop + ymax) do
              begin
                for xc := xleft to (xleft + xmax) do
                  begin
                    for yf := yc to (yc + bwidth) do
                      begin
                        for xf := xc to (xc + bwidth) do
                          begin
                            moveto(xf + 300, yf);
                            line(0, 0)
                            if getpixel(xf, yf) then
                              begin
                                numinbox := numinbox + 1;
                                xf := xc + bwidth + 1;
                                yf := yc + bwidth + 1;
                              end;
                          end;
                      end;
                      numbox := numbox + 1;
                      xc := xc + bwidth - 1;
                  end;
                  yc := yc + bwidth - 1;
              end;
              writeln(bwidth, numinbox, numbox);
              numinbox := 0;
              numbox := 0;
            end;

end.
```